

**Polarization observables in ${}^3\text{He}(\vec{e}, e'n)$
and the neutron electric form factor**

David Boersma

Utrecht University, 2002
ISBN 90-6488-020-4

**Polarization observables in ${}^3\text{He}(\vec{e}, e'n)$
and the neutron electric form factor**

Polarisatieobservabelen in ${}^3\text{He}(\vec{e}, e'n)$
en de elektrische vormfactor van het neutron
(met een samenvatting in het Nederlands)

Proefschrift ter verkrijging van de graad van doctor aan
de Universiteit Utrecht op gezag van
de Rector Magnificus, Prof. Dr. W.H. Gispen,
ingevolge het besluit van het College voor Promoties
in het openbaar te verdedigen op
vrijdag 14 juni 2002 des middags te 12.45 uur

door

David Jan Boersma

geboren op 4 maart 1970, te Hoogkerk (Groningen)

Promotores: Prof. Dr. P. Kooijman
Faculteit der Natuur- en Sterrenkunde
Prof. Dr. G. van Middelkoop
Faculteit der Exacte Wetenschappen (VU)

Copromotor: Dr. Th. S. Bauer
NIKHEF

ISBN: 90-6488-020-4

The work described in this thesis is part of the research programme of the "Stichting voor Fundamenteel Onderzoek der Materie (FOM)", which is financially supported by the "Nederlandse Organisatie voor Wetenschappelijk Onderzoek" (Netherlands Organization for Scientific Research, NWO).

This work was sponsored by the Stichting Nationale Computerfaciliteiten (National Computing Facilities Foundation, NCF) for the use of supercomputer facilities, with financial support from the "Nederlandse Organisatie voor Wetenschappelijk Onderzoek" (Netherlands Organization for Scientific Research, NWO).

Contents

1	Introduction	1
2	Theory	7
2.1	Decomposition of the cross section for polarized electron scattering	8
2.2	The ^3He ground state	10
2.3	Interpretation of spin correlation functions	11
2.3.1	PWIA(S)	14
2.3.2	Faddeev equations	16
2.3.3	Lorentz covariant approach of Nagorny	21
2.4	Asymmetry measurements	26
2.5	Existing data on G_E^n	33
3	Experimental setup	39
3.1	The MEA/AmPS accelerator facility	39
3.2	Polarized electrons	42
3.2.1	Polarized electron source	42
3.2.2	Polarimetry	42
3.3	Polarized ^3He target	45
3.4	Detectors	47
3.4.1	The BigBite electron spectrometer	47
3.4.2	Recoil detector	50
3.4.3	Range telescope	51
3.4.4	Neutron detector	53
3.4.5	Electronics and data acquisition	61

4 Calibration and Performance	65
4.1 Definitions	65
4.1.1 Labeling	65
4.1.2 Coordinate frames	66
4.2 Calibration parameters of the neutron detector	67
4.2.1 Distance-of-Flight	67
4.2.2 Energy deposit and particle identification	69
4.2.3 Time-of-Flight	71
4.3 Parameter determination	73
4.3.1 Test pulses	73
4.3.2 Cosmics	73
4.3.3 Elastic H(e, e'p)scattering	74
4.4 Selection of quasi-free ${}^3\text{He}(e, e'n)$ events	79
4.5 Background considerations	81
4.5.1 Random background	81
4.5.2 Coincident background	88
5 Results	99
5.1 A'_z result and systematic error analysis	99
5.1.1 Correlation of A'_z with the injected current	100
5.1.2 Conclusion on the systematic error	103
5.1.3 Results	104
5.2 A'_x and G_E^n	107
5.2.1 The experimental result	107
5.2.2 Extraction of G_E^n	108
5.2.3 Conclusion	112
5.3 Outlook	112
6 Summary	117
Samenvatting	127
Dankwoord	131

Chapter 1

Introduction

Scattering experiments are a natural means of investigating the structure of objects. In our daily lives, when we are watching an object using our eyes, we are already performing a scattering experiment: light sources like lamps, candles or the sun provide a stream of light which scatters from the objects around us. A fraction of the scattered light enters our eyes, and an unconscious part of our brain performs a fast and clever analysis of the angular distribution of the intensity (brightness) and the energy (color). This analysis yields three-dimensional images which are presented to the conscious part of our brains and thus we are “observing” physical objects.

In an electron scattering experiment the electron accelerator takes the role of the lamp. It provides a stream electrons which we let collide with the objects under study, and from the distribution of the scattered particles we try to reconstruct the properties of the original object. The object under study (in our experiments an atomic nucleus) may disintegrate in the collision; by detecting also (some of) the fragments (“exclusive” scattering) we can gain more information about the nature and dynamics of the elements of which the object was composed.

A rule of thumb from quantum mechanics (in which matter and forces can be represented both as particles and as fields) tells us that the best obtainable spatial resolution is inversely proportional to the characteristic momentum of the probing particles. When we use visible light as a probe then the smallest observable details are of the order of 10^{-7} m. In this thesis we are mainly interested in protons and neutrons, the constituents of atomic nuclei, which have characteristic sizes of 10^{-15} m [1, 4].

This means that in order to study nuclear phenomena we must probe the nucleus with photons of an energy/momentum eight orders of magnitude larger than that of the photons of visible light. Such photons are exchanged when electrons, accelerated to energies of 100 to 1000 MeV, collide with nuclei. The distributions of the scattering angle and of the energy of the scattered electrons depends on the structure of the nucleus and its components; but unlike the perception of visual images of macroscopical objects, the reconstruction of the subatomic structure takes years of data analysis and theoretical interpretation.

For the hypothetical case of a *pointlike* nucleus these distributions can readily be calculated theoretically using the Dirac equation [2, 3]. The *extendedness* of a nuclear object can be parametrized (assuming that the electron and the nucleus exchange only one photon) with so-called electric and magnetic form factors, as introduced by Rosenbluth [7] and Sachs [13]. We can also calculate how electrons scatter from extended nuclear objects and by comparing the calculated distributions with the actually measured ones we can reconstruct nuclear shapes.

Hofstadter *et al.* [9] determined in this way the structure of several nuclei, in particular that of the hydrogen nucleus (the proton). The conclusion was that the proton is not pointlike, and that the charge distribution can be approximated by a simple exponential function of the radius (which corresponds to the so-called dipole form factor in the Rosenbluth formula).

In contrast to the proton, the net electric charge of the other main constituent of atomic nuclei – the neutron – is zero. But since the neutron is also an extended object, some part of it (its core) can be charged while the rest (the mantle) is oppositely charged. Therefore it would be interesting to also perform an elastic electron scattering experiment on neutrons.

Unfortunately, this is experimentally almost impossible because of the lack of a dense free neutron target. Neutrons can be confined in a physical box (see *e.g.* ref. [81]) or in a three-dimensional magnetic trap (see *e.g.* ref. [34, 92]) but with these techniques at most a few thousand neutrons have been trapped. Even with the largest currents that can be produced by present day accelerators (and assuming the beam can be directed through the trap) it would take unrealistically long to obtain a significant result from a scattering experiment with such a thin target.

Instead of scattering electrons from neutrons, thermal neutrons (from a nuclear reactor) can be scattered from the electron cloud of large atoms. This gives information about the charge radius and the depth of the potential well; or, in form factor language, the slope of the electric form factor as a function of the

momentum transfer. This type of experiment was first performed in 1947 (on Lead and Bismuth [5] and Xenon [6]) and has been repeated and improved up to present days [58].

For the investigation of the structure of the neutron at smaller distance scales the most practical approach seems to be to study neutrons bound in small nuclei. In this approach we have to assume that we (will) understand theoretically sufficiently well the effects of nuclear dynamics and the relation between the electromagnetic structure of a *free* and a *bound* nucleon.

One may for instance determine the electromagnetic structure of the deuteron from elastic electron-deuteron scattering. Using a parametrization of the interaction between nucleons (obtained from elastic nucleon-nucleon scattering) and the electromagnetic structure of the proton, values for the electromagnetic form factors of the neutron may be extracted. For the magnetic form factor of the neutron, G_M^n , this approach has worked quite well, since it is of the same order of magnitude as G_M^p . However, the electric form factor G_E^n is more than an order of magnitude smaller than the other nucleon form factors. Its effect on the cross section is rather subtle and its determination becomes very sensitive to small uncertainties in the other parts of the analysis, most notably the choice of the parametrization of the nucleon-nucleon interaction.

For this reason polarized exclusive electron scattering experiments have been proposed. In such experiments the *spins* (intrinsic rotation axes) of the electrons and the target nuclei are oriented in certain directions (while in *unpolarized* experiments the spins point in arbitrary directions). The spin dependence is very sensitive to some effects that are otherwise averaged out.

The spin dependent cross sections of in particular the ${}^2\vec{H}(\vec{e}, e'n)$ and ${}^3\vec{He}(\vec{e}, e'n)$ reactions contain terms linear in the electric form factor. Compared to the ${}^3\vec{He}(\vec{e}, e'n)$ reaction, the ${}^2\vec{H}(\vec{e}, e'n)$ reaction has the advantage that the nuclear ground state is relatively simple and the dynamics of deuteron electrodisintegration are understood fairly well, to the extent that calculations agree satisfactorily well with the data of almost all unpolarized ${}^2\text{H}(e, e'N)$ experiments. The ${}^3\vec{He}(\vec{e}, e'n)$ reaction has the advantage that (for 90% of the wave function) the protons are in a relative *S* state so that polarized ${}^3\text{He}$ gas is effectively a polarized neutron target.

Both experiments have been performed in the internal target hall of the MEA/AmPS accelerator facility at NIKHEF in 1997 and 1998. The ${}^2\vec{H}(\vec{e}, e'n)$ experiment has been described in ref. [89]. In the present thesis the ${}^3\vec{He}(\vec{e}, e'n)$ experiment, its results and problems and the lessons learned are discussed.

In chapter 2 we give an overview of the theoretical aspects of electron scat-

tering on ^3He . We introduce the polarization observables that we measured in our experiment, and describe some aspects of the formalisms behind the calculations performed by Golak and Nagorny for the interpretation of our experimental data. In chapter 3 we give a brief overview of the MEA/AmPS accelerator facility at NIKHEF and the detectors used in our experiment. In chapter 4 the methods and results of the calibration of the neutron detector are described. The background contributions are treated in detail. In chapter 5 we present the results of the measured asymmetries A'_z and A'_x , as well as a discussion about the value(s) of G_E^n that may be extracted from these results.

Chapter 2

Theory

The cross section for electron scattering on ^3He may be decomposed in terms that are proportional to both, one or none of the polarizations of the electron and the ^3He nucleus. The proportionality factors (referred to as spin correlation functions) are specific for each reaction channel and depend nontrivially on the kinematics of the scattering process.

Various phenomenological models have been constructed to describe the properties of the spin correlation functions in terms of nuclear structure, hadron structure and reaction mechanisms. The intuitively and computationally simplest approach, the (symmetrized) plane wave impulse approximation, does not yield an adequate description, but we treat it for reference and comparison. The model of Nagorny is Lorentz covariant and gauge invariant but rescattering of nucleons is taken into account only up to second order, using a simple NN-potential. The model of Golak has a standard recipe for current conservation and is nonrelativistic, but calculates the rescattering to all orders, using realistic NN-potentials.

An extensive Monte Carlo simulation has been performed in order to compare the model predictions, which calculate the observables for specific kinematics, with the results of our experiment, which are averages over finite acceptances and resolutions.

In these calculations the electromagnetic structure of the bound (off-shell) nucleon and that of a free (on-shell) nucleon are assumed to be identical and given by a reasonably well-known magnetic form factor $G_M^n(Q^2)$ and a poorly known electric form factor $G_E^n(Q^2)$. The model predictions for one of the spin

correlation functions, A'_x , depend significantly on G_E^n ; hence a measurement of A'_x is an indirect measurement of G_E^n (within the context of each particular model). This G_E^n value should be compared with the available data from other experiments and with models of the nucleon.

2.1 Decomposition of the cross section for polarized electron scattering

The cross section for a particular scattering process is equal to the squared magnitude of the S -matrix element $\mathcal{M}_{fi} = \langle f|S|i\rangle$ corresponding to the transition probability between an initial state i and a final state f , multiplied with a trivial kinematic factor. If the in- and/or outgoing particles carry spin, the appropriate averages and sums must be taken over all possible spin states, where the weighting factors for the averaging follow from the polarizations of the incoming particles¹. In the following we restrict the discussion to the exclusive scattering of longitudinally polarized electrons off a polarized ^3He target, where the scattered electron and the knocked-out neutron are detected. The differential cross section may be decomposed as [44]:

$$\begin{aligned} \frac{d^6\sigma}{dE_{e'}d\Omega_{e'}dE_nd\Omega_n} &= \overline{\sum_{fi}} K \cdot |\mathcal{M}_{fi}|^2 & (2.1) \\ &= \frac{d^n\sigma_0}{dE_{e'}d\Omega_{e'}dE_nd\Omega_n} \times [1 + \mathbf{A}^0 \cdot \mathbf{S} + h(A_e + \mathbf{A}' \cdot \mathbf{S})] & (2.2) \end{aligned}$$

where $\overline{\sum_{fi}}$ denotes a weighted average of initial, and a sum over final polarizations. The remaining symbols have the following significance:

$$\begin{aligned} K &: \text{Kinematic factor} \\ \sigma_0 &: \text{Unpolarized cross section} \\ \mathbf{A}^0 &: \text{Target analyzing powers} \\ \mathbf{S} &: \text{Target polarization vector} & (2.3) \\ A_e &: \text{Electron analyzing power} \\ h &: \text{Electron helicity} \\ \mathbf{A}' &: \text{Spin-spin correlation functions.} \end{aligned}$$

¹If the polarization of (one of) the outgoing particles is measured, the analyzing power(s) of the polarimeter(s) provide the weighting factors for summation over the spin states of the outgoing particles.

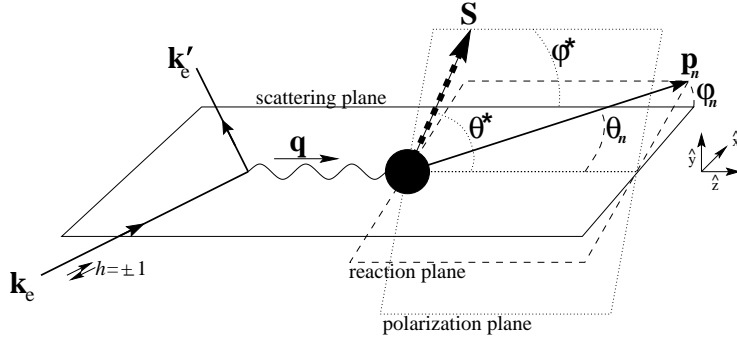


Figure 2.1: The conventional definitions of some of the relevant momenta and the target polarization vector for a doubly polarized electron scattering reaction.

In figure 1 the definitions of several conventional kinematic and polarization variables are given. The formal definitions of the kinematic variables which are used throughout this work are (in laboratory coordinates):

$$k_e = (E/c, 0, 0, E/c) \quad (2.4)$$

$$k'_e = (E', E' \sin \theta_e \cos \phi_e, E' \sin \theta_e \sin \phi_e, E' \cos \theta_e)/c \quad (2.5)$$

$$q = (\omega/c, \mathbf{q}) = k_e - k'_e \quad (2.6)$$

$$Q^2 = -q^2 = \mathbf{q}^2 - \omega^2/c^2 = 4EE' \sin^2(\theta_e/2)/c^2 \quad (2.7)$$

$$\mathbf{p}_m = \mathbf{q} - \mathbf{p}_n \quad (2.8)$$

$$E_m = \omega - T_n - T_{pp} \quad (2.9)$$

$$= \omega - \sqrt{\mathbf{p}_n^2 c^2 + m_n^2 c^4} + m_n c^2 - \sqrt{\mathbf{p}_m^2 c^2 + 4m_p^2 c^4} + 2m_p c^2.$$

The Cartesian coordinate frame for \mathbf{A}^0 , \mathbf{A}' and \mathbf{S} is spanned by the target polarization unit vectors (see figure 1):

$$\begin{aligned} \hat{\mathbf{z}} &= \mathbf{q}/|\mathbf{q}| \\ \hat{\mathbf{y}} &= \mathbf{q} \times \mathbf{k}/|\mathbf{q} \times \mathbf{k}| \\ \hat{\mathbf{x}} &= \hat{\mathbf{y}} \times \hat{\mathbf{z}} \end{aligned} \quad (2.10)$$

or, in words, $\hat{\mathbf{z}}$ is parallel to the transferred 3-momentum, $\hat{\mathbf{y}}$ is perpendicular to the scattering plane and $\hat{\mathbf{x}}$ lies in the scattering plane transversal to the transferred 3-momentum, such that $\hat{\mathbf{x}}$, $\hat{\mathbf{y}}$ and $\hat{\mathbf{z}}$ form a righthanded coordinate frame.

The individual terms on the righthand side in equation (2.2) are usually determined experimentally by measuring the numbers of events $N^{\pm\pm}$ for the four different combinations of the spin states with helicity $h = \pm h_0$ and target polarization $\mathbf{S} = \pm P \hat{\mathbf{S}}_0$. In the ideal case of constant degrees of polarization and the same integrated luminosity for all four measurements, the spin correlation functions take the shape of asymmetries:

$$A_e = \frac{N^{++} + N^{+-} - N^{-+} - N^{--}}{N^{++} + N^{+-} + N^{-+} + N^{--}} \frac{1}{h_0} \quad (2.11)$$

$$\mathbf{A}^0 \cdot \hat{\mathbf{S}}_0 = \frac{N^{++} - N^{+-} + N^{-+} - N^{--}}{N^{++} + N^{+-} + N^{-+} + N^{--}} \frac{1}{P} \quad (2.12)$$

$$\mathbf{A}' \cdot \hat{\mathbf{S}}_0 = \frac{N^{++} - N^{+-} - N^{-+} + N^{--}}{N^{++} + N^{+-} + N^{-+} + N^{--}} \frac{1}{|h_0 P|} \quad (2.13)$$

Hence the target analyzing power A_y^0 is also sometimes referred to as the *target asymmetry* or *induced asymmetry*; and A_e is sometimes called the *electron asymmetry*.

More generally, the spin correlation functions may be obtained by measuring with four different combinations of the target polarization and electron helicity, for each of three linearly independent directions of the target spin vector. This is worked out in more detail in section 2.4.

2.2 The ^3He ground state

Calculations involving 3N states, in particular the ^3He ground state, are usually performed by using a basis of antisymmetrized products of one-nucleon eigenstates. For the analysis of polarization observables in quasi-elastic scattering it is more convenient to work with the partial wave decomposition introduced by Derrick and Blatt [11, 28]. In this scheme spin-isospin states of the trinucleon system are linearly combined to make states of definite symmetry (symmetric states, antisymmetric states and two kinds of mixed symmetry states) under exchange of two particle labels. The spatial part of the wave function is also a state of definite symmetry, in such a way that the total wave function is antisymmetric.

In this representation, the two $L = 0$ states with an antisymmetric spin-isospin part account for 88.6% of (the square of the magnitude of) the wave function². In these states the isospin part is symmetric and the spin part an-

² The numbers in this paragraph are taken from ref. [28] where a wave function is used that

tisymmetric. Hence for this part of the wave function, the two protons are in a relative S state and the neutron is effectively carrying the spin of the nucleus. Therefore, polarized ${}^3\text{He}$ gas may be used as an effective polarized neutron target, with a dilution from unpolarized protons. This is why, in absence of a dense enough free neutron target, it has been proposed to extract neutron electromagnetic form factors from measurements of the ${}^3\text{He}(\vec{e}, e')$ [28] and ${}^3\text{He}(\vec{e}, e'n)$ [44] reactions.

In order to interpret the results of such measurements correctly the relative contributions of other components must be known and taken into account. In the calculations of ref. [28] the remaining 11.4% consists for 1.5% of the mixed symmetry S wave (called S'), 0.05% of P states, 8.4% of mixed symmetry D waves and about 1.4% for the higher partial waves. E.g., in the D wave the nucleon spins are oriented opposite to the nuclear spin, so that at higher missing momenta (where the D wave has more strength than the S wave) we may expect (at least in PWIA, see section 2.3.1) the asymmetries to change sign.

2.3 Interpretation of spin correlation functions

The goal of measuring spin correlation functions (or of intermediate energy electron scattering experiments in general) is to obtain new information about nuclear and nucleon structure. The relation between the structure of the initial state and the scattering observables strongly depends on the details of the electromagnetic interaction of the electron with (the constituents of) the nucleus, and of the subsequent decay of the excited system into free particles (residual nucleus, nucleons, pions and gamma rays). Therefore, we need a model which provides a consistent description of the electrodisintegration of a bound system of strongly interacting particles.

Quantum chromodynamics (QCD) and quantum electrodynamics (QED) are presently regarded as the fundamental theories of strong and electromagnetic interactions, respectively. Unfortunately, due to the large value of the strong coupling constant for $Q^2 < 1 \text{ GeV}^2/c^2$ perturbative QCD calculations would have to be carried out to very high order (and they may even not converge at all) and with the complexity of the QCD interactions, such a description of intermediate energy ($Q^2 < 1 \text{ GeV}^2/c^2$) electron scattering is a sheer impossible task.

was obtained as a solution of Faddeev equations in ref. [18]. Faddeev equations are discussed in section 2.3.2.

Therefore, we have to resort to phenomenological models and effective theories in which nucleons and possibly pions, deltas and other hadrons are the fundamental degrees of freedom. Hadrons are not pointlike like the quarks in QCD; they have a nontrivial spatial structure. In most phenomenological models this structure is taken into account by non-local interactions (in configuration space) or momentum dependent form factors and vertex functions (in momentum space). Some of these quantities can be measured experimentally for free particles; *e.g.* the electromagnetic form factors of the proton are experimentally well-known from elastic H(e, e'p) and the NN-interaction can be constrained by NN scattering data. However, this information is in principle not sufficient for the description of hadrons and hadronic interactions inside a nucleus, which are off-shell and hence have a more complex structure. For an offshell nucleon the most general form of the electromagnetic vertex is [12]:

$$\Gamma_\mu(p', p) = \sum_{\substack{j=+,- \\ j'=+,-}} \Lambda_{j'}(p'^2) \left[F_1^{jj'} \gamma_\mu + \frac{i\sigma_{\mu\nu}q^\nu}{2M} F_2^{jj'} + q_\mu F_3^{jj'} \right] \Lambda_j(p^2), \quad (2.14)$$

which involves 12 so-called off-shell form factors $F_i^{jj'} = F_i^{jj'}(Q^2, W'^2, W^2)$ which depend on $Q^2 = -(p' - p)^2$, on the invariant masses $W'^2 = p'^2$ and $W^2 = p^2$, and on the choice of the electromagnetic gauge. The $\Lambda_\pm(p) = \frac{\pm\not{p} + W}{2W}$ operators project onto positive/negative energy states of mass W .

For the limiting case of a free nucleon ($\Lambda^+ = 1$, $\Lambda^- = 0$, $W = W' = M$) for which $F_{1,2}(Q^2) \equiv F_{1,2}^{++}(Q^2, M^2, M^2)$ are the so-called Pauli/Dirac form factors and $F_3^{++}(Q^2, M^2, M^2) = 0$ (which follows from invariance under space and time inversion), one has the linear combinations

$$G_E(Q^2) = F_1(Q^2) - \frac{\kappa Q^2}{4M^2} F_2(Q^2) \quad (2.15)$$

$$G_M(Q^2) = F_1(Q^2) + \kappa F_2(Q^2) \quad (2.16)$$

(where κ is the anomalous magnetic moment), as introduced by Sachs [13]. In the Breit frame, which is the coordinate frame in which $\mathbf{p}'_N = \mathbf{p}_N + \mathbf{q} = -\mathbf{p}_N$, G_E^n and G_M^n are closely related to the (Fourier transforms of the) charge density and the magnetic moment, respectively.

The off-shell form factors can be calculated in microscopic models, see for instance ref. [84]. It was shown *e.g.* in ref. [52, 59] that the part of the total scattering amplitude that is associated with off-shellness can be shifted to parts

associated with different reaction mechanisms by choosing a different representation of the intermediate fields in these models, while the total scattering amplitude remained invariant. Hence the form factors F_i^{jj} (for distinct values of Q^2 , W^2 and W'^2) are not observables, i.e. one cannot devise experiments to measure the evolution of these form factors in Q^2 , W^2 and W'^2 . However, they do have an overall effect on *e.g.* pion photoproduction cross sections, see refs. [33, 39, 41].

An important requirement for calculations of electromagnetic scattering reactions is that the total scattering amplitude is gauge invariant and (as a consequence) the total hadronic current is conserved. This is the case if all electromagnetic vertices satisfy the the Ward-Takahashi identity (WT) [8, 10], which establishes a relation between a hadronic vertex with n lines and the same vertex with $n + 1$ lines, where the extra line is a photon line. For the $\gamma^* NN$ vertex ($n = 2$) the WT identity reads

$$(p' - p)^\mu \Gamma_\mu(p', p) = e [S^{-1}(p') - S^{-1}(p)]. \quad (2.17)$$

where $S(p) = i(\not{p} - M_N - \Sigma(p))^{-1}$ is the (full) nucleon propagator ($\Sigma(p)$ denotes the self-energy of the nucleon). With this identity the F_3^{jj} form factors may be eliminated, leaving eight independent form factors and $\Gamma_\mu(p', p)$ reduces to

$$\Gamma_\mu(p', p) = \sum_{\substack{j=+,- \\ j'=+,-}} \Lambda_j(p'^2) \left[F_1^{jj} \gamma_\mu + \frac{i\sigma_{\mu\nu} q^\nu}{2M} F_2^{jj} + \left((1 - F_1^{jj}) \not{q} + \Delta\Sigma \right) q_\mu / q^2 \right] \Lambda_j(p^2), \quad (2.18)$$

where $\Delta\Sigma = \Sigma(p) - \Sigma(p')$. The WT identity only applies to the longitudinal part of the current operators. There is no unique prescription to obtain from a given hadronic vertex the transverse part of the corresponding many-body current [99]; but different prescriptions lead to different results. This is part of a general problem with gauge invariance, off-shellness and the structure of hadrons in phenomenological models, outlined for instance in ref. [95].

The electromagnetic interaction is so weak that we can safely assume that only one virtual photon is exchanged between the electron and the nucleus. In a plane-wave impulse approximation (PWIA) (see section 2.3.1) it is assumed that the energy and momentum of the photon are completely absorbed by one particle which then escapes the nucleus without further interaction. However, the coupling constants of the strong interactions are so large that for many processes, in particular those involving few-body systems, this is not a good approximation: after absorption of the virtual photon the hadrons in a nucleus

may undergo so-called final state interactions (FSI) before reaching the final state that will be measured by the particle detectors.

Summarizing: we are in need of gauge invariant calculations of intermediate energy ($Q^2 < 1 \text{ GeV}^2/c^2$) electromagnetic scattering reactions that take into account FSI as well as the off-shellness of the bound hadrons in the initial state. The necessity of Lorentz covariance depends on the precision and kinematics of the experiment.

We invited Nagorny and Golak to perform such calculations for our experiment. In section 2.3.2 the calculations of Golak are described, which take the FSI into account to all orders but both the kinematics and the current operator are nonrelativistic. In section 2.3.3 the approach of Nagorny is discussed. This formalism is an attempt to give a gauge invariant, Lorentz covariant description of electron scattering on ^3He (and other small nuclei) but the FSI effects are calculated for each number of loops separately, with rapidly increasing degree of complexity. Hence, in its present form only the one-loop calculations can be done with all relevant partial waves and two-loop only with a subset of the partial waves.

In both models, the electromagnetic coupling to the nucleon is the free nucleon coupling. In Golak's nonrelativistic calculations the 'off-mass-shellness' is undefined. In Nagorny's model the off-shell effects are absorbed into the many-body current.

All calculations were done twice, once with G_E^n equal to the Galster parametrization (see section 2.5) and once with $G_E^n \equiv 0$. In a comparison with the experimental data a value for G_E^n is then extracted by using a linear interpolation or extrapolation. This extracted G_E^n value may be meaningful *only if* the predictions in other observables and/or other channels agree sufficiently well with the experimental data. This is discussed further in chapter 5.

2.3.1 PWIA(S)

In a description based on the plane wave impulse approximation (PWIA) the $^3\text{He}(e, e'n)$ reaction the virtual photon is assumed to be absorbed by the neutron which subsequently leaves the nucleus without interacting with the protons. This approximation works surprisingly well for many low-energy and intermediate energy single nucleon knock-out reactions and inclusive scattering.

The probability distribution for the energy and momentum of the neutron within the nucleus prior to the interaction is determined by that of the miss-

ing energy E_m and momentum p_m , the so-called spectral function $S(E_m, \mathbf{p}_m)$. This spectral function is usually derived from a ground state wave function obtained from a solution of the Faddeev equations (2.37). Hence in the PWIA the neutron is treated as a free particle³ and ${}^3\text{He}(e, e'n)$ is described as electron-neutron scattering, folded with a spectral function:

$$\frac{d^6\sigma_{PWIA}}{d\mathbf{p}_n d\mathbf{k}'_e} = S(E_m, \mathbf{p}_m) \frac{d^6\sigma_{en}}{d\mathbf{p}_n d\mathbf{k}'_e}. \quad (2.19)$$

As is explained in section 2.2 the neutron effectively carries the spin of the ${}^3\text{He}$ nucleus for 90% of the ground state wave function and hence in PWIA the properties of the quasi-elastic ${}^3\text{He}(\vec{e}, e'n)$ process largely coincide with those of elastic electron-neutron scattering. The cross section for elastic electron scattering on polarized free neutrons (in the rest frame of the initial state neutrons) can be written in the same form as equation (2.2):

$$\frac{d^2\sigma_{en}}{d\Omega_{e'}} = \frac{d^2\sigma_0}{d\Omega_{e'}} [1 + hA_n^e + \mathbf{A}_n^0 \cdot \mathbf{P}_n + h\mathbf{A}'_n \cdot \mathbf{P}_n], \quad (2.20)$$

with

$$\frac{d^2\sigma_0}{d\Omega_{e'}} = \frac{d^2\sigma_{Mott}}{d\Omega_{e'}} f_{rec}^{-1} \left[\frac{G_E^{n2} + \tau G_M^{n2}}{1 + \tau} + 2\tau \tan^2(\frac{1}{2}\theta_e) \right], \quad (2.21)$$

$$f_{rec} = 1 + \frac{2E}{M_n} \sin^2(\frac{1}{2}\theta_e), \quad (2.22)$$

$$A'_{n,x} = \frac{2 \tan(\frac{1}{2}\theta_e) \sqrt{\tau(1+\tau)} G_E^n G_M^n}{G_E^{n2} + \tau G_M^{n2} + 2\tau(1+\tau) \tan^2(\frac{1}{2}\theta_e)}, \quad (2.23)$$

$$A'_{n,y} = 0, \quad (2.24)$$

$$A'_{n,z} = \frac{2 \tan(\frac{1}{2}\theta_e) \tau \sqrt{1+\tau + (1+\tau)^2 \tan^2(\frac{1}{2}\theta_e)} G_M^{n2}}{G_E^{n2} + \tau G_M^{n2} + 2\tau(1+\tau) \tan^2(\frac{1}{2}\theta_e)}, \quad (2.25)$$

$$\mathbf{A}_n^0 = \mathbf{0}. \quad (2.26)$$

The Cartesian coordinates for the spin degrees of freedom (\mathbf{A}'_n , \mathbf{A}_n^0 and \mathbf{P}^n) are again defined as in equation (2.10) or figure 1. In equation (2.21) σ_{Mott} denotes

³This seemingly simple assumption is actually ambiguous. As was shown in ref. [26], there is no preferred method to restore current conservation with this assumption; and moreover, prior to photon absorption the neutron is manifestly off-shell. In many PWIA calculations, and also in the following, we use the electromagnetic coupling of a free nucleon, but this a choice which is by no means theoretically compulsory.

the cross section for unpolarized elastic scattering of point-like fermions (see ref. [3]) and $\tau = Q^2/4M_n^2$.

The asymmetries $A_{n,x}^0$, $A_{n,z}^0$ and $A'_{n,y}$ vanish because of reflection symmetry in the scattering plane. The electron asymmetry A_e and the target asymmetry $A_{n,y}^0$ should vanish because of time reversal symmetry.

The cross section for unpolarized scattering only contains terms proportional to the square of G_E^n , which are dominated by the much larger τG_M^n terms; hence it is hard to extract G_E^n from unpolarized electron scattering data. On the other hand, the sideways asymmetry, equation (2.23), contains an interference term proportional to $G_M^n G_E^n$ which seems to offer a much better opportunity for G_E^n extraction. Moreover, by measuring both $A'_{n,x}$ and $A'_{n,z}$ and determining their ratio we get an expression which is proportional to G_E^n/G_M^n and does not even depend on the absolute values of the electron helicity h and the target polarization P . This was the driving motivation for the early ${}^3\text{He}(\vec{e}, e'n)$ experiments [48].

In a *symmetrized* PWIA (PWIAS), the photon can also be absorbed by one of the protons. The electron-proton cross section is almost an order of magnitude larger than the electron-neutron cross section but for only a small part of the wave function the neutron has a momentum of the order of a few hundred MeV/c within the solid angle of our detector. As it turns out (see figure 2.7) the contribution of the protons leads to an offset in the A'_x asymmetry as compared to the PWIA prediction.

2.3.2 Faddeev equations

Ground state wave function

The Hamiltonian for the three nucleon system reads

$$H = H_0 + V_1 + V_2 + V_3, \quad (2.27)$$

where H_0 is free Hamiltonian (kinetic energy of the three nucleons) and the $V_i = v_{jk}$ (in this section (ijk) is always a cyclic permutation of (123)) describe the NN pair interactions. Possible three-nucleon interactions can also be incorporated straightforwardly. For a bound 3N state $|\Psi_{3N}^b\rangle$ the Schrödinger equation $H|\Psi_{3N}^b\rangle = E|\Psi_{3N}^b\rangle$ may be rewritten as

$$|\Psi_{3N}^b\rangle = G_0(E)(V_1 + V_2 + V_3)|\Psi_{3N}^b\rangle \quad (2.28)$$

$$= |F_1\rangle + |F_2\rangle + |F_3\rangle, \quad (2.29)$$

where $G_0(z) \equiv (z - H_0)^{-1}$ is the resolvent operator of the free Hamiltonian and for the Faddeev components $|F_i\rangle$ we have

$$|F_i\rangle \equiv G_0 V_i |\Psi_{3N}^b\rangle \quad (2.30)$$

$$= G_0 V_i (|F_i\rangle + |F_j\rangle + |F_k\rangle) \quad (2.31)$$

$$= (1 - G_0 V_i)^{-1} G_0 V_i (|F_j\rangle + |F_k\rangle) \quad (2.32)$$

$$= G_0 t_i (|F_j\rangle + |F_k\rangle), \quad (2.33)$$

where in equation (2.31) the formal solution (2.29) was reused. In (2.33) the nucleon-nucleon t -matrix was introduced:

$$t_i \equiv V_i + V_i G_0 V_i + V_i G_0 V_i G_0 V_i + \dots \quad (2.34)$$

$$= V_i + V_i G_0 t_i \quad (2.35)$$

$$= (1 - V_i G_0)^{-1} V_i. \quad (2.36)$$

As the ${}^3\text{He}$ nucleus consists of three identical fermions (nucleons) with mass M_N , the Faddeev components $|F_i\rangle$ can be transformed into each other with cyclic permutation \tilde{P}_c of all quantum numbers of the three nucleons: $|F_j\rangle = \tilde{P}_c |F_i\rangle$, $|F_k\rangle = \tilde{P}_c^2 |F_i\rangle$. With $\tilde{P} = \tilde{P}_c + \tilde{P}_c^2$ equation (2.33) can be rewritten as

$$|F_i\rangle = G_0 t_i \tilde{P} |F_i\rangle. \quad (2.37)$$

From a solution of this equation for any i the bound state wave function is obtained with

$$|\Psi_{3N}^b\rangle = (1 + \tilde{P}) |F_i\rangle. \quad (2.38)$$

The Faddeev equations (2.37) are simpler than the original equation (2.28) because they involve only one pair interaction, but they are still challenging. In momentum space, with Jacobi momenta

$$\mathbf{p}_i = \frac{1}{2}(\mathbf{k}_j - \mathbf{k}_k), \quad (2.39)$$

$$\mathbf{q}_i = \frac{2}{3} \left[\mathbf{k}_i - \frac{1}{2}(\mathbf{k}_j + \mathbf{k}_k) \right], \quad (2.40)$$

and discrete quantum numbers α (angular momentum, isospin) they read

$$\begin{aligned} \langle pq\alpha | F_i \rangle &= \frac{1}{E - p^2/M_N - 3q^2/4M_N} \quad (2.41) \\ &\times \sum_{\alpha'} \int dp' p'^2 \int dq' q'^2 \langle pq\alpha | t_i | p' q' \alpha' \rangle \\ &\times \sum_{\alpha''} \int dp'' p''^2 \int dq'' q''^2 \langle p' q' \alpha' | \tilde{P} | p'' q'' \alpha'' \rangle \langle p'' q'' \alpha'' | F_i \rangle. \end{aligned}$$

These integral equations were solved for several NN-potentials, see *e.g.* refs. [15, 22, 45].

Rescattering to all orders after photon absorption

The asymmetry of the cross section for polarized electron scattering with respect to the electron helicity $h = \pm 1$ can be expressed in terms of the response functions defined by Raskin & Donnelly [36]:

$$A = \frac{\int d\Omega_{pp} (v_{TL'} R^{TL'} + v_{T'} R^{T'})}{\int d\Omega_{pp} (v_L R^L + v_T R^T + v_{TT} R^{TT} + v_{TL} R^{TL})}, \quad (2.42)$$

where $R^{TL'}$ and $R^{T'}$ depend on the orientation of the ^3He spin \mathbf{S} . The v_* symbols denote kinematic factors. For \mathbf{S} parallel or perpendicular to the momentum transfer \mathbf{q} the asymmetry A is equal to A'_z and A'_x , respectively. The integral is over the direction of the relative momentum of the two undetected protons (the magnitude of this momentum is fixed by energy conservation).

As listed in ref. [36], the six response functions in equation (2.42) are a (linear combination of two) product(s) of two matrix elements of the nuclear current operator $J(q)$

$$N_\mu = \langle \Psi_f^{(-)} | J_\mu(q) | \Psi_{^3\text{He}} \rangle. \quad (2.43)$$

Like the ground state wave function $|\Psi_{^3\text{He}}\rangle$, the 3N scattering state $|\Psi_f^{(-)}\rangle$ must be an eigenstate of the full Hamiltonian of eq. (2.27). As we are interested in (e, e'n) we focus on eigenstates in which the nucleons are asymptotically free, with Jacobi momenta \mathbf{p}_i and \mathbf{q}_i . Let $|\phi_{\mathbf{p}_i, \mathbf{q}_i}\rangle$ be an anti-symmetric free 3N state constructed as $(1 + \tilde{P})|\mathbf{p}_i\rangle_a |\mathbf{q}_i\rangle$, where the state $|\mathbf{p}_i\rangle_a |\mathbf{q}_i\rangle$ is an eigenstate of H_0 , antisymmetric under $j \leftrightarrow k$, with energy eigenvalue $E = \mathbf{p}_i^2/M + 3\mathbf{q}_i^2/4M$. We obtain a corresponding state $|\Psi_f^{(-)}\rangle$ by projecting $|\phi_{\mathbf{p}_i, \mathbf{q}_i}\rangle$ onto the eigenstates of the full Hamiltonian with the same energy E :

$$|\Psi_f^{(-)}\rangle = \lim_{\epsilon \downarrow 0} \frac{i\epsilon}{E + i\epsilon - H} |\phi_{\mathbf{p}_i, \mathbf{q}_i}\rangle = \lim_{\epsilon \downarrow 0} i\epsilon G(E + i\epsilon) |\phi_{\mathbf{p}_i, \mathbf{q}_i}\rangle \quad (2.44)$$

where $G(z) = (z - H)^{-1}$ is the resolvent operator of the full Hamiltonian. Using⁴

$$G = G_0 + G_0 V G = G_0 + G_0 (1 + \tilde{P}) V_i G \quad (2.45)$$

⁴For readability we drop from here on the argument of G and G_0 ; in equation (2.45) an arbitrary argument z is understood, while in (2.46) and later G and G_0 an argument E (the total kinetic energy of the final state free nucleons) is understood. Of course, we have dropped many more indices and quantum numbers; otherwise all formulae would be cluttered up like equation (2.41).

and the fact that $\lim_{\epsilon \downarrow 0} i\epsilon G_0(E + i\epsilon)$ leaves the state $|\phi_{\mathbf{p}_i \mathbf{q}_i}\rangle$ invariant we can write

$$|\Psi_f^{(-)}\rangle = |\phi_{\mathbf{p}_i \mathbf{q}_i}\rangle + G_0(1 + \tilde{P})V_i|\Psi_f^{(-)}\rangle \quad (2.46)$$

$$= (1 + \tilde{P})|\psi_i\rangle, \quad (2.47)$$

with the Faddeev components

$$|\psi_i\rangle = |\mathbf{p}_i\rangle_a |\mathbf{q}_i\rangle + G_0 V_i |\Psi_f^{(-)}\rangle \quad (2.48)$$

$$= |\mathbf{p}_i\rangle_a |\mathbf{q}_i\rangle + G_0 V_i (1 + \tilde{P}) |\psi_i\rangle \quad (2.49)$$

$$= (1 - G_0 V_i)^{-1} |\mathbf{p}_i\rangle_a |\mathbf{q}_i\rangle + (1 - G_0 V_i)^{-1} G_0 V_i \tilde{P} |\psi_i\rangle \quad (2.50)$$

$$= (1 + G_0 t_i) |\mathbf{p}_i\rangle_a |\mathbf{q}_i\rangle + G_0 t_i \tilde{P} |\psi_i\rangle \quad (2.51)$$

$$= |\mathbf{p}_i\rangle_a |\mathbf{q}_i\rangle + G_0 t_i [1 - \tilde{P} G_0 t_i]^{-1} (1 + \tilde{P}) |\mathbf{p}_i\rangle_a |\mathbf{q}_i\rangle. \quad (2.52)$$

The Faddeev components (2.52) can be inserted back into (2.47) and (2.43), so that we can decompose the nuclear current in a PWIA term and rescattering terms:

$$N_\mu = N_\mu^{\text{PWIAS}} + N_\mu^{\text{rescat}}, \quad (2.53)$$

$$N_\mu^{\text{PWIAS}} = \langle \phi_{\mathbf{p}_i \mathbf{q}_i} | J_\mu(q) | \psi_{^3\text{He}} \rangle, \quad (2.54)$$

$$N_\mu^{\text{rescat}} = \langle \phi_{\mathbf{p}_i \mathbf{q}_i} | [1 - t_i G_0 \tilde{P}]^{-1} t_i G_0 (1 + \tilde{P}) J_\mu(q) | \psi_{^3\text{He}} \rangle \quad (2.55)$$

$$= \langle \phi_{\mathbf{p}_i \mathbf{q}_i} | U_\mu \rangle, \quad (2.56)$$

$$|U_\mu\rangle = t_i G_0 (1 + \tilde{P}) J_\mu(q) | \psi_{^3\text{He}} \rangle + t_i G_0 \tilde{P} |U_\mu\rangle. \quad (2.57)$$

The rescattering term (2.56) is completely determined by the rescattering state $|U_\mu\rangle$. As suggested by the nomenclature, the terms in the geometrical series (2.57) are interpreted as processes in which the ^3He nucleus absorbs a photon and the nucleons "rescatter" one or more times. Following this interpretation, the terms of the full current (2.53) up to second order are graphically illustrated in figure 2.2. In this figure the electromagnetic current operator $J(q)$ is just the sum of the single nucleon current operators.

The first numerical evaluations of the solutions of the continuum Faddeev equations were obtained by Van Meijgaard and Tjon [42, 37] using a simple S-wave NN interaction and using the relativistic one-nucleon currents. The Bochum nuclear theory group has undertaken the effort of solving equation (2.56) (and deriving predictions for observables such as cross sections and asymmetries) with 'realistic NN potentials' such as the Bonn [32] and the Argonne V18 [50] potentials. They employ a current operator composed of non-

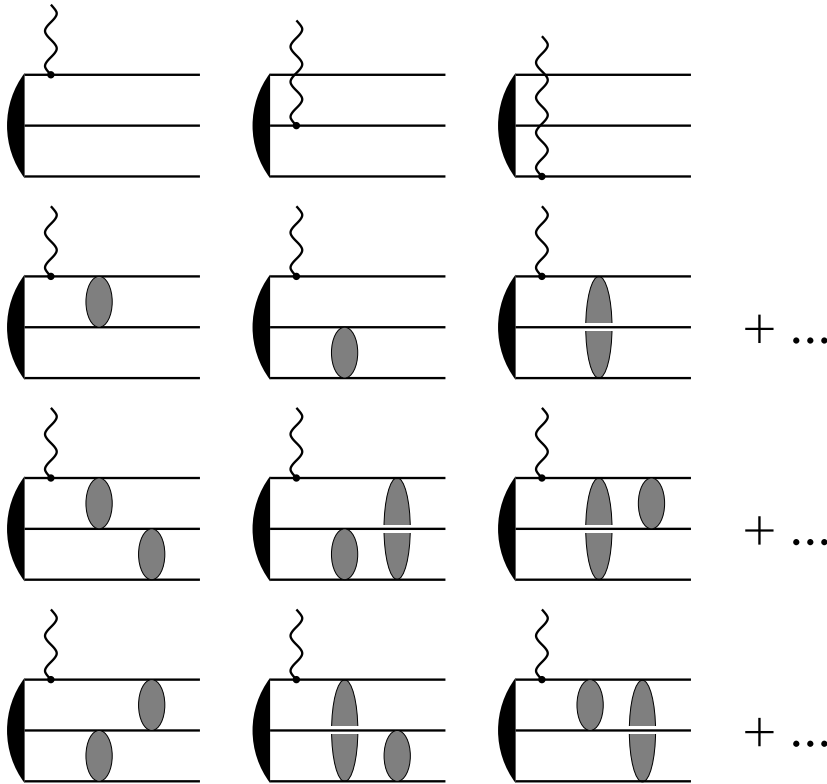


Figure 2.2: Symbolic representation of the terms of N_μ (up to second order in t_i). The horizontal lines represent nucleon states, the wavy line represents a photon coupling to one of the nucleons, the black blob on the left of each diagram represents the initial ${}^3\text{He}$ groundstate wave function and the grey blobs represent full NN-interactions (corresponding to t_i factors in the formulae). The “+ ...” after the first and second order diagrams indicate that two similar sets of diagrams are implied with the photon line attached to the second and third nucleon, respectively.

relativistic reduction of the one-nucleon currents plus Magnetic Exchange Currents (or Meson Exchange Currents, both abbreviated as MEC) which are obtained from the NN-potential following the Riska prescription [29].

The independent components of the nuclear current N_μ are

$$N_0 = \langle \Psi_f^{(-)} | \hat{\rho}(\mathbf{q}) | \Psi_{^3\text{He}} \rangle, \quad (2.58)$$

$$N_{\pm 1} = \langle \Psi_f^{(-)} | J_{\pm 1}(\mathbf{q}) | \Psi_{^3\text{He}} \rangle \quad (2.59)$$

$$= \langle \Psi_f^{(-)} | J_x(\mathbf{q}) \pm iJ_y(\mathbf{q}) | \Psi_{^3\text{He}} \rangle, \quad (2.60)$$

while the component parallel to \mathbf{q} is fixed by requiring current conservation: $N_z = \omega N_0 / |\mathbf{q}|$. With an exact, gauge invariant calculation of the nuclear current this requirement is naturally fulfilled. It would be interesting to check, at least for a limited number of cases, whether or not the current as calculated by Golak *et al.* is conserved or not, by explicitly calculating N_z , but there are presently no plans for such a project [97].

An investigation of the relative importance of the contribution of the rescattering terms to the calculated cross section of $^3\text{He}(e, e'p)$ [53] shows that (for that investigated process) the rescattering series did not converge to the full result (and to the experimental data) until fourth or fifth order. This is a strong illustration of the necessity to take FSI into account in the analysis and interpretation of few-body break-up reactions; but it is also surprising that despite the fact that the amplitude is dominated by these rescattering terms the effect of the electromagnetic structure of the neutron on the A_x^i observable is *not washed out*. This can be seen in the results of the Monte Carlo simulations of our experiment (see section 5) and *e.g.* in refs. [96, 91].

2.3.3 Lorentz covariant approach of Nagorny

Nagorny took a field-theoretical approach in order to obtain a Lorentz covariant and gauge invariant way to calculate amplitudes for electromagnetic processes on nuclear systems, with consistent allowance for their internal structure. This overview of the formal background of his calculations is loosely based on refs. [38, 64].

For the calculation of transition amplitude of a system of m initially free particles interacting with each other, resulting in a system of $n - m$ particles, we need to calculate the matrix element $\langle 0 | \phi_n \dots \phi_{m+1} S \phi_m^\dagger \dots \phi_1^\dagger | 0 \rangle$, where the $\phi_i^{(\dagger)}$'s are field operators corresponding to the particles in the initial and final state and S is the 'scattering matrix' which lets a state evolve from the infinitely

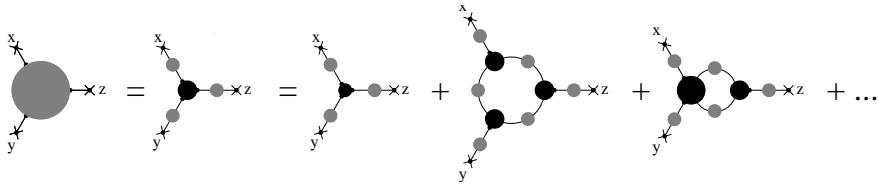


Figure 2.3: A full 3-point Green's function can be decomposed into terms of 2-point full Green's functions (grey blobs) and a 3-point irreducible Green's function (vertex function, black blob); which in turn can be decomposed further into a 2-particle irreducible vertex and loop diagrams, and so on.

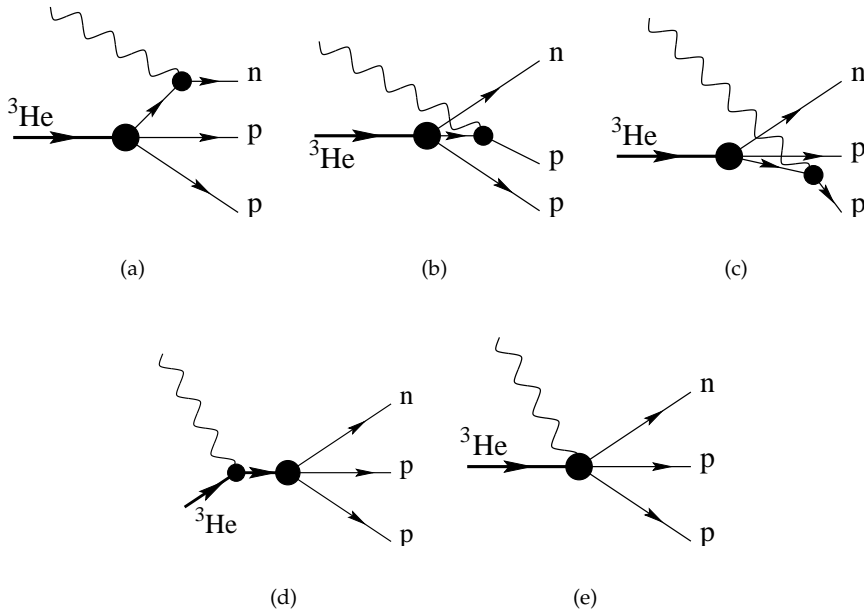


Figure 2.4: Lowest order diagrams in the the calculations of Nagorny.

remote past to the infinitely distant future. Via so-called reduction formulas (see *e.g.* ref. [19, 23]) these amplitudes can be expressed in terms of the general Green's functions of the interacting theory. An n -point Green's function is the vacuum expectation value of the time-ordered product of n field operators Φ_i :

$$G^{(n)}(x_1, \dots, x_n) = \langle 0 | T (\Phi_1(x_1) \dots \Phi_n(x_n)) | 0 \rangle. \quad (2.61)$$

For $n > 2$ such a Green's function may be decomposed in terms of full 2-point Green's functions ('propagators') and *irreducible* Green's functions ('vertex functions'). For the 3-point Green's function we get just one term:

$$G^{(3)}(x_1, x_2, x_3) = \int d\xi_1 d\xi_2 d\xi_3 \Gamma^{(3)}(\xi_1, \xi_2, \xi_3) G^{(2)}(x_1, \xi_1) G^{(2)}(x_2, \xi_2) G^{(2)}(x_3, \xi_3) \quad (2.62)$$

This is graphically illustrated in figure 2.3. In a further decomposition we would get more than one term, namely a two-particle irreducible Green's function and a number of terms corresponding to graphs with loops. A Green's function is called m -particle irreducible if its further decomposition contains (in a graphical representation) no diagrams that can be split into disconnected parts by removing only m internal lines. Which terms actually contribute and how much depends on the properties of the fields and their dynamics, which may be derived for instance from a Lagrangian. In a momentum representation vertex functions can only be a constant function (no momentum dependence) if all its associated fields correspond to pointlike particles.

The 5-point Green's function for ${}^3\text{He}(\gamma^*, n)\text{pp}$ can be decomposed into expressions graphically illustrated in figure 2.4. The wavy lines denote photon propagators, the lines with an arrow denote fermion (nucleon or ${}^3\text{He}$ nucleus) propagators. The terms illustrated in panels (a)...(d) are interpreted as one-body processes/currents, while (e), the 'contact term', constitutes the many-body currents (or the "contact current").

These expressions can be evaluated numerically by using parametrizations of the propagators and vertex functions based on experimental input and/or theoretical models. The numerical evaluations (of each of the one-body currents and the contact term separately) depend on the choice for the electromagnetic gauge. However, the total scattering amplitude is gauge invariant if the vertex functions and propagators satisfy the appropriate Ward-Takahashi identities (WT) [8, 10], which relate every n -point Green's function of hadronic fields to the corresponding $(n + 1)$ -point Green's function (where the extra field is the electromagnetic field).

For the $\Gamma_{\text{He,p,p,n}}^{(4)}$ vertex function a parametrization based on the ${}^3\text{He}$ ground state wave function (see section 2.2) is used. The wave function was obtained by Hajduk [27] as a solution of the (nonrelativistic) Faddeev equations using the Reid soft-core NN potential. This wave function was chosen because it has a separable form which allows a covariant formulation. A drawback is that it involved only 5 channels (S and S'), which means that Nagorny's calculations are less reliable for large missing momenta ($p_m > 150 \text{ MeV}/c$).

For the vertex function $\Gamma_\mu \equiv (\Gamma_{\gamma^*, N, N}^{(3)})_\mu$ corresponding to the electromagnetic coupling to the nucleon we already mentioned the implications of the WT identity on page 13. We may write the half-off-shell vertex ($p'^2 = M^2$, $p^2 \neq M^2$) as:

$$\Gamma_\mu(p', p) = \Gamma_\mu^+(q^2, p^2)\Lambda^+ + \Gamma_\mu^-(q^2, p^2)\Lambda^- \quad (2.63)$$

where

$$\Gamma_\mu^\pm(q^2, p^2) = F_1^{\pm\pm}\gamma_\mu + (1 - F_1^{\pm\pm}) \not{q}q_\mu/q^2 + \frac{i\sigma_{\mu\nu}q^\nu}{2M}F_2^{\pm\pm} \quad (2.64)$$

and we have put $\Sigma(p) = \Sigma(p') = 0$. In diagrams 2.4(a,b,c) this vertex is multiplied with the propagator $S(p) = i(\not{p} - M_N)^{-1}$ (corresponding to the off-shell nucleon); this leads to

$$\Gamma_\mu(p', p)S(p) = \Gamma_\mu^+(q^2, p^2)S(p) + \frac{1}{2M}(\Gamma_\mu^+(q^2, p^2) - \Gamma_\mu^-(q^2, p^2)) \quad (2.65)$$

$$\begin{aligned} &= \Gamma_\mu^+(q^2, M^2)S(p) + (p^2 - M^2)\frac{\partial\Gamma_\mu^+}{\partial p^2}(p^2, M^2)S(p) + \dots \\ &\quad + \frac{1}{2M}(\Gamma_\mu^+(q^2, p^2) - \Gamma_\mu^-(q^2, p^2)) \end{aligned} \quad (2.66)$$

A similar decomposition can be made for the fully off-shell Γ_μ . We see in equation (2.66) that the terms associated with off-shellness do not have a pole in $p^2 = M^2$: in the Taylor expansion the powers of $p^2 - M^2$ eliminate the pole of $S(p)$, and the last term contains no propagator $S(p)$. It is argued by Nagorny [64] that only the pole terms should be interpreted as one-body currents and the regular parts as many-body currents. From this he concludes that one should only use the on-shell form factors (as in the first term of equation (2.66)) in the calculation of the one-body currents (the diagrams in figure 2.4(a,b,c)); the off-shell terms should be absorbed into the contact current (figure 2.4(e)) and need not to be calculated separately.

This contact current is essentially unknown. It must be determined via a decomposition of the one-particle irreducible vertex into loops (see figure 2.5)

and a two-particle reducible vertex. In the loop diagrams also a different kind of 'contact term' appears (figure 2.5(d)) arising from the NN interaction vertex. These contact terms are again unknown and have to be expanded in loops and vertices of higher irreducibility. This repeating procedure can be terminated by only fixing the longitudinal part of the contact terms with the WT identity and using a prescription for the transversal part. For the case of deuteron disintegration this procedure has been worked out in detail in ref. [38]. The hope is that by applying the prescription at the one- or two-loop level yields a better approximation of the exact scattering amplitudes than when the same prescription would be applied in the lowest order calculation.

The expansion of the (Lorentz covariant) contact terms into terms corresponding to loop diagrams is to some degree comparable to the (nonrelativistic) rescattering series in the Faddeev equation (see equation (2.56) and figure 2.2). For the latter it was found that a calculation of the rescattering to first or second order is often not sufficient (see page 21). However, a covariant calculation to two loops is already an enormous effort. Despite years of extensive research a Lorentz covariant formulation of the Faddeev equation has not yet been found.

Summary

Formally, the scattering amplitude for ${}^3\text{He}(\gamma^*, n)pp$ is exactly equal to the sum of the (analytical expressions corresponding to the) diagrams in figure 2.4. The longitudinal part of the contact term, which contains all many-body (and off-shell) effects, is partly constrained by the Ward-Takahashi identity (requirement for gauge invariance). However, the decomposition in a longitudinal and a transversal part is only unique up to an arbitrary transversal function. This ambiguity can be deferred by expanding the contact term in loop terms, which can be carried out to second order. A prescription is then used to fix the transversal part of the contact terms.

2.4 Asymmetry measurements

While in a theoretical description all momenta are exactly given and the polarizations are 100%, in an experiment one has finite acceptances, fluctuating parameters and finite resolutions. We can not measure at exactly one point in phase space, we accumulate data over the finite acceptance of the detectors, which translates to a finite region in phase space, folded with detector efficien-

cies which are not necessarily constant over the acceptance. Some regions of the phase space may be better ‘covered’ than others. The splitting up of the phase space in smaller bins, in order to approach the ideal of “points” in phase space, is not only limited by resolution, but also by statistics.

In an experiment with a polarized target, the finite acceptance also affects the effective direction of the spin of the target nucleus. In the laboratory, the spin is aligned to a constant, homogeneous magnetic holding field with a particular angle with respect to the *central* momentum transfer vector \mathbf{q} . A generic event will have a \mathbf{q} different from the central \mathbf{q} and hence be sensitive to a different (combination of) spin correlation function(s) than the one “aimed” at by the central \mathbf{q} .

The expected number of events during a measuring period T_i (during which the target spin is aligned along $\hat{\mathbf{S}}^{\text{lab}}$) is⁵:

$$N_i = \int_{T_i} dt \int d^n k \mathcal{L}(t) \eta(k, t) \varphi(k) \frac{d^n \sigma_0}{dk^n} \mathcal{A}(k) \cdot \mathcal{P}(t), \quad (2.67)$$

where

$k = (k_1, \dots, k_n)$: set of independent relevant kinematical variables
e.g. $E_e, \theta_e, \phi_e, T_n, \theta_{pq}, \phi_{pq}$

$\mathcal{L}(t)$: luminosity (beam current \times target thickness)

$\eta(k, t)$: product of the detector efficiencies and DAQ live time

$\varphi(k)$: phase space factor and cuts

$\frac{d^n \sigma_0}{dk^n}$: unpolarized differential cross section

$$\mathcal{P}(t) = (1, h(t), S(t), h(t)S(t)) \quad (2.68)$$

$$\mathcal{A}(k) = \begin{pmatrix} 1 \\ A_e(k) \\ A^0(k) \\ A'(k) \end{pmatrix} \quad (2.69)$$

$$\mathbf{S}(t) = \hat{\mathbf{S}}^{\text{lab}} S(t)$$

$$A^0(k) = \left(A_x^0(k) \hat{\mathbf{x}}^{\text{lab}}(\mathbf{q}) + A_y^0(k) \hat{\mathbf{y}}^{\text{lab}}(\mathbf{q}) + A_z^0(k) \hat{\mathbf{z}}^{\text{lab}}(\mathbf{q}) \right) \cdot \hat{\mathbf{S}}^{\text{lab}} \quad (2.70)$$

$$A'(k) = \left(A'_x(k) \hat{\mathbf{x}}^{\text{lab}}(\mathbf{q}) + A'_y(k) \hat{\mathbf{y}}^{\text{lab}}(\mathbf{q}) + A'_z(k) \hat{\mathbf{z}}^{\text{lab}}(\mathbf{q}) \right) \cdot \hat{\mathbf{S}}^{\text{lab}}. \quad (2.71)$$

⁵Note that the “measuring periods” are usually heavily intertwined. In our experiment, the target spin was flipped every few minutes (during injection) while the beam helicity was flipped typically every hour (between runs)

If we assume that the efficiency factor may be factorized: $\eta(k, t) = \eta_k(k)\eta_t(t)$, then the integral can be reexpressed in terms of time averages of the polarizations, acceptance averages of the spin correlation functions and the collected charge:

$$N_i/Q_i = \overline{\mathcal{P}_i} \cdot \overline{\sigma \mathcal{A}} \quad (2.72)$$

$$= \overline{\mathcal{P}_i} \cdot \overline{\mathcal{A} \overline{\sigma}_0} \quad (2.73)$$

$$Q_i = \int_{T_i} dt \mathcal{L}(t) \eta_t(t) \quad (2.74)$$

$$\overline{\mathcal{P}_i} = \int_{T_i} dt \mathcal{L}(t) \eta_t(t) \mathcal{P}(t) / Q_i \quad (2.75)$$

$$= (1, \overline{h}_i, \overline{P}_i, \overline{hP}_i) \quad (2.76)$$

$$\overline{\sigma}_0 = \int d^n k \eta_k(k) \varphi(k) \frac{d^n \sigma_0}{dk^n} \quad (2.77)$$

$$\overline{\mathcal{A}} = \left(\begin{array}{c} 1 \\ \overline{A}_e \\ \overline{A}^0 \\ \overline{A}' \end{array} \right) = \overline{\sigma \mathcal{A}} / \overline{\sigma}_0 \quad (2.78)$$

$$= \int d^n k \eta_k(k) \varphi(k) \frac{d^n \sigma_0}{dk^n} \mathcal{A}(k) / \overline{\sigma}_0. \quad (2.79)$$

The quantities \overline{A}_e , \overline{A}^0 and \overline{A}' are determined both from the experimental data ($N_{i=1\dots 4}$, $\mathcal{P}_{i=1\dots 4}$ and $Q_{i=1\dots 4}$) and from a theoretical model, which provides $\mathcal{A}(k)$ for which the integration (2.79) is performed numerically in a so-called Monte Carlo simulation.

Experimental determination of asymmetries

In the four measuring periods T_i , with polarizations \mathcal{P}_i and integrated luminosity Q_i , we collect N_i ${}^3\text{He}(e, e'n)$ events. The acceptance averaged spin correlation functions are then obtained by solving the set of four equations (2.72), explicitly:

$$(\overline{\sigma}_0, \overline{\sigma}_0 \overline{A}_e, \overline{\sigma}_0 \overline{A}^0, \overline{\sigma}_0 \overline{A}') = \overline{\sigma \mathcal{A}} = \mathcal{M}_P^{-1} \cdot \mathcal{N}, \quad (2.80)$$

with

$$\mathcal{M}_P = \begin{pmatrix} \overline{P}_1 \\ \overline{P}_2 \\ \overline{P}_3 \\ \overline{P}_4 \end{pmatrix} = \begin{pmatrix} 1 & \overline{h}_1 & \overline{P}_1 & \overline{hP}_1 \\ 1 & \overline{h}_2 & \overline{P}_2 & \overline{hP}_2 \\ 1 & \overline{h}_3 & \overline{P}_3 & \overline{hP}_3 \\ 1 & \overline{h}_4 & \overline{P}_4 & \overline{hP}_4 \end{pmatrix} \quad (2.81)$$

$$\mathcal{N} = \begin{pmatrix} n_1 \\ n_2 \\ n_3 \\ n_4 \end{pmatrix} = \begin{pmatrix} N_1/Q_1 \\ N_2/Q_2 \\ N_3/Q_3 \\ N_4/Q_4 \end{pmatrix}. \quad (2.82)$$

The optimal (and most obvious) choice for the polarization settings is to ‘flip’ the beam and/or target polarizations between measuring periods $T_i = T_{\pm\pm}$. In the ideal case that the magnitudes of the average beam and target polarizations are the same for all four datasets, equation (2.80) reduces to the simple asymmetry expressions (2.12...2.13). If we neglect the (uncertainty in) the background contributions and if each measuring period T_i has the same integrated luminosity, the statistical errors become:

$$\Delta_{stat}A = \sqrt{\frac{1-A^2}{N}}. \quad (2.83)$$

For the generic case the error calculation gets somewhat more elaborate, in particular when also the statistical errors of the estimates for the various background contributions must be taken into account. The selection cuts and background contributions are discussed in section 4.4 and section 4.5, respectively. The neutron counts in equation (2.82) refer to the *real* neutrons:

$$N_i = N_i^n - N_i^{nr} - (1 - \eta_v)(N_i^c - N_i^{cr}) - \frac{\alpha_i}{\alpha_H}(N_H^n - N_H^{nr}), \quad (2.84)$$

where subscripts i and H denote data taken with ${}^3\text{He}$ in polarization state i (measuring period T_i) and with Hydrogen (instead of ${}^3\text{He}$) in the cell, respectively; and

- N^n : all *neutral* events satisfying selection cuts
- N^{nr} : all *neutral random* events satisfying selection cuts
- η_v : veto efficiency
- N^c : all *charged* events satisfying selection cuts

- N^{cr} : all *charged random* events satisfying selection cuts
 α : luminosity measure for "beam on cell wall"
 (number of alphas in the Recoil Detector).

With

$$\frac{\partial A_j}{\partial N_i} = \frac{\sum_{k=1}^4 (M_{ji}^{-1} M_{1k}^{-1} - M_{1i}^{-1} M_{jk}^{-1}) N_k / Q_k}{(\sum_{k=1}^4 M_{1k}^{-1} N_k / Q_k)^2} \quad (2.85)$$

(where j selects 1, A_e , A_0 or A') the full statistical error becomes

$$\Delta A_j = \sqrt{\sum_{i=1}^4 \left(N_i^n + N_i^{nr} + (N_i^c + N_i^{cr})(1 - \eta_v)^2 + (N_H^n + N_H^{nr}) \frac{\alpha_i^2}{\alpha_H^2} \right) \left(\frac{\partial A_j}{\partial N_i} \right)^2}. \quad (2.86)$$

Monte Carlo simulations

For the evaluation of the integrals (2.77) and (2.79) the asymmetries as well as the unpolarized cross sections were calculated, using code from Nagorny and from Golak, on a grid of kinematics. For a fair comparison all theoretical models should be calculated on the *same* grid, see table 2.1, so that granularity of the grid is limited by the most CPU-intensive calculations, which are those based on the Faddeev equations.

In the Faddeev type calculations, the evaluation of the $|U_\mu\rangle$ rescattering state (2.57) does not depend on the specific $3N$ final state but only on the electron kinematics. In terms of CPU time it is the most expensive part of the calculation, hence the number of grid points in θ_e and ω is limited. Each combination of θ_e and ω required 6-8 hours CPU time on a Cray C916. The projection of $|U_\mu\rangle$ onto the $3N$ final states took another 3-4 hours (in total, for all E_m , θ_{nq} and ϕ_{nq}). The code of Nagorny and of PWIA(S) required considerably less computing time and the calculations for the full grid could be performed on a Sun workstation in approximately two months.

In the Monte Carlo simulation the momentum of the electron was generated randomly within the acceptance of the electron spectrometer, with a flat distribution in $\cos\theta_e$, ϕ_e and ω . The azimuthal angle ϕ_e only affects the orientation of the scattering plane. The neutron kinematics were kept on the $(E_m, \theta_{nq}, \phi_{nq})$ grid. The values for the cross section and the asymmetries were then interpolated (in the electron kinematics) from the calculated grid.

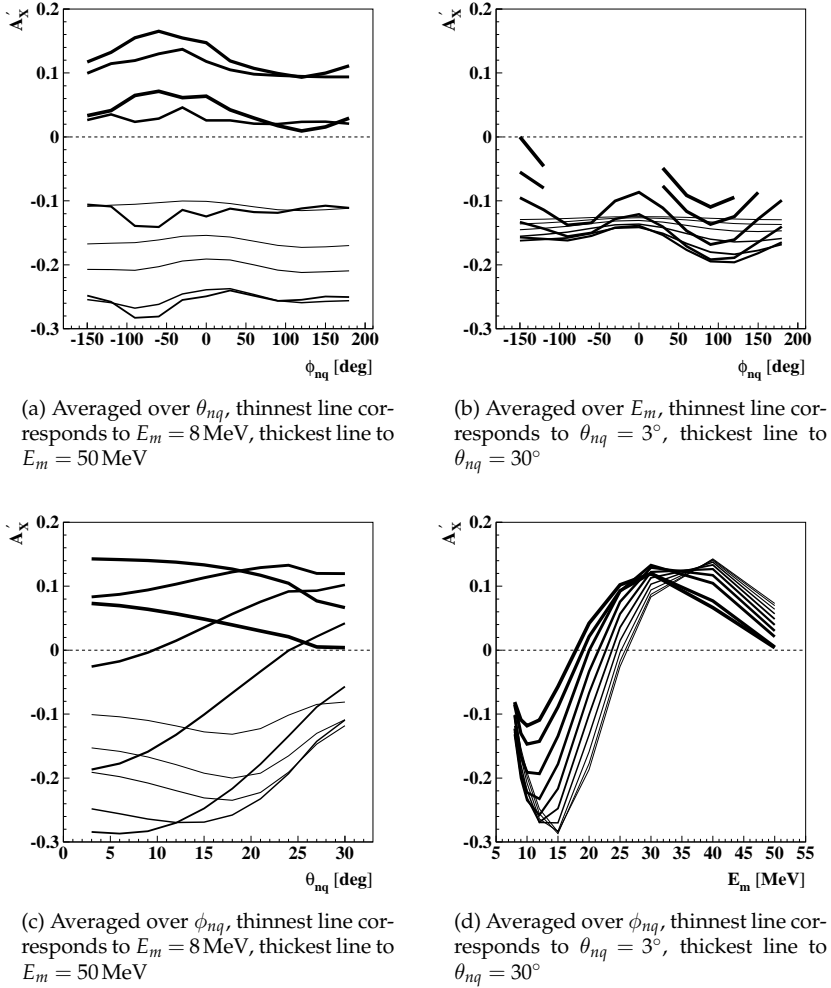


Figure 2.6: Variation of the asymmetry and cross section over the acceptance in the hadronic final state. The asymmetry in the ϕ_e acceptance causes an asymmetry in the curves for ϕ_{nq} .

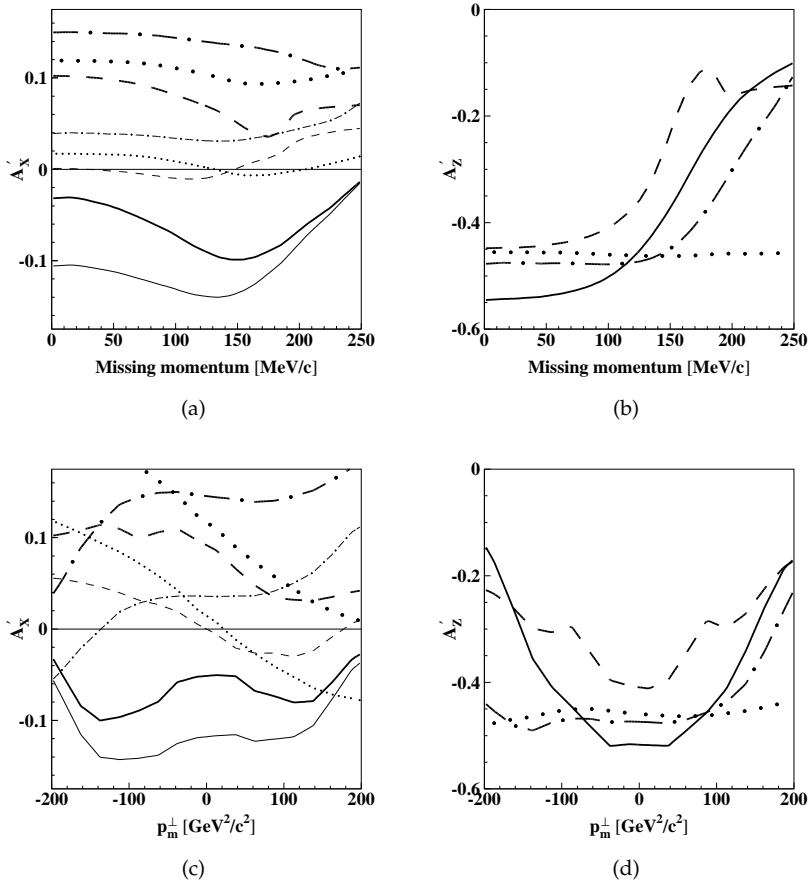


Figure 2.7: Some numerical results of the Monte Carlo simulation [90], using code based on calculations from Golak (solid), Nagorny (dashed) and with PWIA (dash-dotted), PWIAS (dotted). For the thick curves (and longer dashes / dot gaps) calculations were used in which G_E^n was set equal to the Galster parametrization (see section 2.5), for the thin line (and shorter dashes / dot gaps) G_E^n was put to zero.

Variable	Grid values
θ_e [degrees]	35, 40, 45
ω [MeV]	50, 67, 75, 93, 105, 110, 115, 135, 160
E_m [MeV]	8, 9, 10, 12, 15, 20, 25, 30, 40, 50, 60, ..., 100
θ_{nq} [degrees]	0, 3, 6, ..., 39, 42, 45
ϕ_{nq} [degrees]	-150, -120, -90, ..., 120, 150, 180

Table 2.1: Grid of kinematics for which the theoretical models were evaluated, to be used as input for the Monte Carlo simulations. The θ_{nq} angle is the polar angle of p_n with respect to \mathbf{q} in the center-of-mass system; ϕ_{nq} is the corresponding azimuthal angle, with $\phi_{nq} = 0$ corresponding to \mathbf{p}_n lying in the scattering plane. Grid points for which the neutron momenta were outside the acceptance of the Time-of-Flight detector for all ϕ_e (ϕ_e determines the orientation of the scattering plane) were left out.

The calculated values for the observables varied strongly over the (large) acceptance. This is illustrated for the calculations by Golak in figure 2.6. In these calculations $\theta_e = 40^\circ$ and $\omega = 93$ MeV were kept constant and an average was taken over all ϕ_e in the (asymmetric) acceptance of the BigBite electron spectrometer (described in section 3.4.1). Since only the kinematics for which the neutron actually traversed the Time-of-Flight detector were used, in figure 2.6(b) the curves for $\theta_{nq} > 24^\circ$ have interruptions.

Some of the full results are plotted for all calculations for A'_x and A'_z in figure 2.7. The results for A'_x show large disagreement between the different calculations. The Faddeev results show that even for small missing momenta the FSI cause a negative offset. In the results from the calculations of Nagorny the effect of FSI only becomes manifest for $p_m > 100$ MeV/ c where the curve with $G_E^n = 0$ and the curve with nonzero G_E^n start to converge. For $p_m > 150$ MeV/ c the calculations of Nagorny become unstable, because not all relevant partial waves could be taken into account.

2.5 Existing data on G_E^n

The neutron electric form factor has been extracted from the data obtained in an unpolarized inclusive electron scattering experiment on deuterium performed in 1989 in Saclay [40]. From the cross sections measured for different values of the incident electron energy and a range of scattering angles

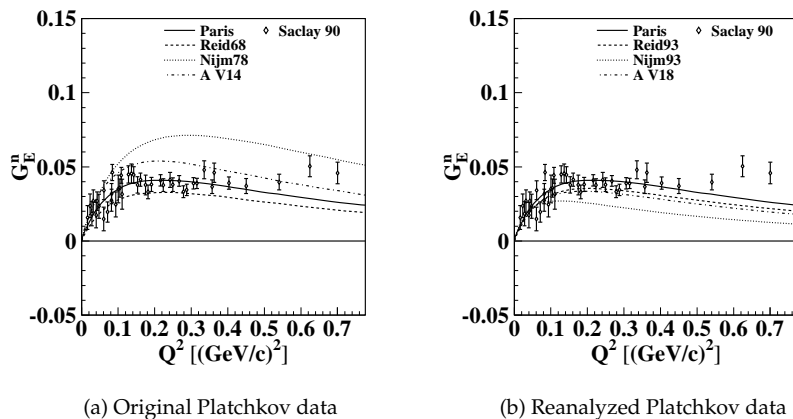


Figure 2.8: The Platchkov data. The data points indicate the values as extracted experimental data by using the deuteron wave function based on the Paris potential. The various curves indicate are parametrizations as in equation (2.87) with a and b fitted to the extracted G_E^d values using various NN-potentials.

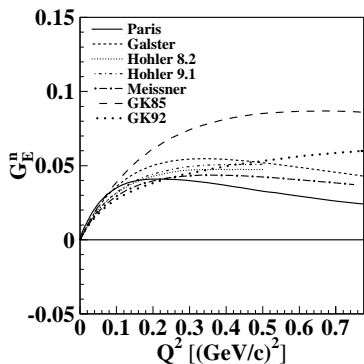


Figure 2.9: Some fits and model predictions for G_E^d . See the text for explanation and references.

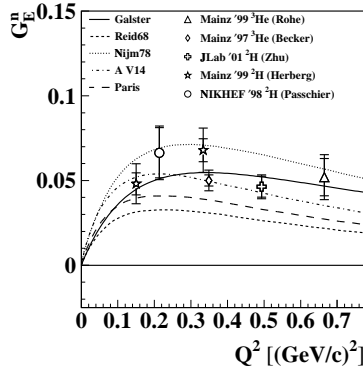


Figure 2.10: The existing G_E^n data from polarized electron scattering experiments. The curves are the same as in figure 2.8(a).

the electric structure function $A(Q^2)$ [21] of the deuteron was obtained for $Q^2 = 0.04 \dots 0.7 \text{ GeV}^2/c^2$ with a precision of 2-6%. By combining this information with the deuteron wave function and the well-known proton electromagnetic form factors, values for the electric and magnetic form factors of the neutron could be deduced.

However, the effect of the small-valued G_E^n on the deuteron structure is rather subtle and its extraction is sensitive to many details of the analysis. In particular it was found that various choices for the NN potential (which determines the deuteron wave function quantitatively) gave quite significantly different results. This is illustrated in figure 2.8(a).

The curves in this figure are fits to the extracted data by using the parametrization of G_E^n by Galster [16] based on earlier data. It has the form

$$G_{E, Galster}^n(Q^2) = \frac{-a\tau G_M^n(Q^2)}{1 + b\tau} \quad (2.87)$$

where for G_M^n usually the "dipole fit" $G_M^n = \mu_n G_D = \mu_n(1 + Q^2/Q_0^2)^{-2}$ is taken, in which $Q_0^2 = 0.71 \text{ GeV}^2/c^2$ and μ_n is the neutron magnetic moment. For the data of ref. [16] the free parameters a and b are equal to 1 and 5.6, respectively. In the present work we will refer to equation (2.87) with these values for a and b as "the Galster parametrization". This parametrization (of the experimental

data from ref. [16]) and the G_E^n extraction of [40] by using the Paris potential are compared to theoretical parametrizations based on Vector Meson Dominance and dispersion relations [30, 17, 82] in figure 2.9.

The slope of $G_E^n(Q^2)$ at $Q^2 = 0$ follows from scattering thermal neutrons off atomic electrons [5, 6, 58]. While theoretical models of the nucleon should reproduce this slope, the slopes (at $Q^2 = 0$) of the fitted curves in figure 2.9 may deviate, since these slopes also depend on the particular choice of parametrization.

From the analysis of Saclay data it was concluded that a reliable, model independent measurement of G_E^n requires a different experimental approach, which seemed to be provided by polarization transfer experiments. Such experiments were carried at *e.g.* Bates (Boston), MAMI (Mainz) [48, 77, 72, 73, 74] and NIKHEF (Amsterdam) [76, 80]; some of the results are shown in figure 2.10, in which the fitted Galster curves of the original Saclay data are also plotted for reference. The $^2\text{H}(\vec{e}, e'n)$ experiments seem to favor *large* values of G_E^n as obtained from the Saclay data by using the Nijmegen potential.

On the other hand, as the NN potentials have evolved due to new input from NN-scattering, the data were reanalyzed in 1999 with the updated versions of those potentials (figure 2.8(b)). The systematic uncertainty due to the choice of NN-potential seems to be significantly reduced and the corresponding Galster fits converge to a relatively *small*-valued G_E^n curve.

One possible explanation for this apparent discrepancy (between the data from polarization transfer experiments and the reanalyzed $^2\text{H}(e, e')$) is suggested by another discrepancy, namely the 8% difference between the Saclay data set and those from an earlier measurement of $A(Q^2)$ performed at MAMI [24] for $\sqrt{Q^2} = 0.04 \dots 0.39$ GeV/c with the same statistical accuracy of 1-2%. The extracted value for G_E^n from the Mainz data is 0.025-0.05 larger than the value extracted from the Saclay data.

It is noted in ref. [100] that if the Mainz data are correct, then some of the existing theories can give a reasonably good account of the full data set on deuteron structure. If the Saclay data are correct, it appears that *no* conventional theory is entirely satisfactory. A new measurement of the $A(Q^2)$ structure function will be performed in Hall A of Jefferson Lab in order to shed new light on this issue.

Chapter 3

Experimental setup

The ${}^3\text{He}(\vec{e}, e'n)$ experiment described in this thesis was performed using the accelerator facilities of NIKHEF (*Nationaal Instituut voor Kernfysica en Hoge-Energie Fysica*), see figure 3.1. From the Polarized Electron Source (PES) pulses of electrons were injected into the Medium Energy Accelerator (MEA). After acceleration to 720 MeV they were stacked in the Amsterdam Pulse Stretcher (AmPS) ring. In the target area (Internal Target Facility, ITF) the beam was steered through an open ended storage cell in which polarized ${}^3\text{He}$ gas was injected. Various detectors were placed around the target cell in order to detect, identify and analyze scattered electrons as well as hadrons emerging from collisions of the electrons in AmPS with the injected ${}^3\text{He}$ atoms. In this chapter we describe the various elements of this setup in more detail.

3.1 The MEA/AmPS accelerator facility

The Medium Energy Accelerator was constructed in the seventies as a 500 MeV linac for electrons. The duty factor was about 1%. In the late eighties the decision was taken to extend the accelerator with the Amsterdam Pulse Stretcher ring (AmPS). In this ring a continuous current could be stacked by injecting with MEA pulses of electrons with a length of one, two or three times the revolution time of the ring ($0.7 \mu\text{s}$).

In stretcher mode a high duty factor ($> 80\%$) beam of up to $12 \mu\text{A}$ was extracted from the ring and projected onto an external target in the Emin experimental hall; the MEA repetition rate was typically 50-150 Hz. With the

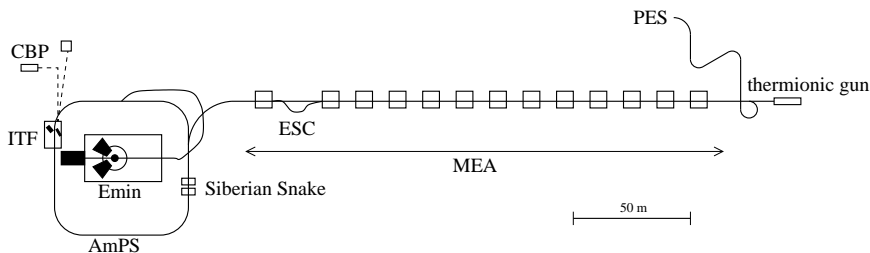


Figure 3.1: Schematic map of the Medium Energy Accelerator and the Amsterdam Pulse Stretcher ring.

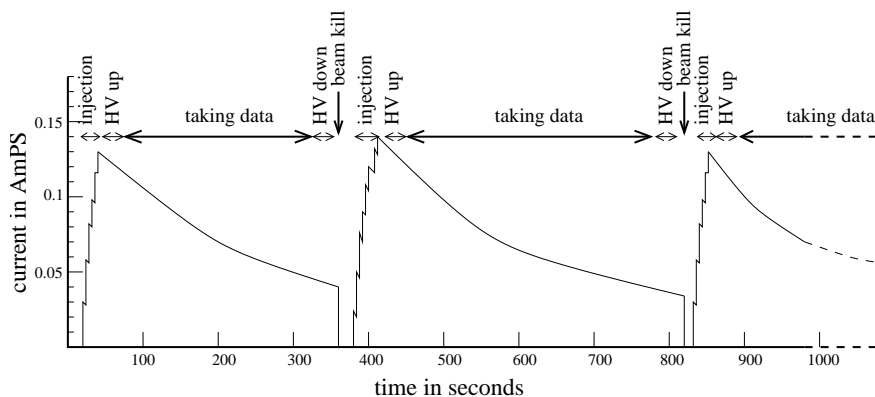


Figure 3.2: Current in AmPS versus time, in storage mode. Some aspects of experimental procedures are added to the graph. One “fill” (removing the old beam, stacking current, ramping up the detectors, taking data and ramping down) takes typically 5-7 minutes. Between fills the target polarization was flipped. After each run (about 10 fills) the electron helicity was flipped. Since the radiation produced during injection might ruin the sensitive components of some of the detectors, their high voltage (HV) had to be ramped down (up) before (after) each injection phase. Discarding (“killing”) the old beam between injections is necessary for polarized electron beams since the polarization has a finite lifetime. It is particularly important between different runs, when the electron helicity is flipped.

high luminosity, which was of the order of $10^{36}\text{cm}^{-2}\text{s}^{-1}$ ($=\text{pb}^{-1}\text{s}^{-1}$), processes with small cross sections like two nucleon knockout reactions could be studied (see, e.g. [83]).

In storage mode several pulses were injected (at 1 Hz) into the AmPS ring. After each injection the beam rapidly damped to an equilibrium trajectory. The amount of stacked current in the ring had roughly the same limitations as in stretcher mode. But in contrast to stretcher mode, where every electron passed only once through the (external) target, the beam was ‘recycled’ with a rate of 1.4 MHz so that although the injection rate was two orders of magnitude lower than in stretcher mode, a four orders of magnitude greater current (up to 250 mA) illuminated the target.

In order to preserve the beam quality, the thickness of the internal target had to be extremely small, less than about 10^{15} atoms per cm^2 . At higher densities the beam blows up to the extent that it is impossible to refocus it and most of the electrons will scatter from the beam pipe and will be lost. Possible internal targets are fibers, pellets [61] and low-pressure gas. In the internal target in the AmPS a carbon fiber target was used for the calibration of the electron spectrometer. For physics experiments gas targets were employed. The gas flow into the scattering chamber was limited to 10^{18} atoms/s by the vacuum requirements of the AmPS ring (10^{-8} mbar) and the speed of the turbo pumps. In order to maximize the luminosity within these limitations, the gas was guided through a cooled tube of 15 or 20 mm in diameter around the beam, which yielded target densities of the order of 10^{14} atoms per cm^2 .

Thus the experiments in the internal target facility (ITF) could be performed with luminosities of the order of $10^{32}\text{cm}^{-2}\text{s}^{-1}$ ($=0.1\text{nb}^{-1}\text{s}^{-1}$). The very low target density enabled the detection of light recoiling nuclei and the background rates were comparatively low.

In order to maintain the polarization of a beam stored in AmPS a set of superconducting solenoids was installed opposite to the location of the internal target. These solenoids compensated the spin precession that occurred in the four bends. The precession angle α after one revolution depends only on the electron energy: $\alpha = 2\pi E/E_{magic}$, where $E_{magic} = 440.65\text{MeV}$. In principle these solenoids (the ‘Siberian Snake’) enabled a polarized electron beam in both storage mode and stretcher mode. However, the polarized electron source was not designed to run at higher rates than 1 Hz and hence could not deliver the amount of current needed for running in stretcher mode. Moreover, in order to get a proper electron spin orientation at the location of the external target, solenoids would be necessary in the extraction line [88]; they

were however never installed.

Figure 3.2 displays the typical time structure of beam current and data taking. The beam current decayed (by interactions with the target, rest gases and the beam pipe and due to synchrotron radiation) with lifetimes of the order of 300 seconds (with target gas) and 1200 seconds (without target gas in the ring).

3.2 Polarized electrons

3.2.1 Polarized electron source

Due to synchrotron radiation a stored electron beam will (in principle) become polarized perpendicularly to the plane of the ring. This is the so-called Sokolov-Ternov effect [14]. The equilibrium polarization of 92% is reached after $15.8 \times \rho^2 L E^{-5}$ seconds, where ρ is the bending radius (in meters) of the beam path in the dipole magnets, L is the circumference of the ring (in meters) and E is the electron energy (in GeV). For AmPS full self-polarization would take more than a day whereas the typical lifetime of the beam with no gas in the internal target is about 20 minutes. Hence, for nuclear physics experiments this polarization mechanism is not useful. However, after stacking of a maximum current of some 250 mA it takes several hours until it has decayed to less than 10 mA. By that time there should have been a significant polarization build-up already. Measurements of this longitudinal self-polarization process have been performed with AmPS and will soon be published [101].

In the absence of a useful self-polarization mechanism a Polarized Electron Source (PES) was developed and constructed at NIKHEF [71]. With circularly polarized laser light electrons of one particular helicity are photo-emitted from a strained layer crystal and steered through a so-called Z-manipulator, which consists of a series of solenoids and electrostatic bends. By tuning the solenoids the spin could be oriented in any direction. During experiments the orientation was tuned such that in AmPS at the location of the internal target the spin was precisely (anti)parallel to the beam direction.

3.2.2 Polarimetry

The degree of polarization directly after the Z-manipulator was measured with a Mott polarimeter, for which the electron spin had to be oriented vertically. For each crystal this was done directly after installation, before removal and a few

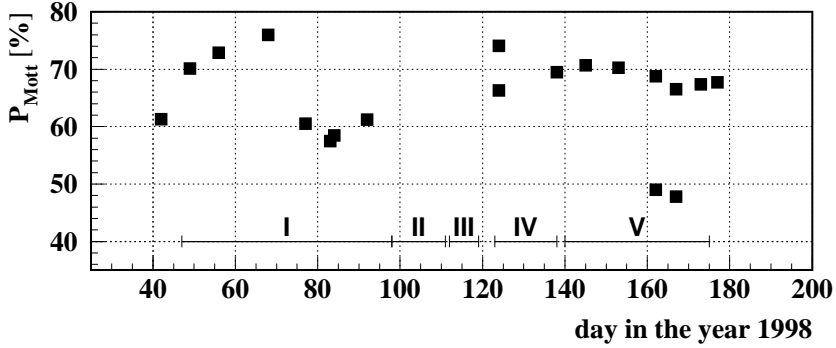


Figure 3.3: *Electron polarization measured with the Mott polarimeter. The horizontal bars indicate the various stages in the experiment: I Commissioning of the polarized electron beam and measurement elastic asymmetry; II Tuning and calibration of the Neutron Detector and the range telescope; III Measurement of A'_x ; IV Measurement of A'_z ; V Measurement of A'_x .*

times in between, typically once every few days. The polarization thus found is plotted versus time in figure 3.3.

The electron polarization was also measured in AmPS with a Compton Backscattering Polarimeter (CBP) [68, 89], see figure 3.4. The stored electron beam was irradiated with circularly polarized laser light in the beginning of the first bend behind the internal target. After Compton scattering the photons had a momentum vector in a narrow cone around the tangent to the electron beam. They were counted in a CsI crystal which was surrounded by a 10 cm thick lead cylinder and preceded by a concrete collimator and a sweeping magnet. By comparing the E_γ spectrum for right oriented with that for left oriented laser light the degree of polarization of the electron beam could be determined.

Ideally, the electron polarization would be monitored continuously, but because of bremsstrahlung and synchrotron radiation backgrounds the CBP measurements could only be performed at small beam currents (< 20 mA) without gas in the target cell. Hence these measurements had to be performed separately. For the determination of the asymmetries in the data analysis the polarization as measured with the Mott polarimeter has been used.

Theoretically, the degree of polarization should not depend on the amount of beam current. However, in our experiments we found strong indications that there is such a dependence. This is discussed in chapter 5.

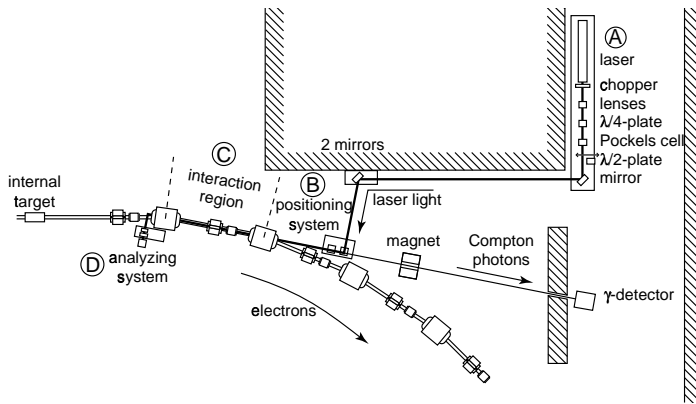


Figure 3.4: The Compton Backscattering Polarimeter in AmPS. The laser light was polarized by means of a quarter-wave plate and a Pockels cell (A). A system of mirrors, all under 45° with respect to the laser beam, guided the beam into the first section of the bend directly after the internal target (C). The intersection of the laser beam with the electron beam was optimized with the beam positioning system (B). The photons that do not undergo Compton scattering were reflected into the analyzing system (D). This system consisted of a power meter preceded by a linear polarizer and a rotating half-wave plate; the ratio of the oscillation amplitude and the offset of the power is equal to the degree of circular polarization of the laser light.

3.3 Polarized ^3He target

A source of polarized ^3He atoms was developed and constructed at the *Vrije Universiteit* [79]. Figure 3.5 shows part of the target setup. In a glass pumping cell mounted directly above the target cell a fraction of the atoms of ^3He gas at low pressure (1 mbar) was excited by an RF discharge to the metastable 2^3S_1 state. The magnetic holding field, generated by a set of Helmholtz coils (not shown in the figure) around the scattering chamber, defined the quantization axis. By irradiating the cell with left (right) circularly polarized laser light parallel to the magnetic field, the atoms with total magnetic quantum number $m_F > 0$ ($m_F < 0$) were excited to $2^3P_{0,1,2}$ states. The atoms decayed back to the 2^3S_1 with either positive or negative m_F . After some time only the states with $m_F < 0$ ($m_F > 0$) were populated. The polarization was transferred from the metastable 2^3S_1 atoms to the ground state (1^1S_0) atoms by so-called metastability exchange collisions; and since in the ground state of a ^3He atom the total angular momentum of the two S-state electrons is zero, the polarization was in that state completely carried by the nucleus. The resulting polarization was measured by monitoring the polarization of the fluorescence light emitted by the $3^1D_2 \rightarrow 2^1P_1$ transition in the RF discharge.

Via a feed tube the 45-50% polarized gas flowed with a rate of 10^{17} atoms per second into the target cell, resulting in a target thickness of 0.7×10^{15} atoms cm^{-2} . In order to achieve this density the target cell was cooled to 17 K.

The direction of the polarization (ϑ^* , φ^*) was defined by the magnetic field generated by the three pairs of Helmholtz coils and, correspondingly, the direction of the laser light. There were three different settings:

- Elastic scattering: $\vartheta_s^* = 98^\circ$, $\varphi_s^* = 0$ ($\vartheta_{lab}^* = 27^\circ$, $\varphi_{lab}^* = 0$), close to the direction of the BigBite spectrometer, which was located at $\vartheta_{lab}^{BB} = 30^\circ$ ($\vartheta_q^{lab} = 71^\circ$). This reaction channel served to check the luminosity and the product of beam and target polarization. The chosen direction of the target polarization maximizes the experimental asymmetry.
- Parallel (measurement of A'_z): $\vartheta_s^* = 0^\circ$ ($\vartheta_{lab}^* = 56^\circ$, $\varphi_{lab}^* = 180^\circ$) with the BigBite spectrometer positioned at an angle of $\vartheta_{lab}^{BB} = 40^\circ$, so in this measurement the target polarization is parallel to the central value of the momentum transfer \mathbf{q} . However, when a field map was made after the data for this set were taken, it turned out that due to a wrong polarity of the DC current power supply of one of the Helmholtz coil pairs the actual direction was $\vartheta_{lab}^* = 28^\circ$, $\varphi_{lab}^* = 180^\circ$ ($\vartheta_s^* = 28^\circ$, $\varphi_s^* = 0^\circ$). So instead of

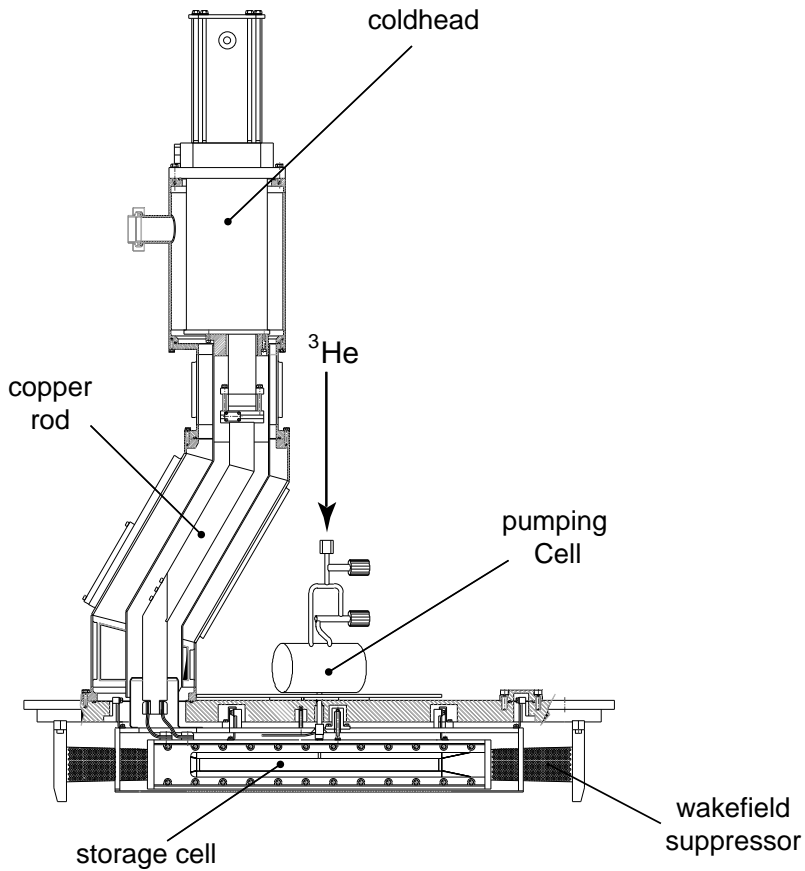


Figure 3.5: Some components of the target setup. By cooling to 17 K the target density increased with a factor of four. Copper braids conduct the heat from the target cell to a $40 \times 40 \text{ mm}^2$ copper bar, connected to a 30 Watt coldhead. The connection is curved in order to allow for the Helmholtz coils (not shown).

A'_z a linear combination $A'_z \cos(28^\circ) - A'_x \sin(28^\circ)$ was measured. In the ${}^3\text{He}(e, e'n)$ channel A'_x is an order of magnitude less than A'_z so that in the neutron channel the effect of this mistake was a reduction of the measured asymmetry by a factor of $\cos(28^\circ) = 0.88$.

- Perpendicular (measurement of A'_x): $\vartheta_s^* = 90^\circ$, $\varphi_s^* = 0^\circ$ ($\vartheta_{lab}^* = 34^\circ$, $\varphi_{lab}^* = 0^\circ$ and still $\vartheta_{lab}^{BB} = 40^\circ$).

Data with $\vartheta_s^* = 90^\circ$, $\varphi_s^* = 90^\circ$ ($\vartheta_{lab}^* = 90^\circ$, $\varphi_{lab}^* = 90^\circ$), comprising a measurement of A_y^0 , were taken in 1997. The analysis of this experiment may be found in [79].

3.4 Detectors

As mentioned above, the ${}^3\vec{\text{He}}(\vec{e}, e'X)$ experiment was performed in three stages: elastic scattering, and measurements of A'_z and A'_x . For the measurement of elastic ${}^3\text{He}(e, e'{}^3\text{He})$ scattering the Recoil detector had to be on the opposite side of BigBite (figure 3.6(a)). For the A'_z and A'_x measurements the Recoil Detector was mounted on the same side as BigBite in order to measure protons and deuterons optimally with the range telescope, (figure 3.6(b)).

3.4.1 The BigBite electron spectrometer

The BigBite electron spectrometer consists of a dipole magnet followed by tracking and particle identification detectors. The whole system is mounted on a platform which can be rotated to angles between 25° and 90° (in steps of 5°) around a pivotal point fixed below the target center via a system of air-pads. In figure 3.7 all basic components are shown in a side view.

A particle emanating from the target enters the spectrometer at 99 cm from the target center through the 25 cm wide mouth of a wedge-shaped dipole magnet¹. The nominal field intensity of 0.92 Tesla deflects a 500 MeV electron entering along the optical axis by 25° .

After deflection in the magnet the electron traverses a pair of multi-wire drift chambers. The chambers are 70 cm apart and have active areas of $140 \times 35 \text{ cm}^2$ and $200 \times 50 \text{ cm}^2$, respectively.

In each wire chamber, the dispersive direction of the track is measured in two wire planes, with a pitch of 20 mm, shifted half a pitch with respect to each

¹Constructed in the Budker Institute for Nuclear Physics, Novosibirsk, Russia

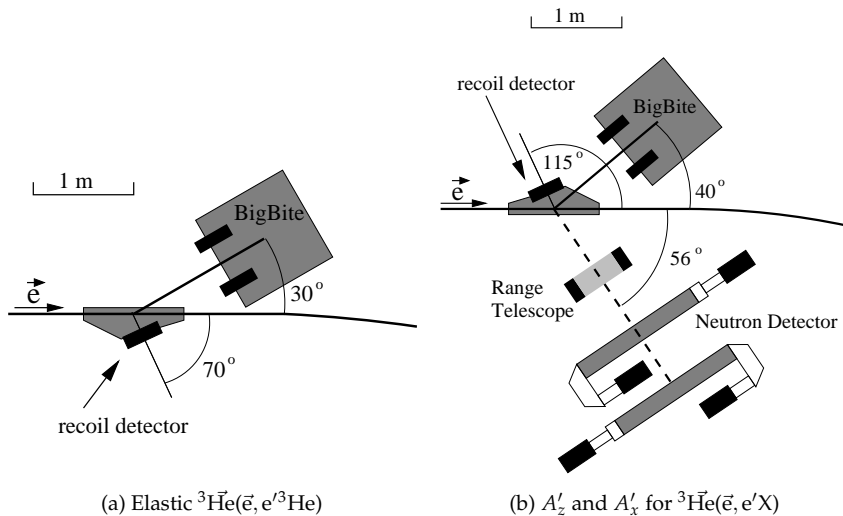


Figure 3.6: Schematic maps of the detector configuration (only roughly on scale).

other. The time difference between the trigger of the scintillator (see below) and the anode wire hit scales with the drift time of the ionization charge to the wire. This drift time, ranging from zero to several hundred ns, constrains the dispersive coordinate to within $180\ \mu\text{m}$, apart from a reflective ambiguity which is removed when at least three (out of four) wire planes fired.

The nondispersive coordinate is measured by copper strips on the outer (cathode) planes of each drift chamber. The strips are $4.08\ \text{mm}$ wide and are laid down on mylar foil with a pitch of $5.08\ \text{mm}$. Comparison of the amount of charge collected by a strip with the charge collected by the neighboring strips constrains the nondispersive coordinate of the track to within $100\ \mu\text{m}$.

The coordinates of the hits in the drift chambers together with the assumption that the particle emanated from the beam line fix the track of the particle in the field of the dipole. The bending radius of this track and the field strength uniquely determine the momentum.

The timing for the drift chambers is set by a $200 \times 50 \times 1\ \text{cm}^3$ scintillator directly after the second chamber. On each side there are two photomultipliers, of which at least one must fire, in order to produce – with a mean timer – a trigger that is (almost) independent of the position in the scintillator. This

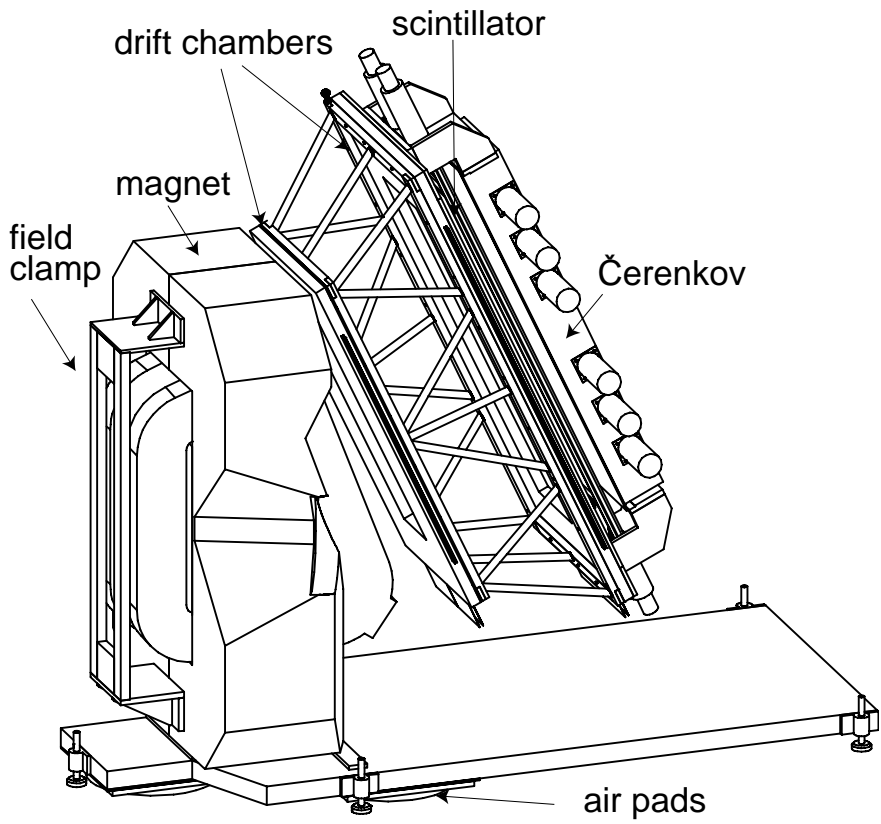


Figure 3.7: Components of the Bigbite electron spectrometer.

Quantity	Acceptance	Resolution
Momentum	250 ... 900 MeV/c	0.84%
θ	± 80 mrad	3-5 mrad
ϕ	± 300 mrad	3-5 mrad
vertex	± 300 mm	3.2 mm
timing		1 ns

Table 3.1: *Acceptance and resolutions (standard deviations) of the BigBite spectrometer.*

trigger also determines the timing of the BigBite arm trigger that is sent to the Coincidence Detector (see figure 3.15).

The top component of the electron spectrometer is a Čerenkov detector consisting of a $210 \times 50 \times 24 \text{ cm}^3$ stack of aerogel blocks, read out via a diffusely reflective light box by twelve 5 inch photomultipliers [67]. The refractive index of aerogel is 1.05 and the material has an small density so that the energy loss by atomic collisions is negligible. Charged particles with a speed greater than $c/1.05 = 0.95c$ (where c denotes the speed of light in vacuum) produce Čerenkov light. Pions with such a speed have a momentum greater than $435 \text{ MeV}/c$. The cross section to produce such fast pions with 720 MeV electrons is negligibly small.

In the environment of the internal target hall only electrons and cosmic muons could produce a detectable signal in the Čerenkov detector. The momentum distribution of the cosmic radiation has its maximum around the zenith. The assumption that these tracks would originate from the beam line therefore results for most of the cosmics in a small bending radius in the dipole and hence a very low momentum (peaking at the minimum of the acceptance, around $250 \text{ MeV}/c$).

Table 3.1 summarizes the acceptance and resolutions of the BigBite spectrometer. For more extensive descriptions of its design, calibration and properties the interested reader is referred to [70, 86, 66, 67].

3.4.2 Recoil detector

In contrast to fixed (liquid, solid) targets, an internal gas target is so thin that low-energy recoiling nuclei can escape from the target and be detected. This enables the measurement of reaction channels that would otherwise be either

impossible or extremely difficult. To exploit this advantage of the internal target, the Recoil Detector was designed and constructed by the *Vrije Universiteit* group within NIKHEF.

The Recoil Detector was contained in a low-pressure (7 mbar) $300 \times 308 \times 150 \text{ mm}^3$ box mounted directly on the scattering chamber, either on the opposite side to the BigBite at 70° or on the same side at 115° . A 99% transparent grid before the entrance of the detector suppressed the electro-magnetic pickup induced by the RF field of the beam.

A recoiling particle from the target (*e.g.* a deuteron) with sufficient energy traversed a $0.9 \mu\text{m}$ mylar foil that separated the detector atmosphere from the AmPS vacuum, a low-pressure wire chamber, two silicon strip detectors (SSD) and a scintillator (see figure 3.8). However, because of a high rate of low-energy electrons from Møller scattering, the wire chamber could only function properly when permanent magnets were mounted on top and below the entrance of the detector to deflect those electrons to smaller angles. Since the gradients of the fringe fields of these magnets would have ruined the target polarization the wire chamber of the Recoil Detector was not used.

Each of the two SSDs had three $50 \times 50 \text{ mm}^2$ segments, divided in 16 strips. On the first (second) layer the 0.1 mm (0.5 mm) thick strips ran vertical (horizontal), giving horizontal (vertical) position information. The distance of the first silicon layer to the target center was 21.4 cm so that with a vertex resolution of 0.5 cm an angular resolution of 2° could be obtained. The light nuclei ($^1,^2,^3\text{H}$, $^3,^4\text{He}$) stopping in the second layer could be clearly identified with the $\Delta E/E$ method. The maximum detectable kinetic energy of a ^3He nucleus in this case was 31 MeV, or 83 MeV if it stopped in the $60 \times 180 \times 5 \text{ mm}^3$ scintillator.

For more extensive descriptions and analyses the reader is referred to [78, 63, 70, 75, 103, 87].

3.4.3 Range telescope

Figure 3.9 shows the layout of the range telescope, which was positioned at 69.0 cm from the target center at an angle of 56° . It consists of two wire chambers and an array of two thin layers of plastic scintillator ($30 \times 50 \times 0.2 \text{ cm}^3$) and fourteen thicker layers ($30 \times 50 \times 1.0 \text{ cm}^3$).

The multi-wire proportional chambers have three wire planes – in the X, Y and Θ ($= 45^\circ$) direction – with a pitch of 6 mm. A 1 mm aluminum plate was placed on the scattering chamber over the exit foil to protect the wire chambers against low energy background.

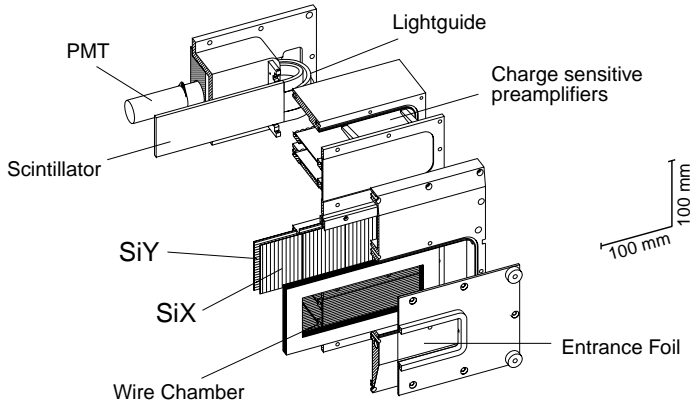


Figure 3.8: Components of the Recoil Detector.

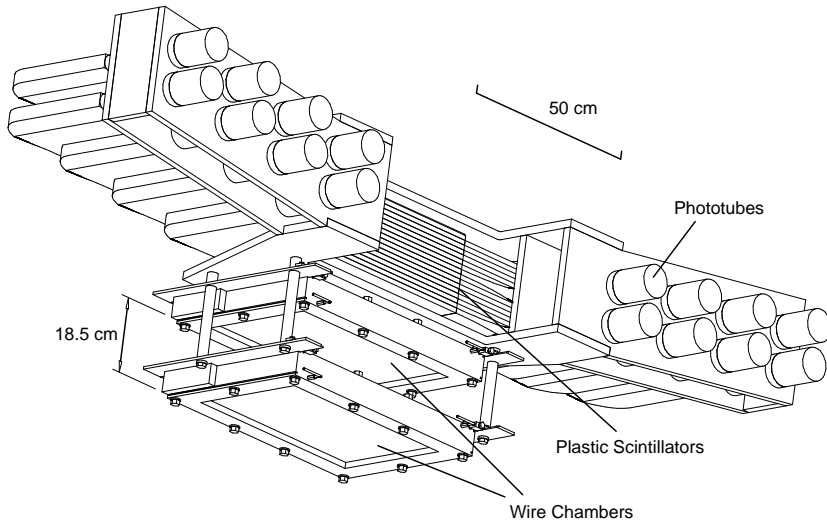


Figure 3.9: Components of the range telescope.

The trigger was defined by the coincidence of hits in the second and the third scintillator layer; in this way the background was reduced but the deuterons of interest (kinetic energy greater than 45 MeV) could still be detected. Deuterons with more than 200 MeV kinetic energy punched through the last scintillator layer. The kinetic energy range for protons was 33-150 MeV. The angular acceptance was $56^\circ \pm 9^\circ$ in the polar angle and $\pm 15^\circ$ in the azimuthal angle.

This detector was used in several earlier experiments at NIKHEF [60, 65] and in Saskatoon [55]. The full analysis of the ${}^3\vec{\text{He}}(\vec{e}, e'p)$ and ${}^3\vec{\text{He}}(\vec{e}, e'd)$ reaction channels may be found in [85].

3.4.4 Neutron detector

Neutron detection and Time-of-Flight

In order to detect a particle it has to interact with the detector material. A charged particle mostly interacts electromagnetically. If it has sufficient energy it leaves an ionization trace in any medium except vacuum. There are several techniques to amplify and detect ionization charges. In suitably chosen media the position of these charges can be reconstructed with resolutions better than a μm , whereas the amount of charge in the trace may be used in the determination of the energy and the identity of the particle.

Neutrons do not have a net electric charge. They do have nontrivial electromagnetic structure, but the electromagnetic form factors are not large enough for a neutron to cause an ionization trace.

Only the properties of the strong interaction are relevant for the design of a detector for medium energy neutrons. But although α_s is (at nuclear scales) two orders of magnitude greater than α_e , the density of scatterers (nuclei instead of electrons) is less and the strong interaction has a comparatively short range. The interaction probability for a 100 MeV neutron in a medium with a density of 1 g/cm^3 is of the order of 1% per cm.

In the collision with a nucleus a random fraction of the kinetic energy of the neutron is transferred to (fragments of) the nucleus with which it interacted (see the subsection on efficiency, page 57). Most of these fragments are charged and hence ionize the detector material (provided their kinetic energy is sufficient).

Therefore, a measurement of the total energy deposited in principle only

yields a lower limit for the kinetic energy of the neutron². If the detector is so large that the neutron and the secondary scattering fragments are, with a high probability, completely stopped, then the deposited and the initial kinetic energy will be strongly correlated. However, for an experiment at intermediate energies with a plastic scintillator detector this would require several meters of thickness. Such a detector is expensive, impractical and would suffer a lot from background radiation.

Instead of by measuring the deposited energy, one may determine in a coincidence experiment the kinetic energy of a nonrelativistic neutron (or any other particle) in an alternative way, namely with the Time-of-Flight technique (TOF). If of one of the other products of the *primary* scattering (in our case the scattered electron) the momentum and the trigger time are accurately known, then the vertex and the instance of the primary interaction can be reconstructed. This information together with the impact position and the trigger time in the TOF detector, determines the distance-of-flight and the time-of-flight and hence the speed of the particle (see figure 3.10).

In order to use a TOF detector for neutron detection it is usually preceded by one or more thin charged particle detectors (“veto layers”); when the TOF detector fires but the veto layers do not, one assumes a neutral particle was detected. This may be either a photon or a neutron. Neutral mesons (usually) do not live long enough to travel the typical distances (several meters) to TOF detectors³. A good timing resolution is required to separate the photons ($\beta = 1$) from the fastest possible neutrons in the experiment ($\beta < 0.8$ in our case). Particles that do not originate from the target location may enter the detector without passing the veto layers. This low energy background radiation may be eliminated by requiring a minimum energy deposit, at the expense of some detection efficiency.

For various reasons scintillator plastic is the natural choice for the detector material, since it has a reasonable density (and hence reasonable interaction probability for neutrons), is transparent and relatively cheap (which allows large detector volumes) and has good timing properties (the primary prerequisite for a TOF detector). In the following a “neutron detector” is understood to be a TOF detector constructed of scintillator blocks equipped with photomultiplier tubes, preceded by thin scintillator layers that may serve as veto layers.

²Except when the scattering was elastic and the scattering angle is also known; then the momentum of the neutron can be exactly reconstructed. This is the principle of the High Acceptance Recoil Polarimeter detector (see refs. [51, 62]).

³The lightest neutral meson which *does* live long enough is the K_L meson; which due to its mass of 598 MeV does not play a role in the present work.

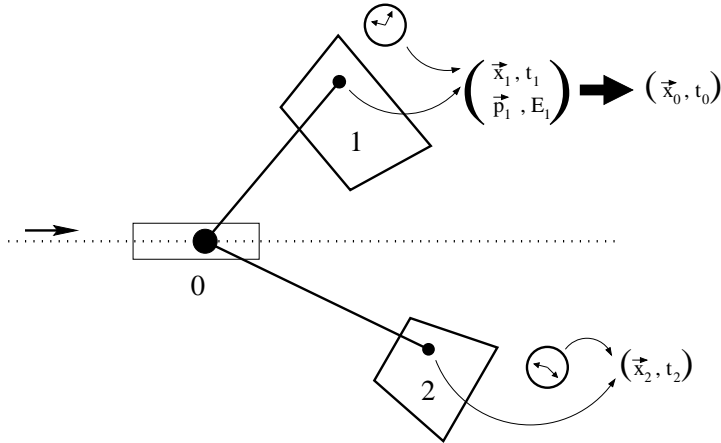


Figure 3.10: In order to measure the velocity of the particle detected at position x_2 at time t_2 the position x_0 and time t_0 of the primary vertex must be calculated from the coordinates and momenta of the particle in detector 2.

On the one hand one would like to construct a neutron detector as thick as possible in order to have a high detection efficiency, given the low interaction probability. On the other hand, the thicker the block the bigger the relative uncertainty in the distance-of-flight and hence the poorer the momentum resolution. The relative uncertainty in the distance-of-flight (and that of the time-of-flight as well) may be reduced by increasing the distance to the target, which, however, decreases the solid angle. Another way to improve the distance resolution is to split the blocks in successive layers (which implies the investment in more complicated electronics and trigger logic).

The TOF detector in ITH

Figure 3.11 shows the geometry of the neutron detector without support structures. The detector consists of two identical walls, each consisting of four telescopes, which consist of three scintillator bars. They were designed and constructed by the *Universiteit Utrecht* as a component of the HARP detector [51], for which they were optimized to detect (recoil) protons.

The bars are 160 cm long, 20 cm wide and 20 cm (E), 1 cm (M) and 0.3 cm

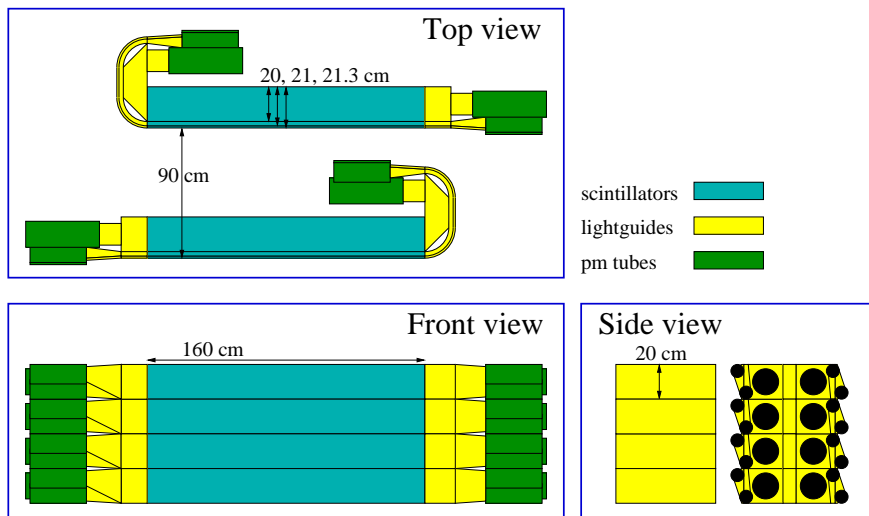


Figure 3.11: Schematic outline of the HARP scintillator bars used as TOF detector in ITH.

(D) thick, respectively. The scintillator material is BC400⁴ (Bicron Corp.). The bars are wrapped in two layers of aluminized mylar (to improve the light collection efficiency) and 0.2 mm thick black PVC (to exclude any light from outside the bar). The E bars are read out on both sides by 5 inch photomultiplier tubes (Burle 8854). On one side they are connected by a simple (cube and cylinder) light guide while at the other end the light is reflected over 180° by a double-prism light guide; this was necessary in the design of the HARP detector. The veto layers (M and D) are read out by 2 inch photomultiplier tubes (Burle 8575), connected to the bars by adiabatic light guides, which on one side make a 180° bend just like for the E bar.

Four telescopes are mounted with plastic straps on a steel support structure, which can move on a rail system inside a support frame. The two scintillator walls in their respective support frames were put together on a steel frame with wheels, such that the center of the array was at beam height and the scintillators faced in the same direction. The detector was positioned in the internal target hall as depicted in figure 3.6.

⁴Equivalent to NE-102A.

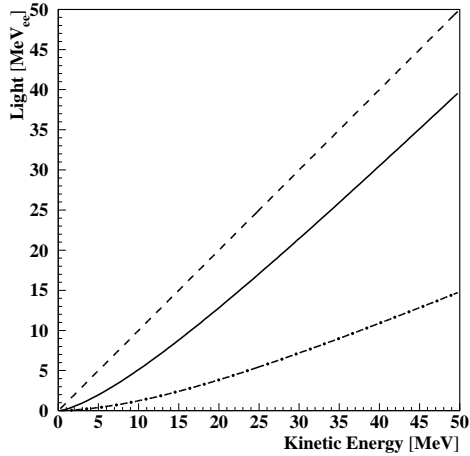


Figure 3.12: Amount of light, expressed in electron equivalent MeV, versus kinetic energy (MeV), for protons (solid), α particles (dash-dotted) and electrons (dashed) stopping in NE-102 scintillating material.

The central angles of the detectors were chosen to match the central angles for quasi-elastic nucleon knockout from a ${}^3\text{He}$ nucleus at $Q^2 = 0.2 \text{ GeV}^2/c^2$ with an incident electron energy of 720 MeV. At this angle, it was positioned as far away from the target as possible. The front face of the first wall was at 2.1 m from the target.

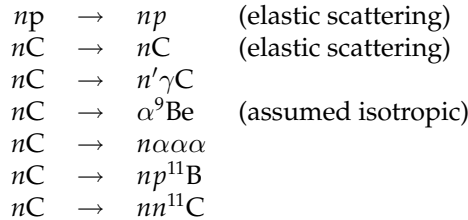
Efficiency

For a good comparison of a theory to measured data, the predictions of the theory must be 'folded' over the acceptance via a Monte Carlo simulation, as described in section 2.4. For asymmetry measurements, the efficiency of the detectors does not affect the result directly, in contrast to the case of absolute cross section measurements. However, the efficiencies are weighting factors in the Monte Carlo simulation and hence their variation (rather than their absolute values) still needs to be known accurately.

The efficiency of a neutron detector may be determined experimentally by irradiation with a well-defined neutron flux, *e.g.* with the neutron beam at the Paul Scherrer Institut (PSI) in Villigen (Switzerland) [35] or with the ${}^1\text{H}(\gamma, \pi^+ n)$

reaction, see [56, 57]. In the latter the measurement of the π^+ momentum vector fixes both the photon energy and the neutron momentum.

Alternatively the efficiency may be estimated by means of a Monte Carlo simulation using cross section tables from neutron-nucleus and np scattering data. The KSUVAX program [20] simulates neutron interactions in detectors through “tracking” and “scattering” with either protons or carbon nuclei with a probability determined from the cross section tables. The program was checked for neutron kinetic energies up to 300 MeV, several scintillator types and detection thresholds and found to be reliable to within 10%. The following processes are taken into account:



Knocked-out α particles and protons, as well as the scattered neutron, are subsequently tracked, until they either leave the detector volume or deposit (almost) all their kinetic energy. The efficiency of the conversion of the deposited energy to visible light is retrieved from a fit to data from light response measurements. The amount of light is expressed in the unit MeV_{ee} , i.e. the amount of light generated when a 1 MeV electron stops in the detector material⁵. The fitting function has the form

$$\mathcal{L}[\text{MeV}_{ee}] = a_1 T_{(p,\alpha)} - a_2 \left[1.0 - \exp(-a_3 T_{(p,\alpha)}^{a_4}) \right] \quad (3.1)$$

where the coefficients a_i depend on the particle (p, α) and on the type of scintillator material, while T_p is the kinetic energy (MeV) of the particle. So by definition for an electron one has $a_1 = 1$ and $a_2 = 0$. In figure 3.12 the graphs of the fit for protons and α particles are shown.

The maximum possible neutron detection efficiency for a given detector geometry is the ratio of the number of neutrons that interact with the active detector material over the total number of neutrons that enter the detector. The interaction probability depends only on the detector material, the length of the

⁵For electrons with a kinetic energy greater than 100 keV the amount of light (the sum of the energy of the photons) is a linear function of the energy deposited by the electron.

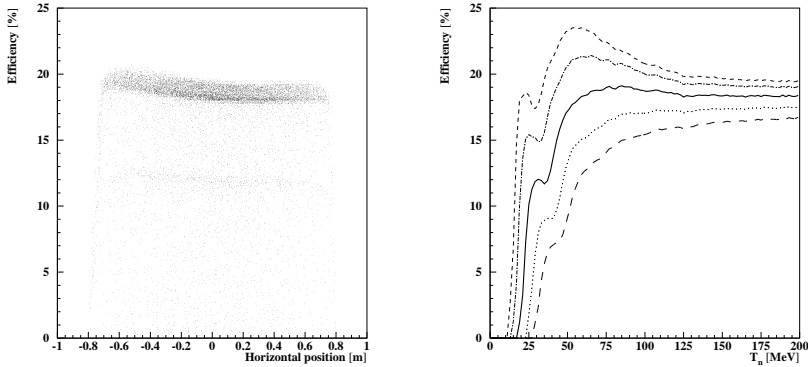


Figure 3.13: Panel (a): Neutron detection efficiency versus position (threshold at 12 MeV_{ee}). Panel (b): Neutron detection efficiency as a function of the neutron kinetic energy for several threshold values of the total amount of light: 6 MeV_{ee} (short dashes), 9 MeV_{ee} (dot-dashes), 12 MeV_{ee} (thick solid line), 16 MeV_{ee} (dots) and 20 MeV_{ee} (long dashes). The attenuation length of the light in the bar travelling towards the phototubes is 3.2 m . The photomultiplier threshold is 5 MeV_{ee} .

neutron track inside the detector volume and the kinetic energy of the neutron. Since the probability distribution fraction of the neutron kinetic energy transferred to the charged scattering fragments has its maximum at zero and decreases steeply, the actual detection efficiency depends strongly on the minimum amount of light that gives a good signal in the photomultipliers.

In the following, a “good signal” is a signal that exceeds the hardware threshold and survives the software cuts. The thresholds of the photomultipliers have been tuned as low as possible but such that the rate of triggers from electronic noise was still negligibly low. As remarked on page 54, low energy random background may be eliminated in the analysis by requiring a minimum amount of scintillator light produced.

In the KSUVAX simulation 10^4 points were generated in a 4-dimensional phase space spanned by the z coordinate of the primary vertex position (triangular distribution), the hit position in the detector (flat distribution for the vertical coordinate, Gaussian-like distribution for the horizontal coordinate with

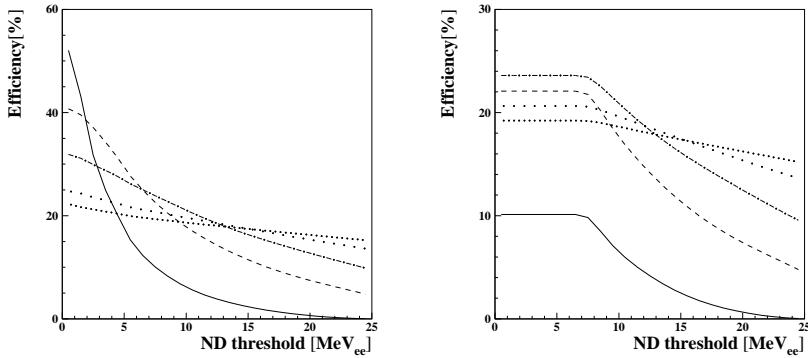


Figure 3.14: Efficiency without (a) and with (b) light attenuation and hardware threshold of 5 MeV_{ee} . Solid: $0 < T_n < 35$; dashed: $35 < T_n < 50$; dot-dashed: $50 < T_n < 75$; dotted: $75 < T_n < 125$; very dotted: $125 < T_n < 200$

a maximum in the center) and the neutron kinetic energy (Gaussian-like). For each point 10^5 neutrons were tracked. The light production was attenuated by a factor $\exp[-d/\lambda]$ where $\lambda = 3.2 \text{ m}$ is the attenuation length and d the distance to the farthest photomultiplier; if the amount of light after attenuation did not exceed the photomultiplier threshold of 5 MeV_{ee} then the light production was set to zero. The statistics of the light production for the complete sample of 10^5 neutrons then provided the efficiency for any detection threshold in that particular point in phase space.

Figure 3.13 displays the dependence of the efficiency of the first wall of the neutron detector on the hit position and on neutron kinetic energy for several thresholds. The slight decrease of the efficiency for more downstream positions (larger values for the horizontal position) is due to the extendedness of the target cell, which makes that for the upstream part of the detector the average length of the track of the neutron through the detector material is greater than that for the downstream part. Figure 3.14 displays the efficiency dependence on the threshold for several T_n bins.

The detection threshold for the time-of-flight detector in the analysis of the ${}^3\text{He}(\vec{e}, e'n)$ experiment was put at 12 MeV_{ee} (see chapter 4). As may be concluded from figure 3.13, the average detection efficiency for one wall is (with

this threshold) equal to $18 \pm 1\%$ for $50 < T_n < 200$ MeV. So within the context of the analysis of this experiment neutron detection efficiency may be taken to be constant. For neutrons emerging from the target into the acceptance of the second wall the detection efficiency is equal to $18\% + (100\% - 18\%) \times 18\% = 33\%$.

3.4.5 Electronics and data acquisition

The electronics of the BigBite spectrometer, the Recoil detector and the range telescope are described in [66, 78, 85], respectively. Figure 3.15 displays the principles of the trigger, readout and data acquisition for the neutron detector. The analog signals of the photomultipliers were carried by 40 m long co-axial cables from the detector to Hadron Digitizer Modules (HDMs) [46] outside the experimental hall.

In an HDM the analog signal is split in three. One of the copies is sent over a delay line to a charge integrator (QDC), the other two are led into a low threshold differential discriminator and a high threshold leading edge discriminator, respectively. If both discriminator thresholds are exceeded, a zero-level trigger is released, where the timing is determined by the low threshold in order to reduce the walk effect. This trigger defines the start time for both the TDC and the integration interval of the QDC of this channel.

In the data acquisition setup for the ITH neutron detector the triggers of the E bar channels were passed to a trigger 1A module, which contains a trigger logic applicable for the Hadron detectors. By not using all input channels this trigger logic simplified to an effective trigger logic as displayed in figure 3.15, so it released a first level trigger when the signals of two photomultipliers of the same E bar had both generated a zeroth order trigger.

A first level trigger defines the stop time for the TDCs in all HDMs and is sent as an arm trigger (ATR) to the Coincidence Detector (CD). The CD collects ATRs from all four detectors and determines whether the ATRs are single hits or part of a double, triple or quadruple coincidence.

Under generic experimental conditions the rates of some types of coincidence, in particular those of the single hits, are too high to be able to store all relevant detector data without introducing an unacceptable amount of dead time. Therefore, for each kind of coincidence (including single hits) a prescaler P_{coinc} may be defined so that the CD generates an Event Trigger (ETR) for only one out of every P_{coinc} instances of that kind of coincidences. The ETR signal is sent to all arms in the coincidence, which in return send all their information for that particular event to the Event Builder (EB) after which the data can be stored on disk and tape.

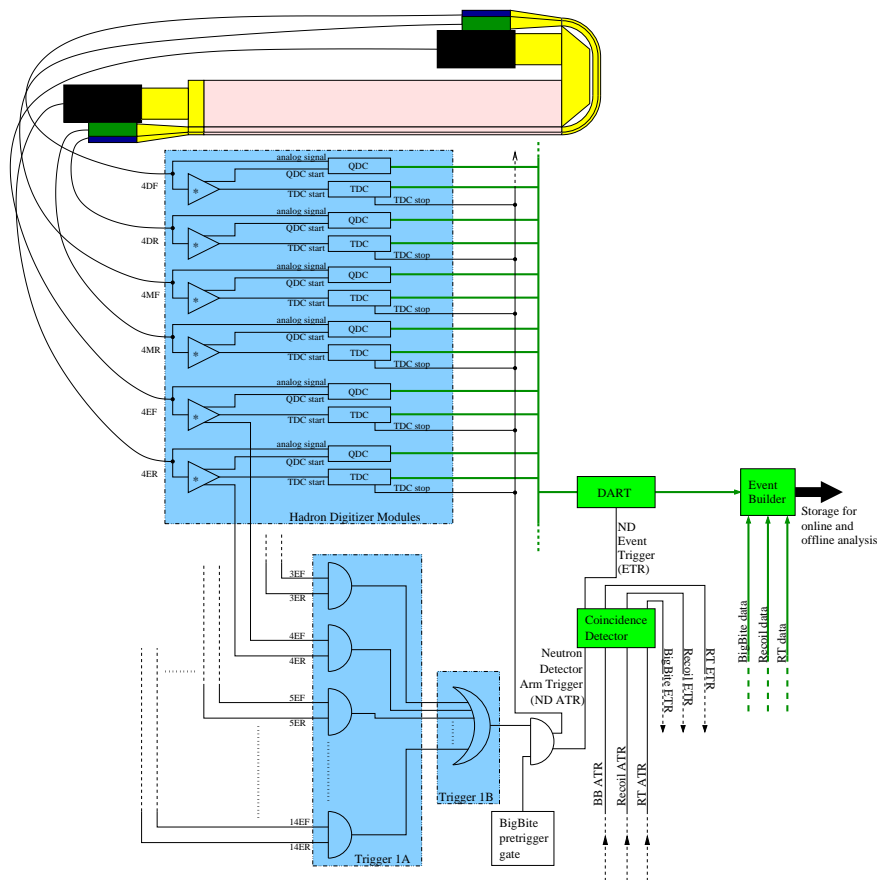


Figure 3.15: *Intuitive representation of ND electronics and data acquisition. The discriminators indicated with an asterisk consist of a low threshold differential discriminator and a high level leading edge discriminator. The depicted trigger logic shows the effective logic obtained by not using all input channels of the trigger 1A module.*

Due to finite acceptances and resolutions there is for all true coincidences (that is, for events where the hits in the various detectors indeed correspond to particles emerging from one and the same scattering event) a finite spread in the times of arrival of the ATRs. The time window for coincidences should be wider than this spread, in order to estimate the amount of random coincidences, resulting in time windows of the order of 100 ns. This puts a constraint on the maximum acceptable individual ATR rates in the CD.

Therefore, the ATR rate of the Neutron Detector was reduced by gating its first level trigger with the pretrigger signal of the BigBite spectrometer. This reduced the ND ATR rate from the order of 100 kHz to below 50 Hz. The BigBite pretrigger signal is defined by the fast signals of its scintillator and the Čerenkov detector. For real coincidences the timing was such that the fastest neutrons arrived 50 ns after the start of the pretrigger gate. The BigBite pretrigger is not equivalent to a BigBite ATR: only 30–40% of the gated Neutron Detector ATRs resulted in an ETR for a BigBite - Neutron Detector coincidence.

Chapter 4

Calibration and Performance

In this chapter the methods used for the calibration of the neutron detector are summarized, and the results presented. Many parameters, such as proportionality constants and offsets, have been determined by using redundant information from well-known and/or overdetermined processes such as cosmic radiation, test pulses and elastic $H(e, e'p)$ scattering. Several parameters could be determined in more than one way, which allowed consistency checks.

4.1 Definitions

4.1.1 Labeling

In this text we label the quantities that are related to photomultipliers and their respective Hadron Digitizer Module (HDM) channels (see section 3.4.5) with three indices $\{tls\}$: the telescope number $t = 1 \dots 8$ (where $t = 1$ and $t = 5$ refer to the top telescope of the first and second wall, respectively), the layer $l = E, M, D$ (see figure 3.11) and the side $s = F, R$. The latter denote "front" and "rear", which originates from the HARP geometry (see refs. [51, 62]), where the photomultipliers on the curved lightguides were closest to the target. In order to minimize the number of labeling conventions for the same device we chose to keep the HARP labels in the application of the scintillator wall as a time-of-flight detector.

Raw data like the digitized values of the integrated charge of the photomultiplier pulses (QDCs) and of their relative timings (TDCs), which are expressed

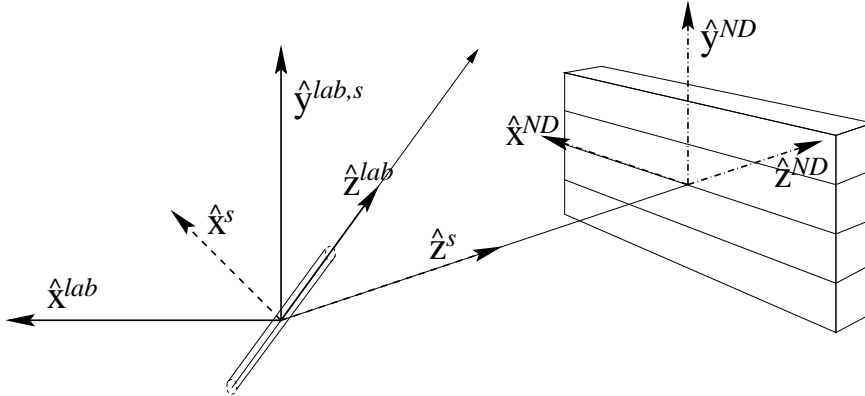


Figure 4.1: The laboratory, spin and neutron detector (ND) frame. Displayed is the ideal situation where the neutron detector would be positioned such that its central axis coincided with the central \hat{q} axis. In the actual situation the detector axis passed the beamline upstream of the target center (see next figure).

in some digitization unit and need to be converted to physics units such as nanoseconds, MeV_{ee} and meters, are indicated in formulae with a tilde (e.g. \tilde{T}).

4.1.2 Coordinate frames

The *laboratory frame* is the frame where \hat{z}^{lab} is along the incoming electron beam, \hat{y}^{lab} is the vertical upwards and $\hat{x}^{\text{lab}} \equiv \hat{y}^{\text{lab}} \times \hat{z}^{\text{lab}}$ is horizontal, perpendicular to the beam on the BigBite side. In the *spin frame* the \hat{z}^s axis is along the central value of the 3-momentum transfer, \hat{y}^s is the vertically upward and \hat{x}^s in the horizontal plane roughly in the direction of the scattered electron. These frames both have the origin in the center of the target. The *neutron detector frame* has its origin in the center of the face pointing to the target and is used for positioning of hits and tracks inside the neutron detector; \hat{y}_{ND} is vertical upward, \hat{z}_{ND} points into the detector and \hat{x}_{ND} points horizontally along the scintillator bar, in the downstream direction.

Ideally, the \hat{z}_{ND} axis would coincide with the \hat{z}^s axis, as suggested by figure 4.1, but in the experimental reality (figure 4.2) it will miss the target center by an amount z_0^{lab} along the beamline and y_0^{lab} vertically. The angle θ_0 between

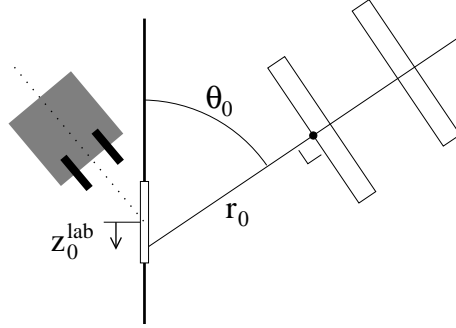


Figure 4.2: The position of the origin of the neutron detector and its orientation are characterized by the parameters $(r_0, y_0^{\text{lab}}, z_0^{\text{lab}}, \theta_0)$. The vertical offset y_0^{lab} is not shown in this figure.

the \hat{z}_{ND} axis and the beam line will be slightly different from the central angle θ_q^{lab} of the momentum transfer. It is assumed that the front face of the detector was perfectly vertical and the bars (the \hat{x}_{ND} axis) were perfectly horizontal. This assumption was crudely checked with a plummet; the horizontal (x and z) deviations of outer edges were less than 1.5 cm.

4.2 Calibration parameters of the neutron detector

In a regular hit the scintillation light propagates towards both the F and R photomultipliers; the timing, position and light production of the hit can be reconstructed from the data of both photomultipliers. In the case of a weak flash which does not exceed both F and R photomultiplier thresholds, or in the case of a HDM triggering on electronic noise, single-sided hits occur, for which the timing, position and light production cannot (or not accurately) be reconstructed. In an M or D layer, such hits can still be relevant for particle identification (see section 4.4), but in E bars they are ignored. In the following a ‘hit’ is assumed to have triggered both photomultipliers of a bar.

4.2.1 Distance-of-Flight

Assuming that the effective speed of light c_l (m/ns) in a particular layer ($l = E, M, D$) is constant, the horizontal (along the bar) position x_{ND}^l ($t = 1 \dots 8$) of a hit

can be retrieved from the TDC information:

$$x_{\text{ND}}^{tl} = \pm \frac{1}{2} c_l \left(d_{t|F} \tilde{T}_{t|F} - d_{t|R} \tilde{T}_{t|R} + t_0^{tl} \right), \quad (4.1)$$

where each $d_{t|s}$ coefficient converts the TDC information (for the HDM channel by which photomultiplier $\{t|s\}$ is read out) to a time in nanoseconds. The offsets t_0^{tl} are chosen such that $x_{\text{ND}}^{tl} = 0$ corresponds to the middle of the bar $\{t|s\}$. The $+$ ($-$) sign holds for telescopes in the first (second) wall, i.e. for $t = 1 \dots 4$ ($t = 5 \dots 8$). The c_l parameters depend on the refractive index n_r of the scintillator material, as well as on the reflectivity of the surface and the wrapping and on the geometry of the layer; one may write $c_l = c/n_r g_l$. The thinner the bar the closer the geometric factor g_l is to 1, since the light which is not emitted in the direction of a photomultiplier is attenuated by more reflections. The c_M and c_D are relevant for charged particle detection (such as protons and deuterons in the ${}^2\text{H}(\vec{e}, e'\chi)$ experiment which was performed directly after the ${}^3\text{He}(\vec{e}, e'\chi)$ experiment described in this thesis, with the same setup except for the Range Telescope, which was taken out). For neutron detection only the position in the E bars needs to be calibrated.

Since within a given telescope no information is available on the vertical position, the vertical coordinate y_{ND} of a hit in the neutron detector is set to the central vertical position of the triggering E bar. If a neighbouring bar also triggered, y_{ND} is set to that of the contact surface (resolution: about 1 cm).

The depth z_{ND} of the hit is the distance from the front face to the location where the incoming particle caused the scintillator light that arrived first at the photomultipliers and determined the trigger. For protons (and other charged particles coming from the target) $z_{\text{ND}} = 0$, but for neutrons z_{ND} can assume any value between $z_{\text{ND}} = 0$ and $z_{\text{ND}} = 20.0$ cm, the thickness of the bar. For z_{ND} in a neutron hit event an average \bar{z}_{ND}^n value is taken. In principle, this value is slightly less than half the thickness of the bar, since a neutron can be detected only once. For an exponentially decreasing flux of neutrons in the bar such that 18% is lost after 20 cm, $\bar{z}_{\text{ND}}^n = 9.7$ cm. Moreover, if the neutron scatters off a proton near the back surface of the bar the proton may escape from the bar and hence not produce sufficient scintillation light to exceed hardware and software thresholds (see section 9). The thickness of this “dead region” is easily estimated to be less than 1 cm, so $\bar{z}_{\text{ND}}^n = 9.5$ cm seems to be reasonable.

For the extraction of kinematic variables, the hit position (\mathbf{x}_{ND}) must be transformed to laboratory coordinates (\mathbf{x}_{lab}) by a rotation over the orientation angle θ_0^{lab} of the ND and a translation over $\mathbf{x}_0^{\text{lab}}$ (the position of the ND frame origin in laboratory coordinates).

4.2.2 Energy deposit and particle identification

For a particle p traversing through (or stopping in) a layer l , the QDC values \tilde{Q}_{tls} are to a good approximation equal to

$$\tilde{Q}_{tls} = \tilde{Q}_{tls}^0 + G_{tls} \mathcal{L}_l(T_p, \vartheta_p, p) \exp\left(-\frac{\frac{1}{2}L \pm x_{\text{ND}}}{\lambda_l}\right),$$

where $\frac{1}{2}L \pm x_{\text{ND}}$ is the distance of the hit position to the photomultiplier $\{tls\}$, $\mathcal{L}_l(T_p, \vartheta_p, p)$ the amount of light produced, λ_l is the attenuation length of scintillator light, the numbers G_{tls} are the product of the lightguide transmission efficiencies and the photomultiplier gains, and \tilde{Q}_{tls}^0 are pedestal values.

The amount of light produced $\mathcal{L}_{tl}(T_p, \vartheta_p, p)$ in a regular hit may be reconstructed from the measured QDC values by eliminating the position dependence:

$$\begin{aligned} \mathcal{L}_{tl}(T_p, \vartheta_p, p) &= \sqrt{\frac{\exp(L/\lambda_l)}{G_{tIF} G_{tIR}} (\tilde{Q}_{tIF} - \tilde{Q}_{tIF}^0)(\tilde{Q}_{tIR} - \tilde{Q}_{tIR}^0)} \\ &= g_{tl} \sqrt{\tilde{Q}'_{tIF} \tilde{Q}'_{tIR}}. \end{aligned} \quad (4.2)$$

The individual gain and transmission factors G_{tls} and the attenuation length do not need to be known separately, but can be absorbed in the g_{tl} constants. The \tilde{Q}'_{tls} are the pedestal subtracted \tilde{Q}_{tls} values.

If in a layer of a telescope next to the triggering telescope also some light was detected and its position agrees with that in the triggering telescope, then it is assumed to be caused by the same particle. Therefore, the amount of light detected in adjacent bars is summed, which requires calibration to the same units (MeV_{ee}). Protons and deuterons may then be identified by the correlation of the summed M (or D) light and the summed E light (the so-called $\Delta E/E$ method).

For the acceptance of an event as a neutral particle hit, all photomultipliers of the M layers of both the triggering telescope and the adjacent telescopes are required to have no signal. From the photomultipliers of the D layers (of the same telescopes) one is allowed to have a signal, because of their higher rate due to low energy background radiation. Some examples are given in figure 4.3. Checking only the veto layers directly in front of the triggering E bar would not be sufficient. For instance an electron might traverse the $2D$ and $2M$ layers and continue its track through the $1E$ bar.

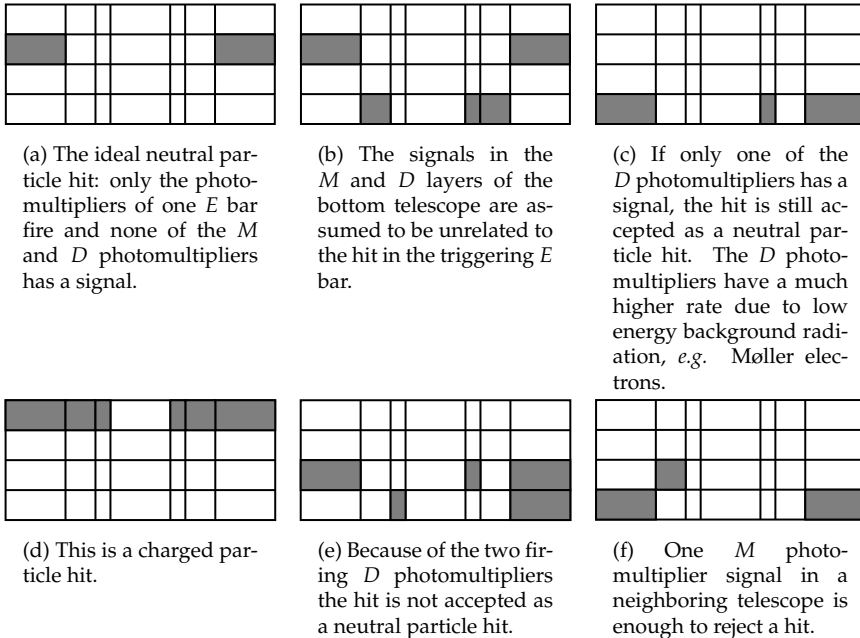


Figure 4.3: Pictograms of example events fulfilling (a-c) or not fulfilling (d-f) the requirements of a neutral particle hit. Each pictogram represents a TOF wall with four telescopes. The outer rectangles represent the photomultipliers on the 20 cm E bars, the squares those of the M layers and the narrow rectangles those of the D layers. Shaded areas represent firing photomultipliers.

The E bars are also subject to a significant rate of low energy background radiation. These events are largely eliminated by applying a software threshold on the total detected amount of light in the triggering E bar and its neighbours, at the expense of some detection efficiency (see page 57 and section 4.4).

4.2.3 Time-of-Flight

As illustrated in figure 3.10, the time-of-flight of a nucleon may be obtained from the difference of the times at which the nucleon and the electron hit their detectors and taking into account the time-of-flight \mathcal{T}_e of the electron. This is an idealisation, since those times can only be measured indirectly via the trigger times. The coincidence detector (section 3.4.5) gives the arrival times $\tilde{t}_{\text{CD}}^{\text{ND}}$ and $\tilde{t}_{\text{CD}}^{\text{BB}}$ of the arm triggers of the detectors, as measured by its fast internal 24-bits clock. The determination of the nucleon time-of-flight \mathcal{T}_n from the time difference $\mathcal{T}_{\text{CD}} = (\tilde{t}_{\text{CD}}^{\text{ND}} - \tilde{t}_{\text{CD}}^{\text{BB}} \pmod{\tilde{t}_{\text{CD}}^{\text{max}}}) d_{\text{CD}}$, where $\tilde{t}_{\text{CD}}^{\text{max}} = 2^{24}$ and $d_{\text{CD}} = 50$ ps, involves a number of corrections:

- The trigger time of the neutron detector corresponds to the time at which a photomultiplier fired, while we need the time at which the neutron actually hit the E bar. The time interval between the hit and the photomultiplier trigger depends on the hit location in the bar, since the light must travel through the bar to the photomultipliers. In the HDM channels of the E bar photomultipliers the delays of the zero level triggers were tuned such that in a regular event the signal of the photomultiplier on the R side of the telescope always arrived later than the F -side signal and hence defined the timing of the ND arm trigger. Hence the correction term is equal to the distance from the hit position to the R photomultiplier divided by the speed of light in the scintillator material.
- An offset \mathcal{T}_0^t (one for every telescope t) to account for photomultiplier response times, cable lengths, trigger delays, etcetera.
- The trigger time must be corrected for walk effects. In principle, “walk” refers to a dependence of the time at which a discriminator (in an HDM, in our case) fires on the amplitude of the incoming photomultiplier pulse. Hence it should, in principle, be studied using the raw QDC values. Since the photomultipliers on the R side are delayed and hence determine the trigger timing, only the ‘ ER ’ QDC values should be relevant. However, since the high voltages were tuned such that differences in photomultiplier gains were minimized and since there is little attenuation in the E

bars, we may approximate the walk effect as a dependence of the trigger time on the amount of scintillation light \mathcal{L} in the triggering E bar. The dependence may be fitted with an exponential

$$\Delta\mathcal{T}_{walk} = Ae^{-B\mathcal{L}}, \quad (4.3)$$

plus an offset which is absorbed in the overall offsets \mathcal{T}_0^t . The walk effect can be satisfactorily studied for the two outer telescopes of the first wall (section 4.3.3), which is then extrapolated to the other telescopes via the above equation (4.3).

Taking this together, we have:

$$\mathcal{T}_n = \mathcal{T}_{CD} + \mathcal{T}_e + \frac{1}{2} \left(d_{iEF} \tilde{T}_{iEF} - d_{iER} \tilde{T}_{iER} + t_0^t \right) + \mathcal{T}_0^t - Ae^{-B\mathcal{L}}. \quad (4.4)$$

The ND hit location, the vertex and time-of-flight together yield the velocity vector. If, by using the signals from the M and D layers, the particle can be properly identified as a neutron, then its 3-momentum is

$$\mathbf{p}_n^{\text{lab}} = \gamma\beta_n m_n c \quad (4.5)$$

with

$$\gamma = \sqrt{\frac{1}{1 - \beta_n^2}} \quad (4.6)$$

$$\beta_n = (\mathbf{x}_n^{\text{lab}} - \mathbf{x}_{\text{vertex}}^{\text{lab}}) / c\mathcal{T} \quad (4.7)$$

$$\mathcal{T} = \text{time-of-flight}. \quad (4.8)$$

Using the BigBite information the derived kinematic variables may then be calculated from:

$$E_m = \omega - T_n - T_{A-1} \quad (4.9)$$

$$\mathbf{p}_m = \mathbf{q} - \mathbf{p}_n^{\text{lab}} \quad (4.10)$$

$$\mathbf{p}_m^{\parallel} = \mathbf{q} \cdot \mathbf{p}_m \quad (4.11)$$

$$\mathbf{p}_m^{\text{oop}} = \mathbf{p}_m \cdot \widehat{\mathbf{k}_e \times \mathbf{k}'_e} \quad (4.12)$$

$$\mathbf{p}_m^{\perp} = \mathbf{p}_m - \mathbf{p}_m^{\parallel} - \mathbf{p}_m^{\text{oop}} \quad (4.13)$$

The calibration parameters that are needed in this procedure and which are described in this section, are listed in table 4.1.

Parameter	Symbol	Number	Method
Conversion factors TDC to ns	d_{tls}	48	T, C
Offsets for positions	t_0^{tl}	24	H, C
Coincidence time offsets	\mathcal{T}_0^t	8	H, He
ND origin and orientation	$r_0, \theta_0, y_0^{\text{lab}}, z_0^{\text{lab}}$	4	H
Walk correction parameters	A, B	2	H
Conversion factors QDC to MeV _{ee}	g_{tl}	24	H, C
QDC pedestals	\tilde{Q}_0^{tls}	48	T
Total		158	

Table 4.1: Calibration parameters of the neutron detector. The next-to-last column lists the number of parameters. The last column indicates how the parameters were calibrated: by means of test pulses (T), cosmics (C), elastic H(e, e'p) scattering (H) and/or ${}^3\text{He}(e, e'n)$ scattering (He).

4.3 Parameter determination

4.3.1 Test pulses

In a test pulse event all HDM channels give a zero level trigger. The line from the gated Trigger 1B back to the HDMs (see figure 3.15) is in the actual setup (partly) a simple cable. Replacing this cable by cables of different lengths changes all TDC values by the same amount of nanoseconds. In this way the linearity of the TDCs may be tested. The d_{tls} parameters have been determined; the average d_{tls} value is 0.228 ns and the maximum deviation is 5.2%.

Since there is no real signal on the inputs of the HDMs, the QDCs are equal to the integrated bias current, allowing to determine the pedestals \tilde{Q}_0^{tls} .

4.3.2 Cosmics

Cosmic rays can be detected by the ND in single arm mode. Rays that traverse all four E bars of one of the ND walls may be used to align the position offsets t_0^{tl} , by fitting a straight line through the four hit positions. Events in which the cosmic particle entered (left) the upper (lower) telescope through one of the side surfaces instead of through the top (bottom) surface are cut out by requiring a minimum value for the QDC's.

For every good cosmic event a line $x = ay + b$ may be fitted through the

four points $(x_t^{\text{ND}}, y_t^{\text{ND}})$ ($t = 1 \dots 4$ or $t = 5 \dots 8$), taking -0.3 m, -0.1 m, 0.1 m, 0.3 m for y_t^{ND} , respectively. The x_t^{ND} coordinates, see equation (4.1)¹, depend on the effective speed c_E of light in the E bars and on the offsets t_{tE}^0 . These are constrained by requiring that:

- The distribution of the direction tangents $a = \tan \theta_{\text{cos}}$ is centered around zenith ($a = 0$) (figure 4.4(a)).
- The distribution of the overall offset b is centered around $b = 0$ (figure 4.4(b)).
- The width of the overall offset distribution is 160 cm. Near the edges of the bars a quadruple coincidence can only take place for near-vertical tracks. This gives the position spectra their characteristic trapezoidal shape; the position resolution is much better than the width of the flanks. Hence the base width of a position spectrum with cosmics, with the requirement that all four telescopes in a wall were hit, should correspond to the length of the scintillator bar.

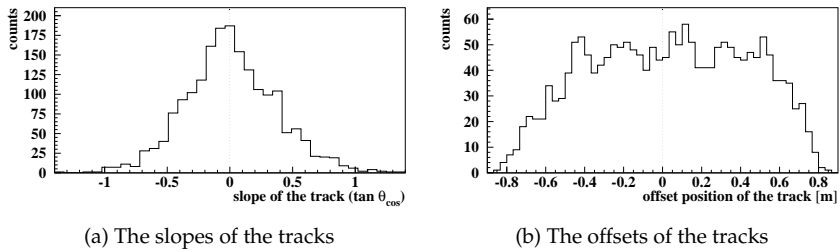
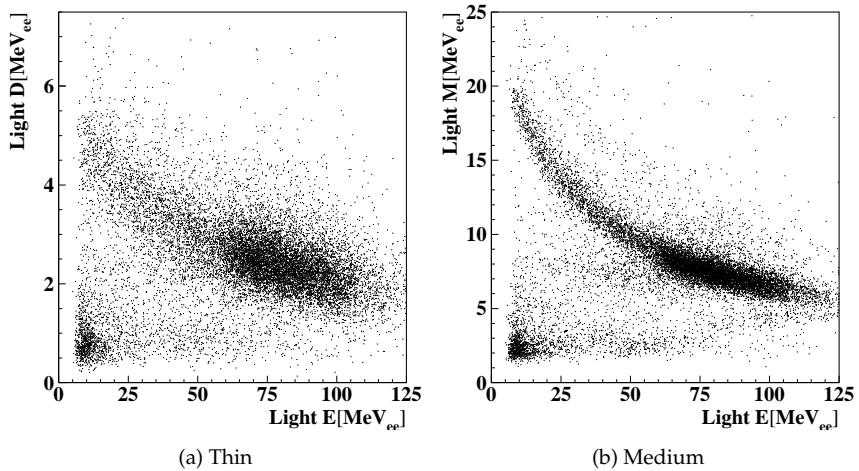
The deviation of the measured positions in the individual telescopes from the fitted line should be position independent and on average equal to zero. This requirement was used to fine-tune the d_{tlS} conversion factors that were obtained from the test pulse measurements.

Once the gain factors g_{tl} for the first wall have been fixed (using elastic H(e, e'p) scattering, see next section), those for the telescopes in second wall are determined by requiring that for cosmics the spectrum of the amount of light \mathcal{L} in a layer l in telescope t ($t = 5 \dots 8$) has its maximum at the same \mathcal{L} value as in telescope $t - 4$.

4.3.3 Elastic H(e, e'p)scattering

Some data were taken with hydrogen in the target cell and the range telescope not yet in its position so that scattered protons could reach the neutron detector.

¹Strictly speaking, the x_{ND} coordinates are slightly ill-defined for slanted tracks with an angle θ_{cos} with respect to the vertical greater than θ_{crit} with $\sin(\theta_{\text{crit}}) = c_E/c$. For these tracks the timings of the F and R photomultipliers are determined by different parts of the tracks through the bar, hence equation (4.1) will yield a position corresponding to somewhere between the endpoints of the track (within the bar) whereas for tracks with $\theta_{\text{cos}} \leq \theta_{\text{crit}}$ the calculated position corresponds to the beginning of the track (within the bar). This slightly deforms the position spectra for cosmics to the extent that the middle of the bar will exhibit a shallow local minimum. Since the effect is quantitatively the same in all bars it does not affect the slope of the fitted tracks.

Figure 4.4: *Cosmics tracking parameter distributions*Figure 4.5: $\Delta E/E$ plots for the center two telescopes of the first wall with $H(e, e'p)$ elastic scattering data.

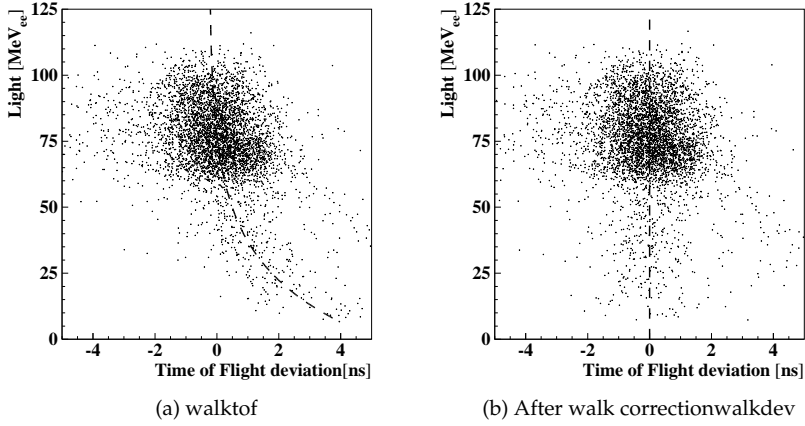


Figure 4.6: The detected amount of scintillator light in the E bars versus the deviation of the measured proton time-of-flight from the proton time-of-flight deduced from electron kinematics, requiring elastic scattering ($|x_{bj} - 1| < 0.1$).

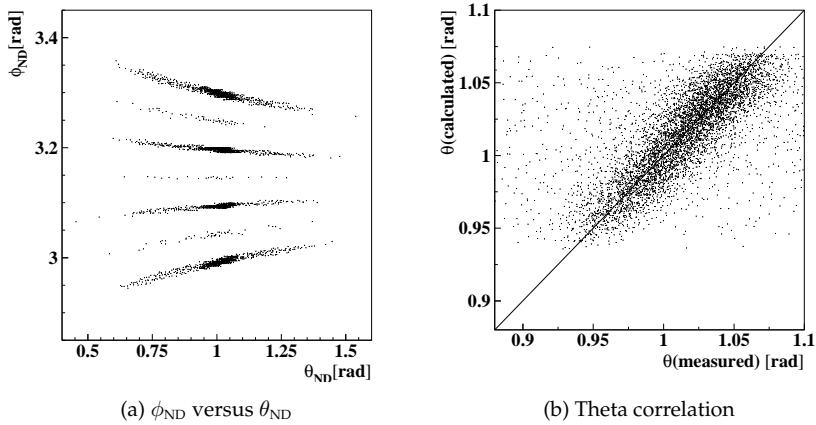


Figure 4.7: Angular ranges in the neutron detector (figure (a)) and calibration of the polar angle (figure (b)).

For those events with a 4-momentum transfer consistent with elastic scattering ($x_{\text{bj}} = Q^2/2M_p\omega = 1$) the time of flight, the angle and energy deposit of the proton in the neutron detector can be predicted. The straggling, energy loss and the time of flight of the proton on its way from the interaction vertex to the neutron detector were estimated with the program *plop* [49], which has been extensively used at NIKHEF for the integration of the Bethe-Bloch equation for electrons and hadrons through various media.

The parameters that are labeled with an 'H' in the "Method" column of table 4.1 were adjusted such that the proton kinematics calculated from the hit position and time-of-flight coincided with those calculated from the electron kinematics.

The tuning procedure consists of the following stages:

1. Energy deposition: equation (3.1) gives the amount of light (in MeV_{ee}) that corresponds to the calculated proton kinetic energy. Comparing this to the measured amount of scintillator light through equation (4.2) fixes all g_{ls} parameters. After calibration the $\Delta E/E$ plots look like in figure 4.5.
2. With a simple meter stick the orientation and the position of the origin of the neutron detector were measured with respect to the wall of the experimental hall, which had an anchor point that corresponded to the position (along the beam line) of the center of the target. The time-of-flight offsets \mathcal{T}_0^t for the first wall ($t = 1 \dots 4$) are chosen such that the measured time-of-flight for protons on average coincides with that calculated with the *plop* program for a proton which has a momentum equal to the momentum transfer \mathbf{q} (as obtained with the BigBite spectrometer) at the elastic scattering vertex.
3. The walk effect may now be studied in the top and bottom telescopes. Events with a minimum amount of light generated in the M and D bars may be identified as proton hits. Some of the protons hitting the top (bottom) E bar may leave the bar through the top (bottom) side. Comparing such events to events where protons of the same kinetic energy are completely stopped, we expect that only a fraction of the amount of scintillation light is produced, whereas the measured time-of-flight should be the same. Figure 4.6 shows scintillator light output versus time-of-flight in telescopes 1 and 4. The band of stopped elastic protons and the band of protons which left the bar are clearly discernible. The latter should, ideally, be a vertical band, but instead deviates to higher times-of-flight for smaller amount of light. The deviating band is fitted with equation (4.3)

and the parameters thus found are used for the walk correction of proton and neutron hits in all telescopes.

4. In order to refine the position information the parameters concerning the ND origin and orientation were slightly adjusted after a comparison of the scattering angle and the azimuthal angle as measured by the neutron detector with those of \mathbf{q} , obtained from the electron kinematics. This yielded $r_0 = 2.38$ m and $z_0^{\text{lab}} = 0.33$ m while $\theta_0 = 56^\circ$ and $y_0^{\text{lab}} = -4$ cm remained fixed. The correlation plots of θ and ϕ are shown in figures 4.7.
5. Now that the positioning has been calibrated, the tuning of the time-of-flight offsets \mathcal{T}_0^t for the first wall $t = 1 \dots 4$ is redone with the same method as above. The gaussian distribution of the difference of the measured and the calculated times-of-flight has a standard deviation of 1.0 ns (FWHM = 2.3 ns). The main contribution to this width comes from the timing resolution of the BigBite scintillator.
6. For the second wall ($t = 5 \dots 8$) the offsets \mathcal{T}_0^t were fixed by requiring the peak of the missing energy distribution for ${}^3\text{He}(e, e'n)$ to be at $E_m = 10$ MeV, a condition which was also satisfied by the telescopes of the first wall and which should be expected from spectral functions obtained with Faddeev calculations [27, 22] and to some extent from ${}^3\text{He}(e, e'p)$ experimental data [25].

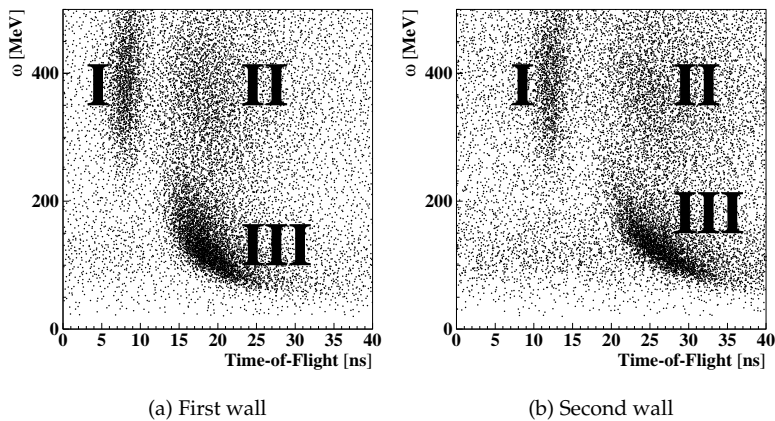


Figure 4.8: Three types of events: ${}^3\text{He}(e, e'\pi/\gamma)$ (region I), ${}^3\text{He}(e, e'n)NN\pi/\gamma$ (region II) and quasi-elastic ${}^3\text{He}(e, e'n)$ (region III).

4.4 Selection of quasi-free ${}^3\text{He}(e, e'n)$ events

We consider only events for which an electron track could be reconstructed in the BigBite spectrometer, with a vertex in the target cell and an energy within a physically acceptable range ($250 < E' < 720 \text{ MeV}$). The term *neutral hit* will be used as shorthand for events in which most probably a neutral particle hit the TOF detector, as was described in section 4.2.2 and illustrated in figure 4.3.

Figure 4.8 shows scatterplots of the energy transfer ω versus time-of-flight for each wall, for all neutral hits in the A'_x data set with a positive reconstructed time-of-flight. There is a clear separation between the events in region I, in which photons (e.g. from π^0 production) were detected, and those of region II+III with slower particles, presumably neutrons from ${}^3\text{He}(e, e'n)$. Region III corresponds to quasi-elastic ($e, e'n$) kinematics, whereas in region II, an additional pion seems to have been created (which might indicate Δ -excitation).

We require that $0.2 \leq \beta \leq 0.8$ (effectively cutting out region I) and assume that we detected a neutron (with $19 \leq T_n \leq 626 \text{ MeV}$). In figure 4.9(a) the energy transfer versus the neutron kinetic energy is shown (for both walls together) for these events. To select only the quasi-elastic scattering events, we restrict the missing energy and momentum to $-50 \text{ MeV} \leq E_m \leq 120 \text{ MeV}$ and $0 \leq p_m \leq 250 \text{ MeV}/c$.

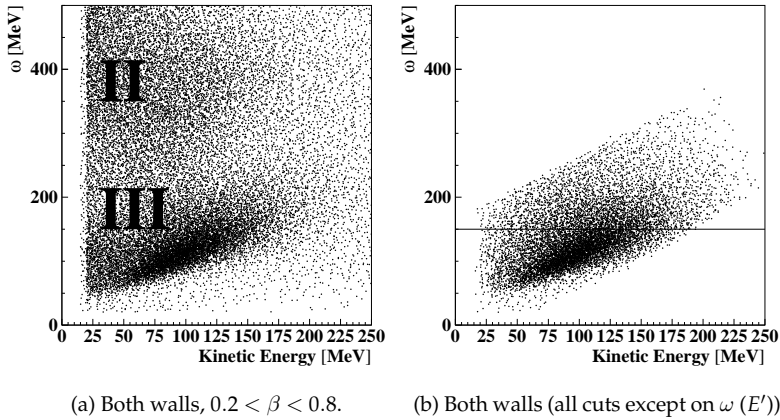


Figure 4.9: The selection cuts on β , p_m and E_m eliminate all pion production events. The upper bound on ω (the line in figure (b)) is in principle superfluous, except that the theoretical descriptions that we would like to compare the data to are considerably less reliable for higher ω .

The cut on E_m is very wide compared to the spectral function of a neutron in ${}^3\text{He}$ (as obtained from Faddeev calculations [22, 27] and from ${}^3\text{He}(e, e'p)$ data [25]) which is sharply peaked around $E_m = 10\text{MeV}$. However, we have a rather modest resolution in E_m (see figure 4.10(e)), and moreover, $E_m \gg 140\text{MeV}$ for events in which a pion was produced. In figure 4.9(b) we show that these cuts effectively selects quasi-elastic nucleon knockout events.

Unfortunately, due to limitations in CPU time the Monte Carlo simulation was only performed for a limited kinematic region, in particular the energy transfer ω had an upper bound of 150 MeV. This bound was partly motivated by the difficulty the theoretical model of Golak seems to have to accurately describe scattering data with larger energy transfer, e.g. those of $\text{He}(e, e'pp)n$ [83]. In the analysis of the A_y^0 data of the 1997 version of the ${}^3\text{He}(\vec{e}, e'X)$ experiment there was no significant ω dependence of the (dis-)agreement between the model and the data, though.

For proper comparison of data and Monte Carlo simulation we should apply the same kinematic cuts. The $\omega < 150$ requirement cuts out 32% of the data.

To summarize, the selection cuts for neutron candidate events are:

$$\begin{array}{rcl}
 0.2 & \leq & \beta \leq 0.8 \quad (19 < T_n < 626 \text{ MeV}) \\
 -50 \text{ MeV} & \leq & E_m \leq 120 \text{ MeV} \\
 0 & \leq & p_m \leq 250 \text{ MeV}/c \\
 20 \text{ MeV} & \leq & \omega \leq 150 \text{ MeV}
 \end{array} \tag{4.14}$$

4.5 Background considerations

The events that are not due to ${}^3\text{He}(e, e'X)$ but nevertheless survive all selection cuts may be subdivided in *random* background (in which the detected particles did not result from the same scattering process in the target region and are also not otherwise causally related) and *coincident* background (*i.e.* events in which the electron detected in the BigBite spectrometer and the particle in the time-of-flight detector *did* emerge from the same interaction vertex).

When not taken into account, background events have two effects:

- Dilution of the measured asymmetries: contributions which are independent from beam and target polarization *and* whose rate² does not depend on the luminosity cancel (to first order) in the numerator but add up in the denominator.
- Introduce of false asymmetries: polarization and/or luminosity dependent contributions.

By switching polarization states very frequently and thus taking the data for all states in very similar beam conditions, the false asymmetries due to contributions that depend on the beam conditions may be minimized. Any remaining background asymmetry may be eliminated if the background contributions can be estimated for every polarization state separately.

4.5.1 Random background

Since the random background events are due to uncorrelated single hits in the detectors, the distribution of the time intervals between the triggers of the two detectors (the coincidence time \mathcal{T}_{CD}) should be flat on time scales smaller than that of the fastest counting detector. In double coincidence experiments where

²Rate: number of events divided by collected charge and target density.

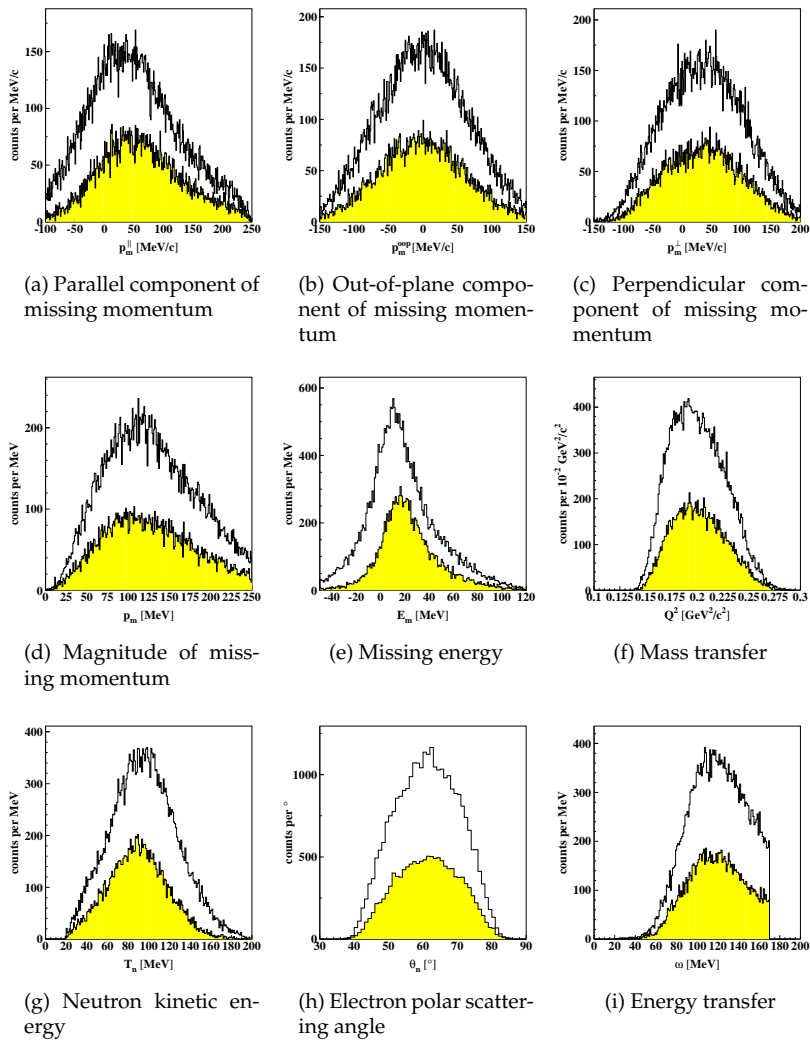


Figure 4.10: Kinematic ranges for neutron candidate events. Shaded: A'_z data set. Not shaded: A'_x data set.

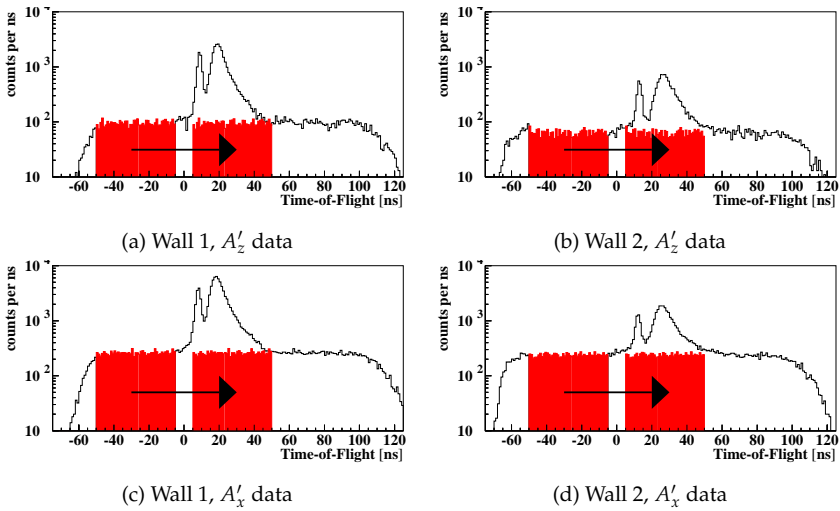


Figure 4.11: Time-of-flight spectra of neutral hits (without cuts). The events in the shaded region with negative time-of-flight are shifted to the physically acceptable domain and analyzed in the same way as normal events. These tagged randoms serve to estimate the number of random background events that survive the kinematic cuts. The random background rate is significantly higher in the A'_x data than in the A'_z data, due to worse beam tuning.

	Wall 1		Wall 2	
	$\mathcal{L} > 5 \text{ MeV}_{ee}$	$\mathcal{L} > 12 \text{ MeV}_{ee}$	$\mathcal{L} > 5 \text{ MeV}_{ee}$	$\mathcal{L} > 12 \text{ MeV}_{ee}$
n_{trbg}	1366	581	1653	516
n_{tot}	24675	20192	9827	7414
n_{trbg}/n_{tot}	$5.5 \pm 0.2 \%$	$2.9 \pm 0.1 \%$	$16.8 \pm 0.4 \%$	$7.0 \pm 0.3 \%$

Table 4.2: The rates of tagged random background compared with total neutron rates.

\mathcal{T}_{CD} is not an essential ingredient in the particle identification and/or kinematics reconstruction, the contribution of random background events is usually estimated by histogramming \mathcal{T}_{CD} for the events that satisfy all selection cuts (except an explicit cut on \mathcal{T}_{CD}) and interpolating the rates on either side of the coincidence peak. This procedure must obviously be modified in the case where \mathcal{T}_{CD} is an essential input in the analysis of a TOF detector.

Figure 4.11 shows histograms the time-of-flight (mainly determined by \mathcal{T}_{CD} , see equation (4.4)). The spectra of the random background events are found to be flat, so that, before the application of selection cuts, in the physically allowable region ($5 < \mathcal{T} < 50 \text{ ns}$) the same rate of random background events may be assumed as outside that region. In order to estimate the number of random background events that survive the conditions (4.14) and are included in the sample of neutron candidate events we use the events with negative time-of-flight ($-50 < \mathcal{T} < -5 \text{ ns}$). After addition of 55 ns to the time-of-flight (keeping all other data unchanged) we can calculate the 'neutron' momentum and all other kinematic variables. The number n_{trbg} of these *tagged* random background events that survive all neutron selection cuts must be compared with the total number n_{tot} of neutron candidate events, see table 4.2.

The result depends strongly on the threshold for the amount of light \mathcal{L} produced in the E bars, since most of the random background involves low-energy particles (see figure 4.2). However, also the real ${}^3\text{He}(e, e'n)$ rate is higher for lower \mathcal{L} (figure 4.12). The relative contribution of random background events may be reduced by a factor 2 by choosing the higher threshold on \mathcal{L} , but only at the expense of about 16% in statistics.

The spectrum of the hit position of the (tagged) randoms in the E bars is not flat, as is shown in figure 4.14. The rate is higher at the side closest to the downstream beam pipe, which is hit by electrons that underwent small angle scattering in the target gas (beam blow-up). Much of the radiation emerging from this region hitting the E bars does not traverse the veto layers, so 'neutral

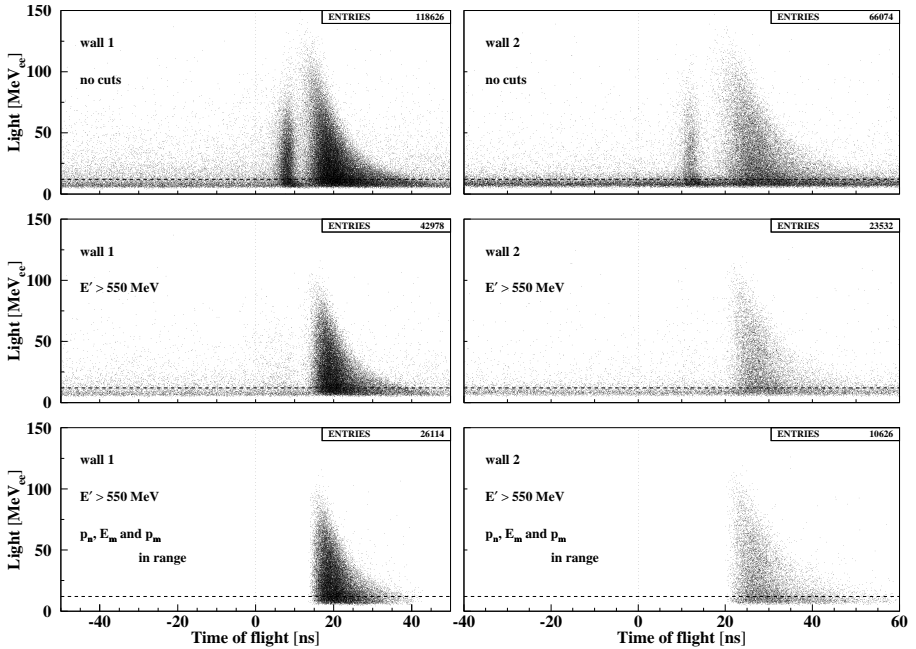


Figure 4.12: *Light in the E bars versus reconstructed Time-of-Flight for neutral particle events. In the upper two panels the vertical bands at $\mathcal{T} = 7 - 10$ ns and $\mathcal{T} = 11 - 14$ ns, respectively, correspond to particles that reach the ND with approximately the speed of light, so in these events most likely a photon was detected, which might result from the decay of a π_0 after neutral pion production. When $E' > 550$ MeV ($\omega < 170$ MeV) pion production is impossible and indeed we see in the middle panels that the bands have vanished. In the lower panels we assume that the detected particle was a neutron and require $0.2 < \beta < 0.8$, $-50 < E_m < 120$ MeV and $0 < p_m < 250$ MeV/c. This removes much of the background.*

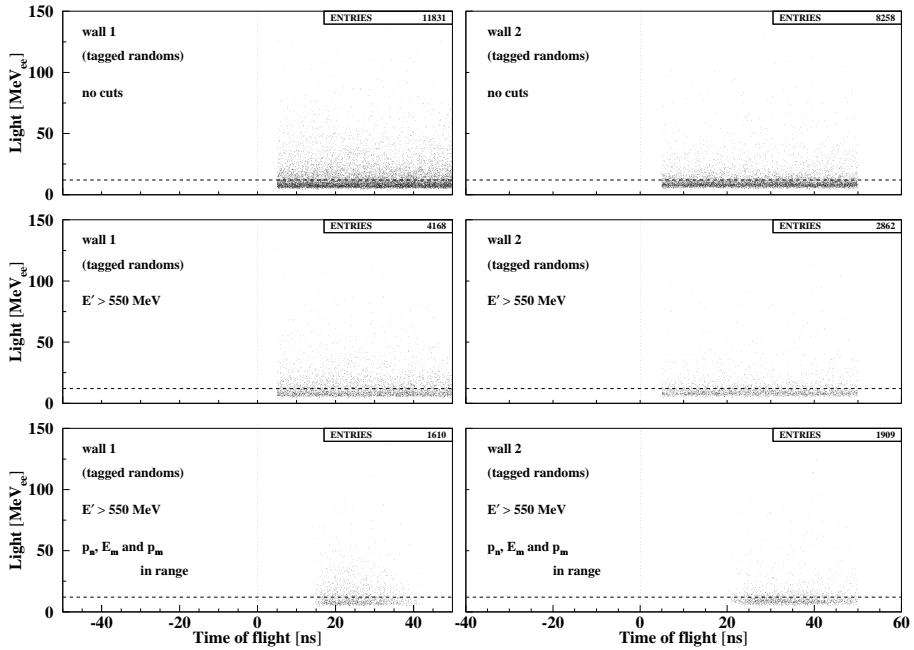


Figure 4.13: Light in the E bars versus reconstructed Time-of-Flight for tagged random neutral particle events, i.e. the events of the shaded area in figures 4.11(c) and 4.11(d). The cuts applied to these events are identical to those of the previous figure, fig. 4.12.

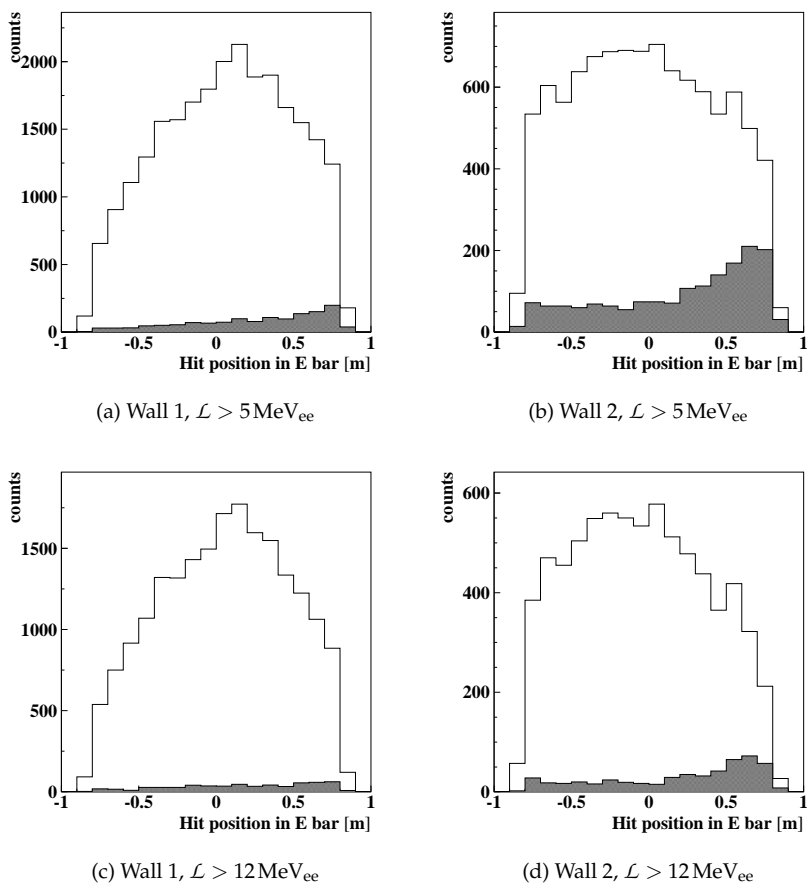


Figure 4.14: Position spectra of neutral hits and tagged random background events (shaded) that satisfy the conditions (4.14), with low threshold ($\mathcal{L} \geq 5 \text{ MeV}_{ee}$) and with high threshold ($\mathcal{L} \geq 12 \text{ MeV}_{ee}$) for the light in the E-bar.

hits' of this kind do not necessarily involve neutral particles.

The random background in the second wall is relatively higher than that in the first wall. The rate of real ${}^3\text{He}(e, e'n)$ events is twice as low because of the smaller solid angle with respect to the target cell (due to 1.4 times greater distance), whereas with respect to the downstream beampipe (the main source of random background) the two walls subtend a comparable solid angle.

Other sources of random background are low energy neutrons, which bounce all through the experimental hall, as well as radiation coming from the upstream beam line. The tuning of the photomultipliers of the second wall, finally, may not have been as good as that of the first wall, possibly causing a slight veto inefficiency.

4.5.2 Coincident background

As was described in section 4.4, $(e, e'\gamma)$ and pion production events are effectively eliminated by the conditions (4.14). The remaining sources of coincident background are:

- *veto inefficiency*: charged particles such as protons from ${}^3\text{He}(e, e'p)$ and ${}^{27}\text{Al}(e, e'p)$ may be misidentified as neutrons, *e.g.* if their tracks run through the narrow gaps between the veto layers of two adjacent telescopes.
- *conversion*: nucleons from ${}^3\text{He}(e, e'N)$ or ${}^{27}\text{Al}(e, e'N)$ may rescatter inside the Range Telescope (or other structures) to neutrons via processes like $C(N, n)$, $H(n, n)$ and $\text{Fe}(N, n)$.
- *cell wall hits*: ${}^{27}\text{Al}(e, e'n)$

Veto inefficiency

The contribution of misidentified charged particles to the coincident neutral background rate may be estimated using elastic $H(e, e'p)$ data (in runs where the Range Telescope was not in its position between the target and the TOF-detector). Elastic $H(e, e'p)$ events are selected cleanly with the requirement that $Q^2/2m_N\omega = 1$ and $\mathbf{p}_N \parallel \mathbf{q}$.

In figure 4.15 the light generated in the E bars by (the particles identified as) protons and neutrons (respectively) is plotted versus the reconstructed time-of-flight. Since in the selected kinematics there are no possible $H(e, e'n)X$ processes, the particles identified as neutrons were either misidentified or due to

some other process. Both plots show the typical proton characteristics: most of the events are in the correlation band at relatively large values of the amount of light in the E bar and some events have less light, due to tracks with only a short intersection with an E bar (see also the discussion on walk corrections on page 72).

If figure 4.15(b) would also contain a significant number of true neutron events, for instance from cell wall events, they would tend to concentrate at lower values for the light in the E bar (like in figure 4.12). The absence of these convinces us that we cleanly selected the elastic $H(e, e'p)$ events; all "neutrons" are misidentified protons in this figure.

Of the 22407 elastic $H(e, e'p)$ events (as defined above) 21768 events have a clear proton signature in the M and D layers and 580 are identified as a neutron (as in section 4.2.2). From this we conclude that the veto layers have an inefficiency of $2.7 \pm 0.2\%$. This is slightly worse than would be expected just from a geometrical consideration: the gap of about 2–3 millimeters between the veto layers (due to wrapping material) would account for at most 1–1.5 % inefficiency. From the elastic hydrogen data taken during the follow-up of this experiment, the measurement of ${}^2\vec{H}(\vec{e}, e'X)$, a veto inefficiency of $0.87 \pm 0.04\%$ was found [89], which *does* agree with the above mentioned geometrical consideration with a gap of 2 mm.

We assume that the veto inefficiency is independent of the nature of the (charged) particle. The contamination to a sample of neutron events can then be estimated by determining with the same data the number of charged particle events (not necessarily protons) which satisfy the same set of requirements as the neutron events and multiply this number with 0.027.

Conversion neutrons

The nucleons emerging from a ${}^3\text{He}(e, e'N)$ or $\text{Al}(e, e'N)$ scattering event may undergo a hadronic interaction in the material of the Range Telescope.

In the case of (p, n) conversion and subsequent detection of the neutron in the TOF-detector this would contribute to the coincident background rate. Since for ${}^3\text{He}(e, e'p)$ the spin correlation functions are an order of magnitude smaller than those for ${}^3\text{He}(e, e'n)$, this type of background only dilutes the $(e, e'n)$ asymmetries.

Due to the low nuclear interaction rate (of the order of 1% per cm for a 100 MeV nucleon in plastic) most of the protons have already lost (electromagnetically) a large fraction of their kinetic energy before the conversion; hence

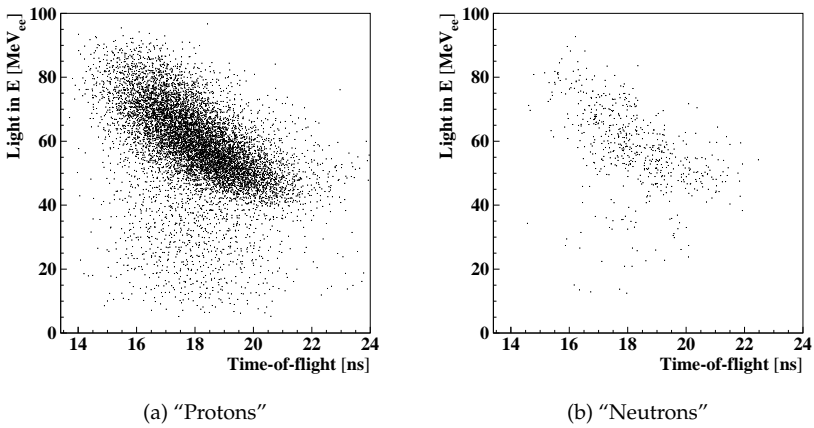


Figure 4.15: Scintillator light in the E bar versus time-of-flight for elastic scattering $H(e, e'p)$ events in which the particle in the TOF-detector was identified (a) as a proton and (b) as a neutron. The similarity of figure (a) and (b) confirms the assertion that the "neutrons" in (b) are actually protons, misidentified due to veto inefficiency.

the resulting neutron has a small kinetic energy ($T_n \lesssim 50 \text{ MeV}$) with a low detection probability (see figure 3.13). Hence only the (p, n) conversions taking place in the first few centimeters of the Range Telescope material can contribute at all.

In the case of neutrons they are either scattered out of the acceptance (neutron loss) or detected at angles and energies not corresponding to their momentum at the original ${}^3\text{He}(e, e'n)$ vertex (kinematically shifted neutrons). Neutron loss causes neither asymmetry dilution nor false asymmetries. The kinematically shifted neutrons can introduce a false asymmetry if the asymmetry is studied as a function of variables that depend on the neutron momentum. In particular when plotting versus the missing momentum p_m the asymmetry at high p_m (which is small in all theoretical models for both A'_x and A'_z) acquires in this way an admixture from the (theoretically large) asymmetry at low p_m .

The incoming rate of neutrons is an order of magnitude less than that of the protons. In contrast to (p, n) , (n, n) scattering can be both elastic and inelastic. Moreover, unlike the protons, the neutrons are not slowed down electromagnetically and hence neutrons scattering in any part of the Range Telescope (instead of only the first few centimeters) may contribute to the conversion background.

The (p, n) part of the conversion background may be estimated experimentally by comparing Hydrogen data *with* and *without* the Range Telescope in between the target and the TOF detector. Figure 4.16 shows the spectra of the position and the energy deposit (light in the E bar) for both charged particles and 'neutrons' in the two cases, for Hydrogen data taken after the A'_x run. The data has been analyzed like ${}^3\text{He}(e, e'n)$ data. No other background corrections have been taken into account in this figure.

In the data *with* the Range Telescope in its position the proton spectra (figures 4.16(a) and 4.16(a)) exhibit a clear 'shadow' (for hit positions between -0.2 m and $+0.5 \text{ m}$ and more for than 50 MeV_{ee} light). The neutron spectra have evident contributions from protons misidentified due to veto inefficiency (in the same regions) in the data *without* the Range Telescope.

In figure 4.17 the missing momentum spectra are shown for neutron events, *with* and *without* Range Telescope, with the known background contributions subtracted. In order to compare the sets quantitatively it is important to choose the proper normalization procedure. If the detected neutrons would be entirely due to (p, n) conversion of protons from elastic $\text{H}(e, e'p)$, the number of elastic events as identified by the BigBite electron spectrometer ($x_{Bj} = 1$) may serve as the normalization factor (figure 4.17(a)). If on the contrary the cell wall events (see next section) are the dominant contribution, the spectra should be

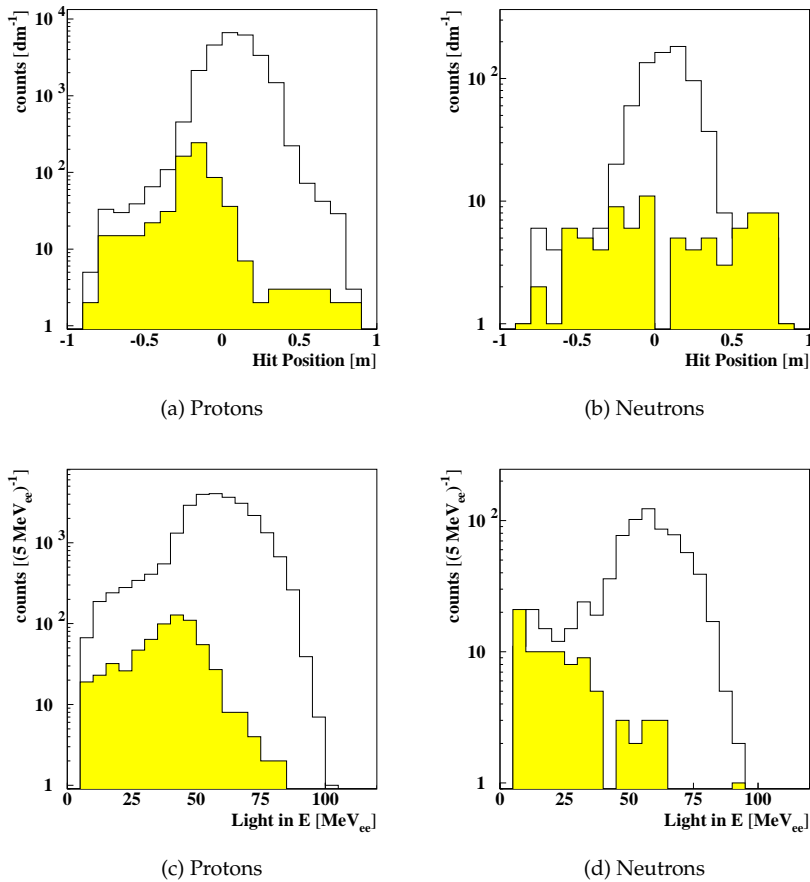


Figure 4.16: The hit position and scintillator light of protons and neutrons in hydrogen data runs with (shaded) and without (clear) the Range Telescope between the target and the TOF detector. The proton spectrum exhibits a clear shadow of the Range Telescope. Other sources of background (randoms, veto inefficiency) have not been corrected for in this figure. In particular the effect of veto inefficiency is clearly visible.

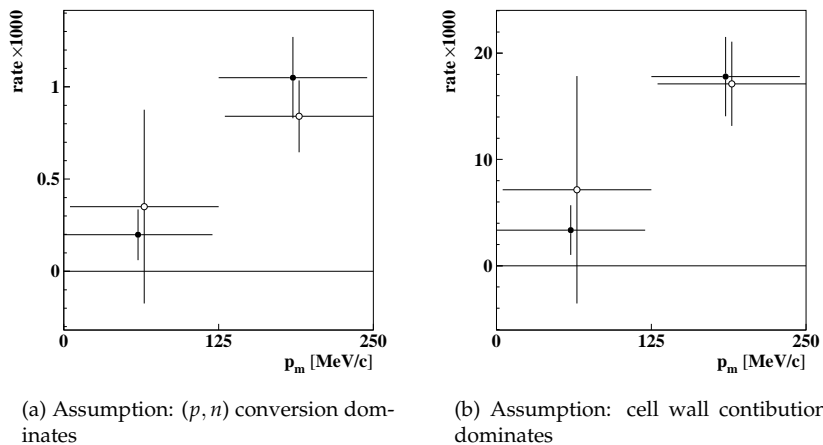


Figure 4.17: Neutron rates in Hydrogen data with (●) or without (○) Range Telescope. The "rate" is defined as the number of neutron events divided (a) by the number of elastic scattering events as determined by electron kinematics only; or (b) by the number of Helium nuclei from inelastic $\text{Al}(e, e'n)$ scattering, measured with the Recoil Detector.

normalized by the number of Helium nuclei detected in the Recoil Detector (figure 4.17(b)). The two normalizations do not lead to significantly different results, however. From figure 4.17(a) we might conclude that the conversion background from (p, n') in the Range Telescope is $0.02 \pm 0.02 \pm 0.02\%$ of the number of protons entering it.

Proton-neutron conversion may also take place in other structures such as the massive parts of the scattering box (the exit foil is too thin for a substantial conversion rate) or the downstream beam pipe. The kinematics for these processes are such that the resulting neutrons have a very small kinetic energy. The solid angle subtended by the TOF detector with respect to the conversion vertex in these structures is an order of magnitude smaller than the solid angle with respect to a conversion vertex inside the Range Telescope. Therefore, we believe that the remaining background is due to cell wall hits.

Cell wall hits

The background from cell wall hits in an electron scattering experiment is usually estimated by performing empty-target measurements. Unfortunately, in our experiment very few data were taken with an empty cell. Fortunately we do have some Hydrogen data in which the Recoil Detector was also operating, which provides us with an alternative way to estimate the cell wall background.

Since there is no (quasi-) elastic $H(e, e'n)$ process, we may, for our experiment, also study Hydrogen data to obtain an estimate for the cell wall contribution. After the subtraction of all other background contributions, any remaining events that survive the selection cuts (4.14) are attributed to electron scattering from the cell wall and to proton-neutron conversion in the Range Telescope. In the previous section we argued that the latter contribution is relatively small.

In internal target experiments only the halo of the beam traverses the cell wall. The *cell wall luminosity* depends on the gas density, the type of gas, the beam energy, the beam current and the beam tuning. The beam tuning varied during data taking, both on short and long time scales. Therefore, we cannot simply extrapolate the number of cell wall events from the Hydrogen data set to the A'_x and A'_z data sets by scaling with the collected charge.

A better way to obtain the cell wall luminosity is to measure other (e, X) reaction channels. The Recoil Detector gives access to such channels, namely $Al(e, {}^4\text{He})$ and $Al(e, {}^3\text{He})$. Obviously, the ${}^3\text{He}$ nuclei from elastic ${}^3\text{He}(e, e{}^3\text{He})$

must *not* be counted. In figure 4.18(a) we show how that is taken care of selecting only the upstream part (first 16 strips) of the Silicon X layer.

In figure 4.19 the $\Delta E/E$ plots and the corresponding mass plots are shown for Hydrogen, A'_x and A'_z data respectively. The mass plots are projections of the $\Delta E/E$ plots along the Bethe-Bloch curve, with an offset such that the " ^4He " band is projected onto positive values and the " ^3He " band onto negative values.

Since we have no information on the scattering vertex for the Recoil single events, the energy deposits have not been corrected for impact angle. Therefore, the elastically scattered ^3He nuclei with an impact angle of about 45° do *not* end up in the ^3He band but in the ^4He band.

The mass plots for the upstream part of the strip detectors have the same shape for all data sets. This confirms our assertion that the events in the upstream part are all due to scattering on the cell wall. After scaling these plots with an acceptance factor we may compare them with the mass plots for all strips together, which also include the elastic events. For the Hydrogen data, the two plots almost coincide, as should be expected. In the $^3\text{He}(e, e'n)$ data we see that in the A'_x the beam tuning was apparently considerably worse than during A'_z , resulting in an approximately 5 times lower a signal-to-background ratio.

The contribution of cell wall events to a neutron spectrum for $^3\text{He}(e, e'n)$ data may now be determined by producing the same spectrum for Hydrogen data and scaling it with the number of ^3He and ^4He events in the upstream part of the silicon detector. This correction may be done per polarization state, to eliminate false asymmetries. Such asymmetries might in principle arise due to a slightly different beam position for the two electron helicities due to inhomogeneous magnetic fields in the AmPS ring. We assume that the ^3He and ^4He knock-out from Aluminium do *not* depend on the electron helicity.

The background subtraction procedure we have just described assumes that the background from the upstream end of the target cell is proportional to that of the whole cell. If during the Hydrogen data taking the beam conditions were such that relatively more (less) electron scattering processes took place on the downstream part of the cell than during the A'_x and A'_z data taking, we will overestimate (underestimate) the cell wall background contribution. This must be taken into account in the systematic error. For a given observable we estimate this systematic error by taking 50% of the change of the observable induced by the cell wall background correction.

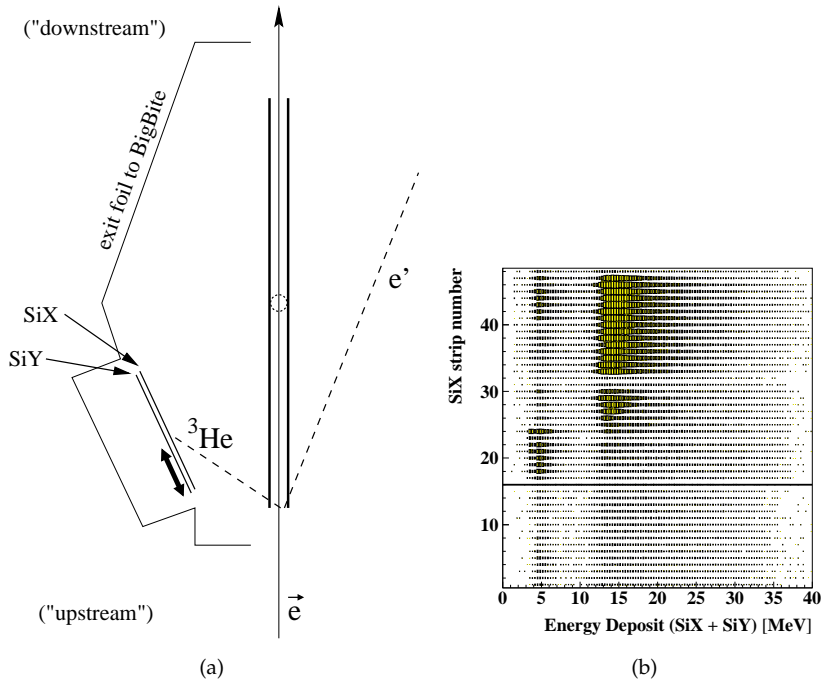


Figure 4.18: Figure (a) sketches the elastic scattering event at the upstream end of the cell with the largest angle for ^3He (lowest energy) such that the ^3He is just detectable in SiY. For all other (detectable) elastic scattering events the vertex is further downstream and/or the ^3He angle is less, so any ^3He (or ^4He) detected in the region indicated with a bold arrow cannot be due to elastic scattering. In (b) we show the SiX strip number (ascending in downstream direction) versus total energy deposit in the silicon layers of the Recoil Detector. The hits with an energy deposit more than 10 MeV correspond to ^3He and ^4He .

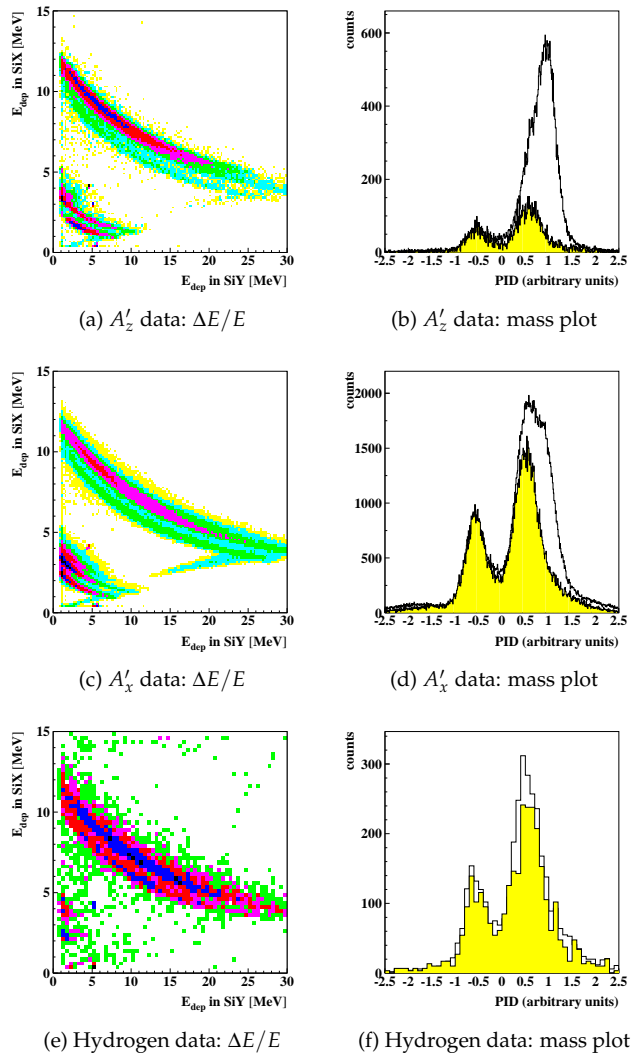


Figure 4.19: Counting ^3He and ^4He in the Recoil detector. The mass plot (see text) for only the upstream part (shaded) is normalized with a acceptance factor such that it can be compared with the mass plot for all silicon strips (not shaded).

Chapter 5

Results

In this chapter the results of the analysis of the A'_z and A'_x data on ${}^3\vec{\text{He}}(\vec{e}, e'n)$ are presented. The A'_z data were taken during three distinct periods; the results of these three periods are inconsistent with each other. This can be explained partially by a dependence of the electron polarization on the amount of injected current into the AmPS ring. The remaining, unexplained fluctuation is accounted for in the total error of the asymmetries.

From the A'_x data set we extracted values for G_E^n , the electric form factor of the neutron, using four different models. Using the model of Golak, which has been tested successfully in many experiments, we extract a value for G_E^n of 0.03 ± 0.03 (statistical error 0.02). Since the model of Golak cannot accurately describe the A_y^0 data which we took 1997 with the same experimental setup, we conclude that this G_E^n value has a non-negligible theoretical uncertainty, which is hard to estimate quantitatively.

5.1 A'_z result and systematic error analysis

Since the spin-spin correlation function A'_z is almost an order of magnitude larger than the spin-spin correlation function A'_x , a much smaller relative statistical error could be obtained than for A'_x , even with only half the number of events. Therefore, the measurement of A'_z is an interesting test for the models that we use to extract values for G_E^n from the result of our A'_x measurement. The smaller relative error is also useful in the investigation of the systematic error. We can use the result of this investigation in the analysis of the A'_x data.

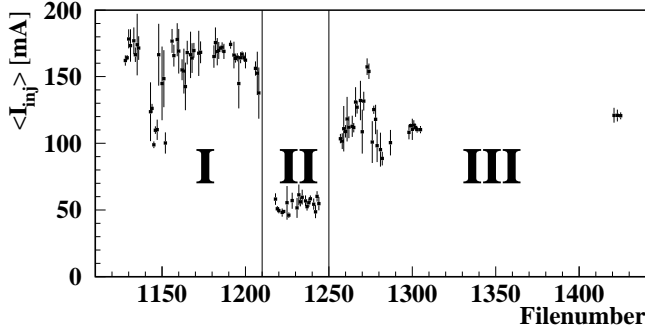


Figure 5.1: The average injection currents of the A'_z runs.

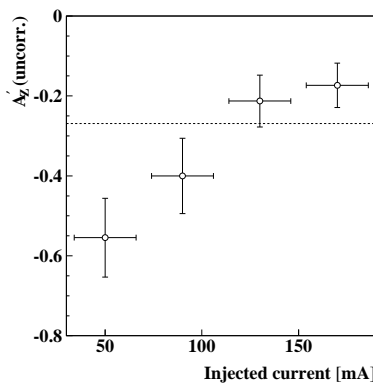
During the A'_z measurement the target polarization should have been aligned to the central \mathbf{q} value ($\theta_{lab}^* = 56^\circ$, $\phi_{lab}^* = 180^\circ$). After all data were taken the magnetic holding field was mapped and it turned out that the DC power supply of one of the Helmholtz coils had been connected incorrectly, so that effectively the field was aligned to an angle of $\theta_{lab}^* = 28^\circ$ (ϕ_{lab}^* unchanged). This has been taken into account in the Monte Carlo simulations.

5.1.1 Correlation of A'_z with the injected current

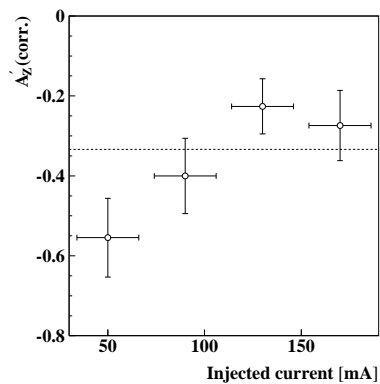
In figure 5.1 the average injected current is shown for each run of the A'_z data set. Each run has approximately ten “fills” (see figure 3.2); the average injected current $\langle I_{inj} \rangle$ of a run is the average of the values of the beam currents at the beginning of data taking of each fill, weighted with the dead-time corrected charge collected in that fill.

The results for the spin-spin correlation function A'_z , averaged over the full kinematic acceptance, obtained from the data taken in the three indicated periods, are -0.17 ± 0.05 (I), -0.52 ± 0.09 (II) and -0.22 ± 0.06 (III). The probability that these values are just statistical fluctuations from the average value of -0.235 ± 0.034 is only 0.4%.

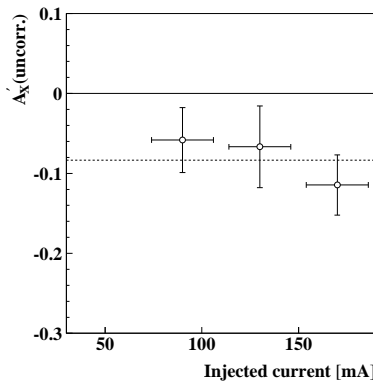
We have studied this fluctuation as a dependence on $\langle I_{inj} \rangle$. This is shown in figure 5.2(a), where in the chosen binning of $\langle I_{inj} \rangle$ (from 30 to 190 mA in bins of 40 mA) the data points of periods I and III are distributed over three current bins. For A'_x (figure 5.2(c)) there were no data taken with very low injected current ($I_{int} < 70$ mA).



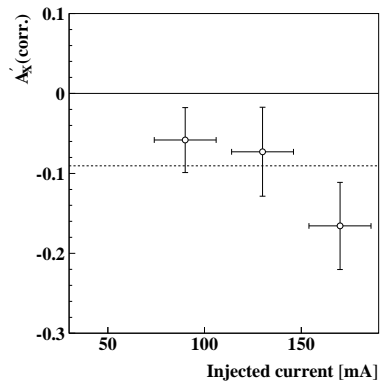
(a) A'_z as obtained *without* electron depolarization correction factor; $\chi^2/d.o.f. = 14/3$



(b) A'_z as obtained *with* electron depolarization correction factor; $\chi^2/d.o.f. = 8.4/3$



(c) A'_x as obtained *without* electron depolarization correction factor; $\chi^2/d.o.f. = 1.2/2$



(d) A'_x as obtained *with* electron depolarization correction factor; $\chi^2/d.o.f. = 2.6/2$

Figure 5.2: Average values of A'_z and A'_x versus inject current. The dashed line in each plot indicates the overall averages.

It should be noted that the correlation of the A'_z result with $\langle I_{inj} \rangle$ is *a priori* not necessarily due to a direct causal relation: in principle the correlation may be due to some other variation in the experimental conditions. However, we have not been able to identify another plausible source of such variations. Let us therefore assume for the moment that the correlation is indeed causal. We can think of three mechanisms through which the injection current might have caused a dilution of the asymmetry:

- The target polarization is degraded by inhomogeneities of the electromagnetic field of the electron beam (RF structure and gradient of the cylindrical magnetic field).
- Current dependent background dilutes the asymmetry.
- Current dependent depolarization of the electron beam.

The magnitude of the magnetic field gradient at a distance r of a linear direct current is $|\partial B/\partial r| = 2 \cdot 10^{-7} I/r^2$, which is of the order of 0.2 Gauss/mm for a beam size of 1 mm and a current of 100 mA. This is small compared to the strength of the holding field of 40 Gauss. In the HERMES experiment at HERA the target depolarization was studied at the end of the target cell with a so-called Target Optical Monitor [54]. No depolarization effect was found. The average current in the HERA ring was 30 mA, in bunches of 0.03 ns with 96 ns between each bunch, so that the field inhomogeneities induced by HERA were worse than in AmPS. The first hypothesis is therefore excluded.

As for the background: we have extensively studied all conceivable sources of background and found ways to estimate their contributions (see section 4.5). In the figures shown, all known background contributions have already been subtracted. We therefore also must drop the second hypothesis.

The third hypothesis, electron depolarization, was investigated using the Compton Backscattering Polarimeter (described in detail in ref. [89]). The result is plotted in figure 5.3. These data suggest that the electron polarization does not depend on the beam current for $\langle I_{inj} \rangle < 115$ mA, but that there is a linear decline for higher $\langle I_{inj} \rangle$. This simple relation may be implemented as a correction factor for the electron polarization, to be used in the calculation of spin correlation functions from the data. There is no conclusive physical description of the effect.

In figure 5.2 we show the average of the full kinematic acceptance versus injected current, with and without such a correction, for both A'_z and A'_x . The strong correlation of the A'_z values without applying a correction factor, figure 5.2(a), is diminished considerably by the correction, figure 5.2(b). When

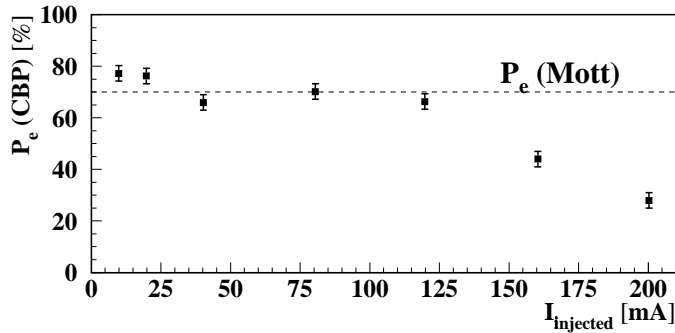


Figure 5.3: Current dependence of the electron polarization as measured with the Compton Backscattering Polarimeter. The dashed line indicates the value of the electron polarization as measured by the Mott polarimeter directly after the polarized electron source (PES).

we fit the corrected distribution with a constant we find a χ^2 of 8.4, which has (for 3 degrees of freedom) a probability of approximately 4%. Hence it is not very likely, but certainly not excluded that the electron depolarization as found with the Compton Backscattering Polarimeter is the only cause of the observed current dependence, and that the remaining trend seen in figure 5.2(b) is a statistical fluctuation.

In the A'_x data we do not see any hint of the electron depolarization; the data show no correlation with injection current, neither in figure 5.2(d) nor in figure 5.2(c). If there is indeed any other effect responsible for the trend in figure 5.2(b), it must as well have affected the A'_x data. If the effect is just changing slowly in time and not causally related to the beam current, the measured asymmetry in the A'_x data set does not necessarily correlate with the injected current in the same way as in the A'_z data set.

5.1.2 Conclusion on the systematic error

Part of the systematic fluctuations in the A'_z result can be explained in terms of current dependent electron depolarization. For the remaining part of the fluctuation we do not have a satisfactory explanation. It might, in principle, be a statistical fluctuation. If there is some other asymmetry changing effect, we cannot correct for it, since we do not know whether it is related to the beam

current, or to anything else.

This uncertainty is the dominant contribution to the systematic error. We quantify this error by defining the *total* error as 1.5 ($= \sqrt{(8.4 + 2.6)/(3 + 2)}$) times the statistical error; this puts the combined $\chi^2/d.o.f.$ of the A'_z and A'_x current dependencies equal to unity. In the plots on the following pages the outer error bars represent the total error and the inner error bars represent the purely statistical error. In fits and averages the total errors of separate (Q^2, p_m) bins are combined in the same way as statistical errors.

The only other possibly significant source of systematic error is the subtraction of cell wall background (see page 95). It is only (slightly) significant for A'_x , for which this error is added in quadrature to the total error.

5.1.3 Results

In figure 5.4 we show the spin-spin correlation function A'_z (corrected for current dependent electron depolarization) versus missing momentum p_m . Also shown are the electron asymmetry A_e , the induced asymmetry A_z^0 and the total numbers of counts and background estimates per polarization state. Since the (estimated) background contributions are small, their associated systematic errors are negligible.

In the A'_z result (figure 5.4(b)) we see a large asymmetry for small p_m , going to zero at larger p_m . This is in qualitative agreement with the predictions from the models of Golak and Nagorny. The magnitude of the asymmetry for small missing momenta ($p_m < 150 \text{ MeV}/c$) seems to be estimated also rather well by the model of Nagorny, while it is slightly overestimated by the model of Golak. For higher missing momenta ($p_m > 150 \text{ MeV}/c$) the calculations with Nagorny's model become unstable (because the helicity amplitudes for the D and higher partial waves in the rescattering could not be included) while Golak's curve agrees nicely with the data.

The electron asymmetry A_e (figure 5.4(c)) and the induced asymmetry A_z^0 (figure 5.4(d)) are zero or negligibly small in the calculations of Nagorny and Golak (zero in PWIA) except that the latter predicts a rise of A_z^0 at higher p_m , which is not quite supported by the data.

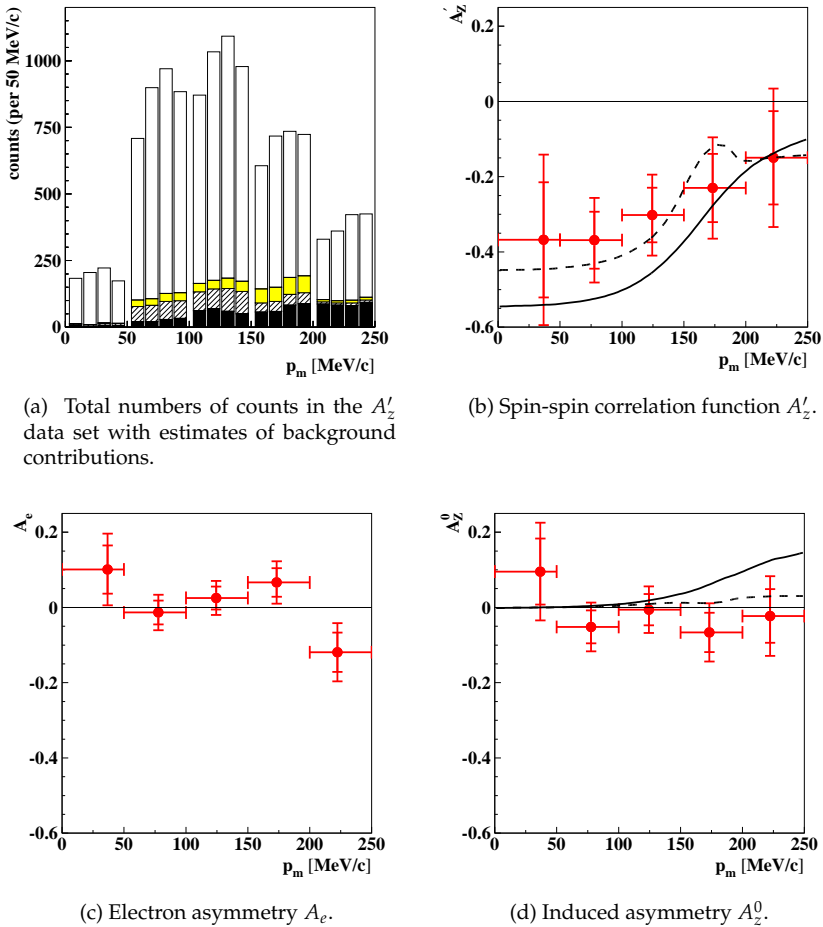
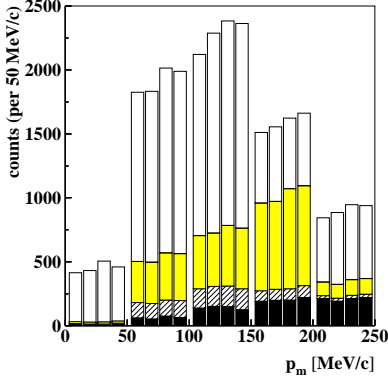
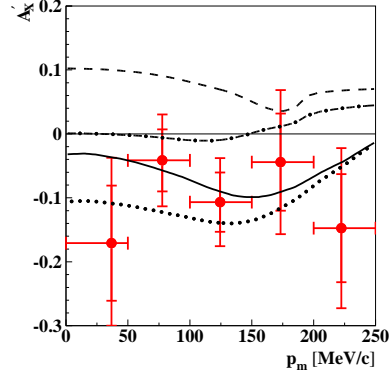


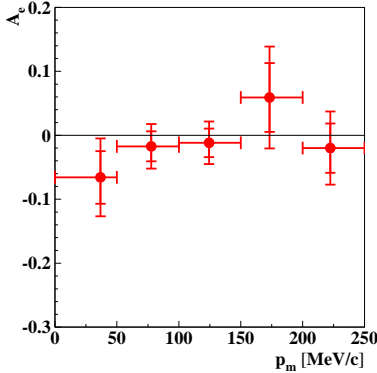
Figure 5.4: All available data from the A'_z data set with background estimates, and the three spin correlation functions. In figure (a), each p_m bin of 50 MeV/c has four histogram bars, corresponding to the four orientations of the polarization ($++$, $+-$, $-+$, $--$, respectively, where the first sign refers to the beam polarization and the second to the target polarization). The various shades indicate the (estimates for) various background contributions: random background (black), veto inefficiency (hatched), cell wall (grey). The curves in (b) and (d) give the results from calculations by Nagorny (dashed) and Golak (solid). The predictions for A_e (figure (c)) are consistent with zero.



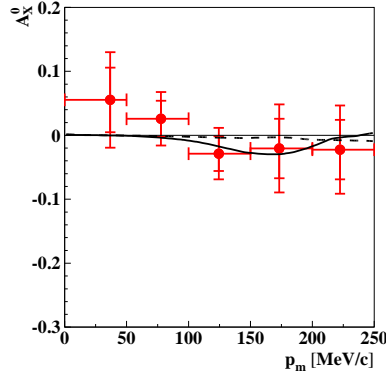
(a) Total available A'_x data. Legend: see figure 5.4.



(b) Spin-spin correlation function A'_x .



(c) Electron asymmetry A_e (in the A'_x data set).



(d) Induced asymmetry A_x^0 .

Figure 5.5: All available data from the A'_x data set, with background estimates ((a), legend the same as for figure 5.4(a)), and the three spin correlation functions (b,c,d). The curves in (b) and (d) present the results from calculations by Nagorny (dashed and dash-dotted, for $G_E^n = G_{E, Galster}^n$ and $G_E^n = 0$, respectively), and Golak (solid and dotted line, for $G_E^n = G_{E, Galster}^n$ and $G_E^n = 0$, respectively). The predictions for A_e (figure (c)) are consistent with zero.

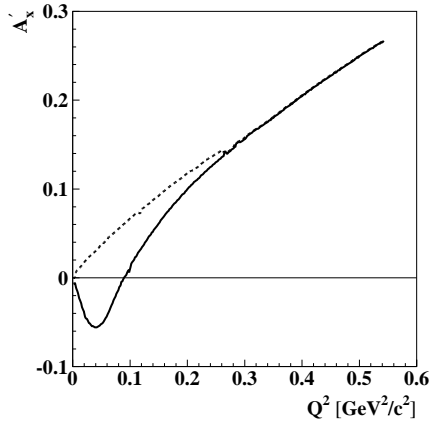


Figure 5.6: The Q^2 dependence of A'_x in ${}^3\text{He}(\vec{e}, e'n)$ at $p_m = 0$ for PWIA (dashed) and with FSI (full) by Laget [44].

5.2 A'_x and G_E^n

5.2.1 The experimental result

In figure 5.5 the A'_x spin-spin correlation function is shown versus the missing momentum p_m . Also shown are the total numbers of counts with background estimates, as well as the electron asymmetry A_e and the induced asymmetry A_x^0 (which should both be close to zero according to theory). The measured asymmetries are indeed within the errors consistent with zero.

An important aspect of the result for A'_x is the sign, which we find to be negative (equal to that of A'_z). We have convinced ourselves that the equality of the signs of A'_x and A'_z is not due to some experimental mistake. The optical elements for both the polarization and the polarimetry of the target could be mounted in only one way. Therefore, it is impossible that during rearrangements of the target setup (between the dedicated elastic run and the A'_z data taking and between the A'_z and A'_x data taking) the definitions of the sign of the target polarization and the polarimeter were inadvertently flipped. The measurements with the CBP of the electron polarization have the correct sign throughout all data sets.

A shift to negative values, induced by FSI in the small Q^2 range, was pre-

dicted qualitatively by Laget [44], see figure 5.6. In these calculations the missing momentum p_m is put to zero and rescattering is taken into account only to first order. This might be the reason why the predicted zero-crossing is at $Q^2 \approx 0.1 \text{ GeV}^2/c^2$, while based on our experimental result and the assumption that for larger Q^2 the result should converge to the PWIA(S) prediction we would expect it between 0.2 and 0.3 GeV^2/c^2 .

In the full calculations of Golak, A'_x also acquires an FSI-induced offset at small Q^2 , shifting the asymmetry to negative values for both $G_E^n = 0$ and G_E^n equal to the Galster parametrization. In ref. [96] a series of calculations with Q^2 running from 0.05 GeV^2/c^2 to 0.5 GeV^2/c^2 is presented where \mathbf{p}_n is parallel to \mathbf{q} and for G_E^n the Höhler parametrization is used. The zero-crossing takes place around 0.2 GeV^2/c^2 .

Hence we might expect in addition to the observed negative offset also a rising trend of A'_x with Q^2 in our data. However, in our experiment, which covers a large range in Q^2 ($0.14 < Q^2 < 0.26 \text{ GeV}^2/c^2$), this FSI induced trend is dominated by the admixture from the much larger A'_z spin-spin correlation function, which causes an *opposite* trend (see figure 5.7). For quasi-elastic kinematics with Q^2 values larger (smaller) than the central value of 0.2 GeV^2/c^2 the \mathbf{q} vector is at a smaller (larger) angle with respect to the electron beam (hence \mathbf{q} is not perpendicular to the target spin vector) so that the measured asymmetry gets a negative (positive) admixture from A'_z .

5.2.2 Extraction of G_E^n

Figure 5.7 shows the measured values of A'_x versus Q^2 together with curves obtained from a Monte Carlo simulation with G_E^n put either to zero or equal to the Galster parametrization (see refs. [16, 40] or equation 2.87). The average value of the Galster parametrization in the Q^2 range of our experiment is 0.05.

If we assume that the curves of $A'_{x,\alpha}$ as obtained from the Monte Carlo simulation using model α (where α denotes the model of Nagorny or Golak) depend linearly on the value of G_E^n used in the calculation; i.e.:

$$A'_{x,\alpha}(\xi, Q^2) = (1 - \xi)A'_{x,\alpha}(0, Q^2) + \xi A'_{x,\alpha}(1, Q^2), \quad (5.1)$$

(where $A'_{x,\alpha}(\xi, Q^2)$ denotes $A'_{x,\alpha}$ calculated with $G_E^n = \xi G_{E,Galster}^n$) then we obtain a value for $G_{E,\alpha}^n$ by solving ξ in a one-parameter fit to the data. We find:

$$\begin{aligned} G_{E,Nagorny}^n &= -0.049 \pm 0.026(0.017) \\ G_{E,Golak}^n &= +0.031 \pm 0.034(0.023) \end{aligned}$$

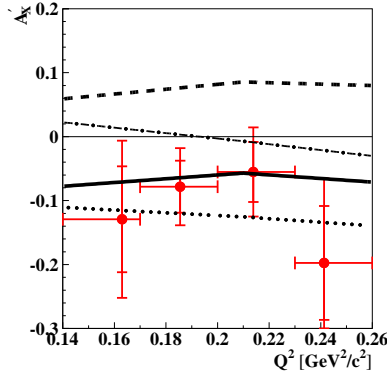


Figure 5.7: The A'_x spin-spin correlation function versus Q^2 ; the legend for the curves is the same as in figure 5.5.

where the quoted error is the total error as explained in the conclusion of section 5.1, and the number in parentheses is the purely statistical error. With PWIA and PWIAS we would obtain the values $-0.056 \pm 0.023(0.016)$ and $-0.056 \pm 0.018(0.012)$, respectively¹.

Strictly speaking, the electric form factor of a bound neutron is not an observable (as explained in 2.3) and $G_{E,\alpha}^n$ only has a meaning within the particular model with which it was extracted from A'_x . However, the models of Nagorny and Golak both aim to separate the effects of nucleon structure from those of the nuclear structure and reaction mechanisms, so that the extracted G_E^n values ought to be the same.

Independent checks with observables other than A'_x in $(e, e'n)$ are necessary to establish the level of confidence we may have that a model can effectively separate the various effects². Our experiment was specifically designed [47]

¹The fact that both values are equal to -0.056 is a numerical coincidence.

²Conversely, instead of using a model to obtain a 'measurement' of G_E^n one may interpret the (in-)compatibility of the extracted G_E^n with the existing experimental data as a test of the ability of the model to incorporate consistently the effects of nuclear structure, nucleon structure and reaction mechanisms. In such an interpretation, the negative value for $G_{E,Nagorny}^n$ (which deviates approximately four standard deviations from the existing data) would indicate that the model of Nagorny does not pass this test, while the model of Golak does. One must then conclude that a (more) thorough incorporation of FSI is mandatory for a reliable description of the polarization observables in electrodisintegration of ${}^3\text{He}$.

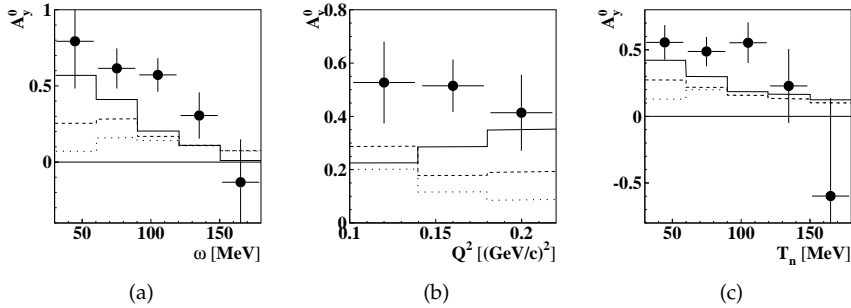


Figure 5.8: Results for A_y^0 for the 1997 data set of ${}^3\text{He}(e, e'n)$, shown versus energy transfer (a), four-momentum transfer (b), and neutron kinetic energy (c). The curves are produced with a Monte Carlo simulation using the models of Golak (solid) and Nagorny with one loop (dotted) or two loops (dashed). PWIA and PWIAS predict the A_y^0 to be equal to zero.

to provide such observables. In the A'_z data set it turns out (see figure 5.4) that the model of Nagorny can reliably describe the data for $p_m < 150 \text{ MeV}/c$ while the predictions from the model of Golak are slightly off. In the first run of the ${}^3\vec{\text{He}}(\vec{e}, e'X)$ experiment in 1997 we measured the induced asymmetry A_y^0 with the same setup as described in this thesis, except that the BigBite spectrometer was positioned at 35° instead of 40° so that Q^2 was centered around $0.16 \text{ GeV}^2/c^2$ instead of $0.21 \text{ GeV}^2/c^2$. The latest results of the analysis and the Monte Carlo simulations of the $(e, e'n)$ channel in that experiment [102] are shown in figure 5.8. Neither model can well describe the experimental data. The description provided by the model of Golak is closest to the data, but in large parts of the acceptance there is a discrepancy of several standard deviations, although figure 5.8(b) suggests that the discrepancy may be smaller in the kinematic range of the A'_x data set ($0.14 < Q^2 < 0.26 \text{ GeV}^2/c^2$).

In other experiments the predictions from the model of Golak were in many cases in impressive agreement with the data, for *e.g.* Nd scattering (see ref. [43]), ${}^3\text{He}(e, e'p)$ (in [53] excellent agreement with the data from [31] is shown) and recently for polarized inclusive electron scattering at Jefferson Lab [94]. For ${}^3\text{He}(e, e'd)p$ Nagorny's model seems to agree slightly better with the experimental data [98, 69] than the model of Golak.

We therefore conclude that neither model has yet attained the required level of confidence for a reliable extraction of G_E^n . At present we would prefer the

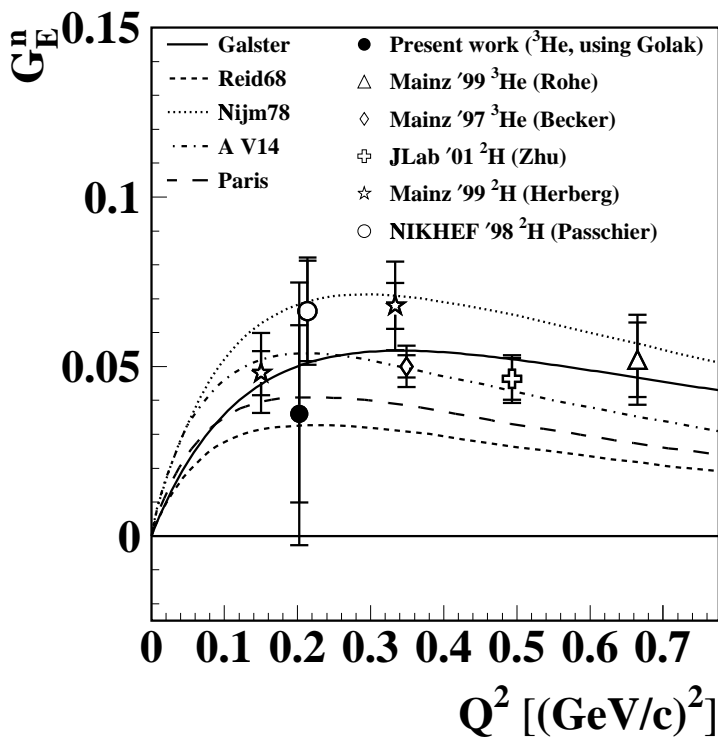


Figure 5.9: The G_E^p values as extracted from double polarized electron scattering experiments. The curves correspond to fits to the Platchkov data [40] when interpreting their scattering data using the Paris (solid curve), Reid68 (dashed curve), Nijmegen78 (dotted curve) or Argonne V14 (dash-dotted curve) potential. The NIKHEF '98 ${}^2\text{H}$ data point has been shifted to a slightly higher Q^2 value to avoid collision with the data point of the present work.

calculations of Golak, because the effects of FSI, which are most thoroughly taken into account in his model, seem to be decisively important in polarization observables in ${}^3\text{He}(\vec{e}, e'n)$. This is demonstrated by the A_y^0 result, which however also shows that the model of Golak still needs significant improvements. These improvements may also change the predictions for A_x' and hence the extracted value for G_E^n . This is a theoretical uncertainty in our G_E^n result which we cannot quantify.

The G_E^n value extracted by using the full calculation of Golak is displayed in figure 5.9, together with the results for G_E^n obtained from previous polarized electron scattering experiments. The ${}^3\text{He}$ Mainz results [73, 74] are extracted from the ratio of the measured A_\perp and A_\parallel . Originally the extraction was performed using a PWIA model, later the effect of FSI on A_\perp/A_\parallel was calculated by Golak, resulting in a significantly higher value for G_E^n .

5.2.3 Conclusion

The sign of the result of our measurement of A_x' is a qualitative confirmation of the prediction by Laget [44] that at low Q^2 the A_x' spin-spin correlation is shifted to negative values due to FSI.

The extraction of G_E^n from the A_x' spin-spin correlation is very model dependent. Choosing the model of Golak (which has been successful in the description of various intermediate energy scattering processes involving 3N-systems) we obtain a value of $+0.03 \pm 0.03(0.02)$ which is consistent with the present world data set. However, from the latest analysis of the measurement of the induced asymmetry A_y^0 it was found [102] that the curves based on Golak's calculations significantly underestimate the experimental data. Improvements to the model may strongly affect the extracted value of G_E^n .

5.3 Outlook

The ${}^3\text{He}(\vec{e}, e'X)$ experiments in 1997 and 1998 at NIKHEF had a pioneering character. Performing polarized electron scattering experiments is not a simple extension of unpolarized electron scattering, it takes a few years to explore the new running conditions and to learn to avoid new pitfalls. However, the accelerator was scheduled to be closed down by the end of 1998, so that effectively we had to take the data during the learning stage.

During two weeks in September 1996 we tested the complete experimental setup with polarized electrons, a polarized ${}^3\text{He}$ target and all detectors. In

the spring of 1997 the first measurement ${}^3\vec{\text{He}}(\vec{e}, e'X)$ was performed. During the start-up of that experiment the Siberian Snake, which preserves the electron polarization in the AmPS ring, had suffered a destructive quench and could be operated only partially. Therefore, first the A_y^0 asymmetries were measured with an unpolarized 720 MeV electron beam, with injected currents up to 200 mA. A measurement of A_y^0 was performed with a beam energy of 442 MeV (close to the magic energy, for which the electron spin precesses exactly 360°), with fairly low injected currents of 20-30 mA. In these measurements a relatively low background and no depolarization effects were found.

The main lessons learnt from that experiment were:

- We had a functioning polarized ${}^3\text{He}$ target system.
- Even though we could use the Siberian Snake only partially, it was shown that a longitudinally polarized electron beam could be stored in AmPS and used for experiments in the internal target facility.
- Our data acquisition system could handle four fast counting detectors, where the trigger rate of the TOF-detector had been reduced by using a low level trigger signal from the BigBite spectrometer.
- The A_y^0 result indicated that for the description of polarization observables in $(e, e'n)$ PWIA is inadequate. The models of Golak and Nagorny had been calculated only in the central kinematics; the curves from the Monte Carlo using the model of Golak coincided with with the data. (In the full Monte Carlo, which was completed only in 2001, none of the models yields curves consistent with the experimental data.)

The measurement in the spring of 1998 of A_z' was the first double polarization experiment with a high current ($I > 100$ mA) polarized electron beam. After collecting all A_z' data the dependence of the electron polarization on the injected current was studied with the CBP. When the conclusion that data should be taken with injection currents lower than 110 mA was finally accepted, the A_x' measurements were already well underway, with all data until then taken with high currents ($I_{inj} > 140$ mA).

The very low random background rate and the low rates for coincident background during the A_y^0 and A_z' measurements had made it seem not compulsory to perform $\text{H}(e, e'N)$ and empty target measurements. The other reason for $\text{H}(e, e'N)$ measurements, namely the recalibration of the Time-of-Flight detector, was set aside because for those measurements the Range Telescope

would have to be removed (and reinstalled afterwards), which would have been very time consuming. To make things worse, the slits (which in normal operation served as collimators for the beam and drastically reduced cell wall background), were left out during the A'_x measurement, because they were suspected to depolarize the electron beam. Due to these factors the cell wall background in the $(e, e'n)$ channel was much higher in the A'_x data set than in the A'_z data set, and its contribution was hard to estimate.

The ${}^3\vec{H}(\vec{e}, e'X)$ experiment was followed by the ${}^{1,2}\vec{H}(\vec{e}, e'N)$ and $N \rightarrow \Delta$ experiments. In these experiments many of the above mentioned mistakes were avoided: the injected currents were kept below 100 mA and unpolarized hydrogen and empty target measurements were made on a regular basis. The Range Telescope was removed from the setup and protons and deuterons were measured with a slightly worse energy resolution in the Time-of-Flight-detector, which provided (apart from $(e, e'p/d)$ scattering data) many more systematic checks for the stability of gains, offsets and efficiencies.

Based on these experiences we can make the following remarks and recommendations for future measurements of spin correlation parameters in internal target facilities:

- Thorough investigations of the properties of the polarization of stored electrons are necessary, in particular of the correlation of the polarization with *e.g.* the injected current, the instantaneous current, the injection process, the type and density of the target gas, the rest gas pressure, and with the geometry of the storage ring.
- In experiments with large acceptance detectors, random and coincident background rates may be completely uncorrelated.
- Preferably, the experimental setup should allow the simultaneous measurement of a spin correlation function in an already well-known reaction channel, which can provide an independent measurement of the product of beam and target polarization. During the ${}^2\vec{H}(\vec{e}, e'N)$ measurements the ${}^2\vec{H}(\vec{e}, e'p)$ for small missing momenta could be used for this purpose.
- For intermediate energy scattering experiments on ${}^3\text{He}$ and larger nuclei, the presently available theoretical models of electrodisintegration are not reliable enough to extract electromagnetic form factors. New models and improved versions of existing models should at least be able to give an accurate prediction of the A_y^0 induced asymmetry and the A'_x spin-spin

correlation, which should both be measured as a function of Q^2 in the entire low Q^2 range (up to $0.5 \text{ GeV}^2/c^2$) with much better statistical accuracy than the presently available data.

When (if ever) a technique will be developed to measure the electromagnetic form factors of the *free* neutron for Q^2 larger than $0.1 \text{ GeV}^2/c^2$, then we can compare this value with those extracted from electron scattering on deuterium and ^3He . This would provide an important test for modern (and future) models of intermediate energy electron scattering whether they can truly disentangle the effects of nucleon structure, nuclear structure and reaction mechanisms. Here the term 'reaction mechanisms' includes in particular the electromagnetic interaction with the constituents of the nucleus: the consistent treatment of gauge invariance and the coupling to offshell particles is still an unresolved issue for theoretical debate (see section 2.3).

Another interesting contribution to the knowledge and understanding of the three-nucleon system would be a measurement of $^3\vec{\text{H}}(\vec{e}, e'p)nn$ [93]. The reaction can be described with exactly the same formalism as $^3\vec{\text{H}}e(\vec{e}, e'n)$. Since the electromagnetic coupling is smaller for a neutron than for a proton, the effects of FSI (or rather: symmetrization) are probably less than for $^3\text{He}(e, e'n)$. An extracted value for G_E^p from the A'_x spin-spin correlation parameter in this channel should then be compared to the well-known value from elastic electron-proton scattering. However, although the development of a polarized tritium target may be slightly easier than a free neutron target, it is still a very ambitious project due to the very serious safety issues.

Chapter 6

Summary

We have measured polarization observables of the ${}^3\text{He}(e, e'n)$ reaction using the MEA/AmPS electron accelerator facility at NIKHEF in Amsterdam, The Netherlands. A 60% polarized beam of electrons with an energy of 720 MeV was led through an internal target with 50% polarized ${}^3\text{He}$ gas. Scattered electrons were observed with a large acceptance magnetic spectrometer and the neutrons were detected in a time-of-flight detector.

The longitudinal asymmetry A'_z and the transverse asymmetry A'_x were measured in a Q^2 range of 0.14-0.26 GeV^2/c^2 and a missing momentum range of 0-250 MeV/c , in two separate measurements with identical setups. From the data of the measurement of A'_z , we found that the result had a strong anomalous dependence on the beam current. This could be explained partially by the degradation of the polarization of the electron beam for injected currents greater than (approx.) 110 mA. The remaining dependence has been translated into a systematic error, although it cannot be excluded that this fluctuation is just statistical.

Monte Carlo (MC) simulations of the experiment have been performed using two fundamentally different calculations of the polarization dependent cross section of ${}^3\text{He}$ electrodisintegration. The calculations of Nagorny are based on a Lorentz covariant approach, with emphasis on gauge invariance with consistent allowance of the internal structure of the nucleons. Rescattering of the nucleons after absorption of the virtual photon (or Final State Interactions, FSI) could be taken into account to second order. The calculations of Golak (and the Bochum nuclear theory group) are based on (nonrelativistic)

Faddeev equations for the 3N continuum states. In a Faddeev equation FSI are by definition taken into account to all orders.

All calculations (and simulations) were performed twice: once with the assumption that G_E^n , the electric form factor of the neutron, is equal to the Galster parametrization (which is close to the existing data on G_E^n , and takes the value 0.05 for $Q^2 = 0.2 \text{ GeV}^2/c^2$), and once with the assumption that $G_E^n = 0$. The MC results with these two different assumptions were nearly identical for the A'_z asymmetry, but significantly different for A'_x .

The MC results for A'_z agreed reasonably well with the experimental data; slightly better with Nagorny's calculations than with the Bochum calculations.

For A'_x , we measured small negative values, while the MC simulations using Nagorny's calculations (or lowest order calculations, PWIA) predict A'_x to be positive for $G_E^n = G_{E, Galster}^n$ and close to zero for $G_E^n = 0$. For $p_m > 150 \text{ MeV}/c$ the calculations converge. Using the calculations of Golak the MC yields negative values for A'_x if $G_E^n = 0$ and closer to zero (but still negative) if $G_E^n = G_{E, Galster}^n$.

The MC results and the experimental data for A'_x can be compared in two different ways: *either* we use the data to extract values for G_E^n (within the context of each particular model), *or* we boldly assume that the electric form factor of a neutron (bound in a ${}^3\text{He}$ nucleus) is equal to the Galster fit and we use the data to test whether the models can give an adequate description of the nuclear dynamics.

In the first interpretation, we would obtain $G_{E, Golak}^n = 0.031 \pm 0.034(0.023)$ and $G_{E, Nagorny}^n = -0.049 \pm 0.026(0.017)$, where the numbers in parentheses are the purely statistical errors. In principle these values for G_E^n have a well-defined meaning only within the respective models; and a comparison with other data on G_E^n only makes sense if we have confidence that a model can take *all* relevant effects accurately into account. However, we have also measured the analyzing power A_y^0 (in 1997, with the same setup) and for those data Golak's calculations give a better description than Nagorny's calculations, but the agreement is not satisfactory. An improvement in the calculations will probably also change the predictions for A'_x , and hence the G_E^n extraction.

In the second interpretation, we would conclude that the Faddeev calculations agree better with the data than Nagorny's calculations. This is then probably due to the higher order contributions from FSI. These cause a negative offset to A'_x , compared to a lowest order calculation (PWIA).

Bibliography

- [1] E. Rutherford, *Phil. Mag.*, sixth series, **21** (1911) 669 and **37** (1919) 537.
- [2] P.A.M. Dirac, *Proc. Roy. Soc. London*, **A117** (1928) 610.
- [3] N.F. Mott, *Proc. Roy. Soc. London*, **A124** (1929) 425.
- [4] J. Chadwick, *Proc. Roy. Soc. London*, **A136** (1932) 692.
- [5] W.W. Havens Jr., I.I. Rabi, L.J. Rainwater, *Phys. Rev.* **72** (1947) 634, *Phys. Rev.* **82** (1951) 345:Z7.
- [6] E. Fermi and L. Marshall, *Phys. Rev.* **72** (1947) 1139.
- [7] M.N. Rosenbluth, *Phys. Rev.* **79** (1950) 615.
- [8] J.C. Ward, *Phys. Rev.* **78** (1950) 182.
- [9] R. Hofstadter *et al.*, *e.g.* *Phys. Rev.* **92** (1953) 978, *Phys. Rev.* **95** (1954) 512, *Phys. Rev.* **98** (1955) 217.
- [10] Y. Takahashi, *Nuov. Cim.* **6** (1957) 371.
- [11] G. Derrick and J.M. Blatt, *Nucl. Phys.* **8** (1958) 310.
- [12] Adam M. Bincer, *Phys. Rev.* **118** (1960) 855.
- [13] R.G. Sachs, *Phys. Rev.* **126** (1962) 2256; F.J. Ernst *et al.*, *Phys. Rev.* **119** (1960) 1105 .
- [14] A.A. Sokolov and I.M. Ternov, *Sov. Phys. Doklady*, **8** (1964) 1203.
- [15] R.A. Malfliet and J.A. Tjon, *Nucl. Phys.* **A127** (1969) 161.

- [16] S. Galster *et al.*, *Nucl. Phys.* **B32** (1971) 221.
- [17] G. Höhler *et al.*, *Nucl. Phys.* **B114** (1976) 505.
- [18] I.R. Afnan and N.D. Birrell, *Phys. Rev. C* **16** (1977) 823.
- [19] N. N. Bogoliubov and D. V. Shirkov, *Introduction to the Theory of Quantized Fields*, 3rd edition, John Wiley & Sons, 1979.
- [20] R.A. Cecil *et al.*, *Nucl. Instr. and Meth.* **161** (1979) 439.
- [21] E.L. Lomon, *Ann. Phys.* **125** (1980) 309.
- [22] C. Ciofi degli Atti *et al.*, *Phys. Rev. C* **21** (1980) 805.
- [23] C. Itzykson and J.-B. Zuber, *Quantum Field Theory*, McGraw-Hill 1980.
- [24] G.G. Simon *et al.*, *Nucl. Phys.* **A364** (1981) 285.
- [25] E. Jans *et al.*, *Phys. Rev. Lett.* **49** (1982) 974, *Nucl. Phys.* **A475** (1987) 687.
- [26] T. de Forest Jr., *Nucl. Phys.* **A392** (1983) 232.
- [27] H. Meier-Hajduk *et al.*, *Nucl. Phys.* **A395** (1983) 332.
- [28] B. Blankleider and R.M. Woloshyn, *Phys. Rev. C* **29** (1984) 538.
- [29] D.O. Riska, *Physica Scripta* **31** (1985) 107.
- [30] M.F. Gari and W. Krümpelmann, *Z. Phys.* **A322** (1985) 689, *Phys. Lett.* **B274** (1992) 159.
- [31] P.H.M. Keizer *et al.*, *Phys. Lett.* **B157** (1985) 255, *Phys. Lett.* **B197** (1987) 29; P.H.M. Keizer, Ph.D. thesis, Universiteit van Amsterdam 1986.
- [32] R. Machleidt *et al.*, *Phys. Rep.* 14919871
- [33] H.W.L. Naus and J.H. Koch, *Phys. Rev. C* **36** (1987) 2459.
- [34] W. Paul *et al.*, *Z. Phys.* C45198925; K.J. Kügler *et al.*, *Nucl. Instr. and Meth.* **A228** (1985) 240
- [35] R. Henneck *et al.*, *Nucl. Instr. and Meth.* **A259** (1987) 329.
- [36] A.S. Raskin and T.W. Donnelly, *Ann. Phys.* **191** (1989) 78.

- [37] E. van Meijgaard, Ph.D. thesis, Utrecht 1989.
- [38] S.I. Nagornyi *et al.*, *Yad. Fiz. (Soviet Journal of Nuclear Physics)* **49** (1989) 465.
- [39] H.W.L. Naus, Ph.D. thesis, Universiteit van Amsterdam 1990.
- [40] S. Platchkov *et al.*, *Nucl. Phys.* **A510** (1990) 740.
- [41] P.C. Tiemeijer, J.A. Tjon, *Phys. Rev. C* **42** (1990) 599.
- [42] E. van Meijgaard and J.A. Tjon, *Phys. Rev. Lett.* **57** (1986) 3011, *Phys. Rev. C* **42** (1990) 74+96, *Phys. Rev. C* **45** (1992) 1463.
- [43] H. Shimizu *et al.*, *Nucl. Phys.* **A382** (1982) 242; H. Rühl *et al.*, *Nucl. Phys.* **A524** (1991) 377; H. Sakai *et al.*, *Phys. Rev. Lett.* **84** (2000) 5288; N. Sakamoto *et al.*, *Phys. Lett.* **B367** (1996) 60; H. Patberg, Ph.D. thesis, Köln, 1995, unpublished; M. Allet *et al.*, *Few Body Systems* **20** (1996) 27; G. Rauprich *et al.*, *Nucl. Phys.* **A535** (1991) 313; J. Zejma, Ph.D. thesis, Kraków, 1995, unpublished.
- [44] J.M. Laget, *Phys. Lett.* **B273** (1991) 367.
- [45] R.-W. Schulze and P.U. Sauer, *Phys. Rev. C* **48** (1993) 38.
- [46] A. Zondervan *et al.*, *Nucl. Instr. and Meth.* **A342** (1994) 436.
- [47] R. Alarcon *et al.*, *Measurement of Quasielastic Spin-Dependent Electron Scattering from a Polarized ^3He Internal Target*, MEA/AmPS proposal 9405, August 1994.
- [48] M. Meyerhoff *et al.*, *Phys. Lett.* **B327** (1994) 201.
- [49] L.J.H.M. Kester, program PLOP, Vrije Universiteit, Amsterdam 1995.
- [50] R.B. Wiringa *et al.*, *Phys. Rev. C* **51** (1995) 38
- [51] H. den Bok, Ph.D. thesis, Universiteit Utrecht, 1995.
- [52] S. Scherer and H.W. Fearing, *Phys. Rev. C* **51** (1995) 359.
- [53] J. Golak, H. Kamada, H. Witała, W. Glöckle and Ishikawa, *Phys. Rev. C* **51** (1995) 1638.

- [54] M.L. Pitt *et al.* TOM: A Target Optical Monitor of polarization and luminosity for polarized internal gas targets. in *Proc. of the Int. Workshop on Polarized Beams and Polarized Gas Targets, Cologne, Germany*, edited by Schieck and Sydow, World Scientific, Singapore 1995.
- [55] H.B. van den Brink, Ph.D. thesis, Vrije Universiteit, Amsterdam 1995.
- [56] E.E.W. Bruins, *Phys. Rev. Lett.* **75** (1995) 21.
- [57] E.E.W. Bruins, Ph.D. thesis, Universiteit Utrecht, 1995.
- [58] S. Kopecky *et al.*, *Phys. Rev. Lett.* **74** (1995) 2427
- [59] R.M. Davidson and G.I. Poulis, *Phys. Rev. D* **54** (1996) 2228.
- [60] E. Passchier, Ph.D. thesis, Universiteit Utrecht, 1996.
- [61] C. Ekström *et al.*, *Nucl. Instr. and Meth.* **A371** (1996) 572.
- [62] M.A. van Uden, Ph.D. thesis, Universiteit Utrecht, 1997.
- [63] M.J.M. van Sambeek, Ph.D. thesis, Vrije Universiteit, Amsterdam 1997.
- [64] Lecture notes for *Nuclear Electrodynamics: Off-Shell Effects and Gauge Invariance*, a workshop at Jefferson Lab (1997).
- [65] M. Bouwhuis, Ph.D. thesis, Universiteit Utrecht, 1998.
- [66] D.J.J. de Lange *et al.*, *Nucl. Instr. and Meth.* **A412** (1998) 254.
- [67] D.W. Higinbotham, *Nucl. Instr. and Meth.* **A 414** (1998) 332.
- [68] I. Passchier *et al.*, *Nucl. Instr. and Meth.* **A 414** (1998) 446.
- [69] C.M. Spaltro *et al.*, *Phys. Rev. Lett.* **81** (1998) 2870.
- [70] D.J.J. de Lange, Ph.D. thesis, Universiteit Utrecht, 1998.
- [71] B. Militsyn, Ph.D. thesis, Technische Universiteit Eindhoven, 1999.
- [72] C. Herberg *et al.*, *Eur. Phys. J.* **A5** (1999) 131.
- [73] J. Becker *et al.*, *Eur. Phys. J.* **A6** (1999) 329.
- [74] D. Rohe, *Phys. Rev. Lett.* **83** (1999) 4257.

- [75] T. Botto, Ph.D. thesis, Vrije Universiteit, Amsterdam 1999.
- [76] I. Passchier *et al.*, *Phys. Rev. Lett.* **82** (1999) 4988.
- [77] M. Ostrick *et al.*, *Phys. Rev. Lett.* **83** (1999) 276.
- [78] M.J.M. van Sambeek *et al.*, *Nucl. Instr. and Meth.* **A 434** (1999) 279.
- [79] H.R. Poolman, Ph.D. thesis, Vrije Universiteit, Amsterdam 1999.
- [80] H.R. Poolman, *Phys. Rev. Lett.* **84** (2000) 3855.
- [81] S. Arzumanov *et al.*, *Nucl. Instr. and Meth.* **A440** (2000) 511
- [82] U.-G. Meissner, *talk at NUCLEON '99*, proceedings in *Nucl. Phys.* **A666&667** (2000) 51c or arXiv:hep-ph/9907323.
- [83] D.L. Groep *et al.*, *Phys. Rev. Lett.* **83** (1999) 5443.
- [84] J.A. Tjon and S. Wallace, *Phys. Rev. C* **62** (2000) 065202.
- [85] E. Six, Ph.D. thesis, Arizona State University, 2000.
- [86] D.W. Higinbotham, Ph.D. thesis, University of Virginia, 2000.
- [87] D.W. Higinbotham, *Nucl. Instr. and Meth.* **A 444** (2000) 557-568.
- [88] I. Passchier, private communication.
- [89] I. Passchier, Ph.D. thesis, Vrije Universiteit 2000.
- [90] Full MC results for ${}^3\text{He}(e, e'n)$ with a grid of Golak's calculations, performed by H.J. Bulten, VU/NIKHEF/SARA, 1997-2001.
- [91] J. Golak, G. Ziemer, H. Kamada, H. Wilała and W. Glöckle, *Phys. Rev. C* **63** (2001) 034006
- [92] C.R. Brome *et al.*, *Phys. Rev. C* **63** (2001) 055502
- [93] D.W. Higinbotham, private communication.
- [94] Xiong *et al.*, JLab ${}^3\text{He}(\vec{e}, e')$.
- [95] J.H. Koch *et al.*: *Hadron structure and the limitations of phenomenological models in electromagnetic reactions*, preprint arXiv:nucl-th/0108044.

- [96] J. Golak, W. Glöckle, H. Kamada, H. Wilała, R. Skibiński, A. Nogga: *Sensitivity Studies for Extraction of G_E^n from Inclusive and Semi-inclusive Electron Scattering on Polarized ^3He* ; preprint arXiv:nucl-th/0110060.
- [97] J. Golak, private communication, 2001
- [98] C.M. Spaltro *et al.*, *The $^3\text{He}(e, e'd)p$ Reaction in (q, ω) -constant Kinematics*, preprint arXiv:nucl-ex/0201011, to be submitted to Nuclear Physics A,B?.
- [99] J.A. Tjon, private communication.
- [100] R. Gilman *et al.*, *A(Q) at low Q in ed elastic scattering*, Jefferson Lab proposal 02-004 (accepted).
- [101] D.W. Higinbotham *et al.*, "Self polarisation in AmPS", to be submitted to *Nucl. Inst. and Meth. in Phys. Res.*.
- [102] H.J. Bulten *et al.*, *Final-state interaction in electron-induced knock-out from polarized ^3He* , to be submitted to *Physical Review Letters*.
- [103] M.F.M. Steenbakkers, Ph.D. thesis, Vrije Universiteit, to be published.

Samenvatting

We hebben voor de reactie ${}^3\text{He}(e, e'n)$ grootheden gemeten die van de polarisatie van het elektron en de ${}^3\text{He}$ -kern afhangen. Daarvoor gebruikten we de MEA/AmPS versnellerfaciliteit van het Nationaal Instituut voor Kernfysica en Hoge-Energiefysica (NIKHEF) in Amsterdam. Een 60% gepolariseerde bundel elektronen met een energie van 720 MeV werd door een intern doelwit geleid waarin zich 50% gepolariseerd ${}^3\text{He}$ gas bevond. De verstrooide elektronen werden gedetecteerd in een magnetische spectrometer met een grote acceptantie, de neutronen in een vluchttijd detector.

We hebben de longitudinale asymmetrie A'_z en de transversale asymmetrie A'_x gemeten in het bereik $0.14 - 0.26 \text{ GeV}^2/c^2$ in Q^2 en $0 - 250 \text{ MeV}/c$ in misende impuls, in twee afzonderlijke metingen met een identieke opstelling. In de meetgegevens voor A'_z bleek dat het resultaat een sterke anomale afhankelijkheid van de bundelstroom heeft. Dit kon voor een deel verklaard worden uit het verlies van polarisatie van de elektronenbundel dat optrad wanneer meer dan (ongeveer) 110 mA in de AmPS ring geïnjecteerd werd. De overblijvende afhankelijkheid is omgezet in een systematische fout, hoewel het ook niet helemaal uitgesloten kan worden dat deze fluctuatie van statistisch oorsprong is.

Monte Carlo (MC) simulaties van het experiment zijn uitgevoerd met twee fundamenteel verschillende berekeningen van de polarisatie-afhankelijke werkzame doorsnede voor de elektrodisintegratie van ${}^3\text{He}$. De berekeningen van Nagorny zijn gebaseerd op een Lorentz-covariante aanpak, met nadruk op ijk-invariantie waarbij op een consistente manier rekening gehouden wordt met de interne structuur van de nucleonen. Herverstrooiing van de nucleonen na absorptie van het virtuele foton (oftewel "eindtoestandswisselwerkingen", FSI) konden tot tweede orde in rekening gebracht worden. De berekeningen van Golak (en de vakgroep theoretische kernfysica in Bochum) zijn gebaseerd

op (niet-relativistische) Faddeevvergelijkingen voor de drie-nucleon continuu-toestanden. In Faddeevvergelijkingen worden eindtoestandswisselwerkingen per definitie tot alle ordes in rekening gebracht.

Alle berekeningen (en simulaties) zijn tweemaal uitgevoerd: een keer onder de aanname dat G_E^n , de elektrische vormfactor van het neutron, gelijk is aan de Galsterparametrisatie (die een waarde geeft in de orde van de beschikbare gegevens van G_E^n , en ongeveer gelijk is aan 0.05 voor $Q^2 = 0.2 \text{ GeV}^2/c^2$), en een keer met de aanname dat $G_E^n = 0$. Voor A_z' leiden deze twee aannames in de MC tot vrijwel identieke uitkomsten, maar voor A_x' zijn er significante verschillen.

De MC uitkomsten voor A_z' komen redelijk overeen met de gemeten data; iets beter met de berekeningen van Nagorny dan met die van Golak.

Voor A_x' daarentegen hebben we negatieve waarden gemeten terwijl de MC simulatie met Nagorny's berekeningen (en ook met een laagste-orde berekening, in de zgn. vlakke-golf-stootbenadering) op positieve waarden uitkomt voor $G_E^n = G_{E, Galster}^n$ en op waarden rond nul voor $G_E^n = 0$. Voor $p_m > 150 \text{ MeV}/c$ wordt het verschil tussen deze berekeningen kleiner. Met de berekeningen van Golak volgen uit de MC simulaties negatieve waarden voor A_x' met $G_E^n = 0$ en waarden dichtbij nul (maar nog steeds negatief) met $G_E^n = G_{E, Galster}^n$.

De uitkomsten van de MC simulatie en de experimentele gegevens kunnen op twee manieren met elkaar vergeleken worden: òfwel we gebruiken de meetgegevens om waarden voor G_E^n te verkrijgen (binnen de context van ieder afzonderlijk model), òfwel we nemen aan dat de elektrische vormfactor van een neutron (gebonden in een ^3He kern) gelijk is aan de Galster waarde en we gebruiken de meetgegevens om te testen of de modellen een adequate beschrijving kunnen geven van de nucleaire dynamica.

In de eerste interpretatie zouden we $G_{E, Golak}^n = 0.031 \pm 0.034(0.023)$ en $G_{E, Nagorny}^n = -0.049 \pm 0.026(0.017)$ vinden, waarbij de getallen tussen haakjes de puur statistische fout aangeven. In principe hebben deze waarden voor G_E^n alleen een welgedefinieerde betekenis binnen de respectieve modellen; een vergelijking met andere G_E^n metingen heeft alleen zin als zeker is dat een model *alle* relevante effecten in rekening kan brengen. We hebben echter ook A_y^0 gemeten (in 1997, met dezelfde meetopstelling) en hoewel Golak's berekeningen van die meetgegevens er dichtbij komen dan die van Nagorny wijken ze er toch significant van af. Een verbetering van de berekeningen zal waarschijnlijk ook de voorspellingen voor A_x' , en dus de G_E^n extractie, significant veranderen.

In de tweede interpretatie zouden we vaststellen dat de Faddeevberekeningen beter overeenkomen met de meetresultaten dan de Lorentz-covariante

berekeningen van Nagorny. Dit moet dan waarschijnlijk toegeschreven worden aan de hogere orde bijdragen van de eindtoestandswisselwerkingen. Deze veroorzaken een negatieve verschuiving in A'_x ten opzichte van een laagste-ordeberekening (PWIA).

Dankwoord

Zeven jaar geleden kreeg ik een e-mailtje van Thomas. Hij had gehoord dat ik op zoek was naar een AIO of OIO plaats. Wel, hij had een vacature voor een OIO, voor een project op het gebied van electron-neutron verstrooiing bij intermediaire energieën. Ik ging bij hem langs, en Thomas vertelde mij over HARP, de High Acceptance Recoil Polarimeter, en over de fysica die hij er mee wilde bedrijven. Dat leek me wel wat. Vooral het meten van G_E^n sprak me aan.

Er rustte geen zegen op het HARP project. Na ruim een jaar hebben we ook maar besloten dat ik de metingen voor mijn proefschrift zou gaan oogsten bij een ander project, in het "9405" experiment in ITH, de Internal Target Hall van de elektronversnellerfaciliteit MEA/AmPS van het NIKHEF. Op die manier zou ik toch G_E^n kunnen gaan meten, hoopte ik. Dat was namelijk het hoofddoel van het "9405" experiment. Alleen de goden waren ertegen. Vlak voor de grote meetperiode, in december 1997, kreeg ik RSI. Bovendien kreeg ik in diezelfde tijd een groot verlies in mijn privéleven te verwerken, waardoor natuurkunde een tijdlang niet de hoogste prioriteit had. Verder bleek tijdens het experiment dat de polarisatie van de elektronbundel zich vreemd gedroeg, en wellicht doordat er veel gepionierd moest worden begingen we allerlei vergissingen en nalatigheden, waardoor de data-analyse nogal lastig werd.

Welnu, de odyssee is volbracht en ik heb veel meegemaakt en geleerd. Ik ben daarvoor een hele boel mensen dank verschuldigd. Laat ik beginnen met mijn promotores. Beste Paul, je raakte, zoals dat heet, in een laat stadium bij dit werk betrokken, en ik dank je voor je bijdragen. Beste Ger, we zijn het over vrij veel dingen oneens geweest en we zijn allebei erg koppig van aard. Maar het is altijd bijzonder leerzaam om standpunten te verdedigen tegenover iemand die een geheel andere mening toegedaan. Bedankt voor alle tijd en energie die je aan mijn promotiewerk gewijd hebt. Beste Thomas, je bent een inspirerende fysicus en ik heb veel van je geleerd. We hebben niet alleen veel over vluchtijddetectoren gepraat, maar ook over alle andere aspecten van het sub-

atomaire onderzoek, over de eigenaardigheden van de Nederlandse cultuur, over muziek, kunst in het algemeen, en zo verder. Bedankt voor alles.

Mijn Utrechtse collega's in de elektronverstrooiing: Henno, Eppo en Andrzej dank ik voor allerlei raad en gezelligheid (Andy: thanks!). Ton, Dick, Kees, Arie, Marc, bedankt voor jullie immer goede humeur en geduld bij het kleine en het grote elektronische en mechanische werk aan de oranje Titanic. Zisis, Eric, Andrew, Eelco, Guillermo, Rob, Karsten and other HARP players, I think we should conclude that it was an big and exciting adventure.

Op het NIKHEF hebben Ronald, Gerco en vooral David G. van het *triple point* me uit allerlei impasses gered tijdens het duel met GLANCE en andere computergerelateerde projecten. Met jullie en met Eddy, Henk, Louk, Marcel v. B., Martijn, Willem K., Willem H. en allerlei buitenlandse medewerkers (telefonerende Italianen) heb ik ook aan allerlei (e, e'p) en (e, e'pp) experimenten in Emin meegedaan en veel geleerd, zoals het draaien van elektronspectrometers en het foutloos overschrijven van scalers.

I had my Internal Target physics adventures together with Blaine, Dirkjan, Dominique, Doug, Ed, Hans Roeland, Hans V., Henk-Jan, Igor, Jo, Laurens, Mark H., Massi, Peter H., Ricardo, Tancredi, Zilou, and others. Mijn bijzondere dank gaat uit naar Jo, voor zijn energieke leiderschap en natuurkundig enthousiasme; naar Igor en Laurens, voor allerlei vrolijke discussies over de data-analyse, polarisatieproblemen, linuxwonderen en wat niet al; nog een keer naar Igor, voor het opvangen van mijn taken in mijn RSI periode; naar Henk-Jan, voor de grote geweldige Monte Carlo berekeningen, een project van ruim vier jaar; en naar de versnellertechnici, voor de vakkundigheid en creativiteit waarmee ze de versneller tot het eind toe draaiende hielden en *tunen*. I would also like to thank Massi, for your inspiring scientific attitude and your style of dealing with problems in physics research.

Sergey, we had many long and interesting discussions about gauge invariance in electron scattering, about the Ukraine and many other subjects, while we worked in the same office. Groetjes aan Mika en Irina. Jacek Golak, thanks for all the work on calculations for our experiment.

Ik wil Justus Koch en John Tjon bedanken voor een aantal zeer leerzame discussies over ijkinvariantie, off-shell vormfactoren en het oplossen van Faddeevvergelijkingen.

Pablo, kamergenoot gedurende het laatste jaar, may the ntuples be with you... en bedankt voor de koffie. De AmPS koffi club werd bevolkt door eerderegenoemde personen en bovendien door Jochen, Jos, Niels, Sander, Hella, Paul v.d. N. en soms ook door Vladas en mensen van de HERMES-groep. Ik was aanvankelijk helemaal niet zo'n trouwe koffiepauzehouder, maar dat werd

steeds beter.

Het fundamenteel onderzoek der materie is ondanks de leuke en soms zeer kleurrijke collega's vaak een nogal eenzame bezigheid. Gelukkig heb ik een sociaal zeer rijke hobby, namelijk kamerkoorzingen, en tijdens het repeteren, cafés bezoeken en concert geven met Het Projectkoor (alias Capella Occento), het Nederlands Studentenkoor, Venus en PA'dam heb ik vaak de kracht en motivatie teruggevonden die nodig waren om dit lange project tot het eind toe vol te houden. Terwijl ik aan niet-fysici probeerde uit te leggen waar mijn onderzoek over ging kwam ik er vaak weer achter waarom ik het ookalweer zo leuk vond. Bovendien hebben niet-fysici veel meer verstand van relativiteit.

Ik wil mijn zusje Sandra en mijn studiegenoten en vrienden Job, Judith, Stan, Wybren en Tanya bedanken voor alle morele steun. Lieve Constance, je zou me waarschijnlijk feestelijk uitlachen voor deze postume dank, ware het niet dat het bestaan van een hiernamaals, met jou daarin, lachend, dit bedankje juist weer bijzonder zinvol zou maken. Lieve Tanya, als er iemand is die me eraan herinnerd heeft dat natuurkunde niet alles is, dat de wereld en het leven vanuit totaal andere perspectieven vaak veel mooier en zinvoller kunnen worden bekeken, dan ben jij het wel.

Lieve ouders, jullie zijn geweldig. Jullie hebben altijd achter mij gestaan, zoals dat heet, en zo moet het ook maar heten, want het is zo.